TECHNISCHE UNIVERSITÄT WIEN

VIENNA UNIVERSITY OF TECHNOLOGY

DIPLOMARBEIT

Space-Filling Polyhedra as Mechanical Models for Solidified Dry Foams

ausgeführt zum Zwecke der Erlangung
des akademischen Grades eines Diplom-Ingenieurs
unter der Leitung von

Univ.Ass. Dipl.-Ing. Dr. Thomas Daxner
ao. Univ.Prof. Dipl.-Ing. Dr. Helmut J. Böhm

Institut für Leichtbau und Struktur-Biomechanik (E317)

eingereicht an der Technischen Universität Wien
Fakultät für Maschinenwesen und Betriebswissenschaften

von

Robert Bitsche
9825484
Myrthengasse 14/9
1070 Wien

Wien, im September 2005

Abstract

The subject of the present thesis is the simulation of the mechanical behavior of idealized, dry foam structures, namely the Kelvin structure and the Weaire-Phelan structure. These structures are models for solidified, dry, closed-cell foams, such as metal foams and polymer foams. The results of such simulations help in gaining insight into the principal deformation mechanisms that govern the mechanical behavior of real solid foams.

The geometry of both the Kelvin and the Weaire-Phelan foams is predicted with the program *Surface Evolver* that can calculate the shape of liquid surfaces which is governed by surface tension. As a result the cell walls are slightly curved, which affects the mechanical behavior of microstructures representing low-density foams. The respective geometries from Surface Evolver are transformed to Finite Element unit cell models for subsequent stress and deformation analyses.

For the determination of the tensors of elasticity, an isotropic linear-elastic bulk material is assumed. The presented results of linear analyses comprise the full tensor of elasticity and its dependence on the relative density. The dependence of the apparent Young's modulus on the loading direction is discussed and correlated with the cubic symmetry of the structures. The slight curvature of the cell walls influences the linear-elastic behavior for relative densities below 4%.

With metal foams in mind, the bulk material behavior for the non-linear simulation is chosen to be elastic-plastic. Therefore, yielding of the bulk material will also affect the effective behavior on the macro-mechanical level, which is demonstrated well by the simulations. Different approaches for the definition of initial yield surfaces are discussed, and such initial yield surfaces are calculated for both foam structures based on a non-linear approach.

One section of the present thesis is also devoted to wet foam structures dominated by *Plateau borders*. A unit cell of a wet Weaire-Phelan foam is predicted with the help of Surface Evolver. This unit cell is a promising candidate for further studies.

Kurzfassung

Das Thema dieser Diplomarbeit ist die Simulation des mechanischen Verhaltens von idealisierten, trockenen Schaumstrukturen: der Kelvin- und der Weaire-Phelan-Struktur. Diese Strukturen sind Modelle für feste, trockene, geschlossenzellige Schäume wie Metall- oder Polymerschäume. Die Ergebnisse solcher Simulationen helfen, die Verformungsmechanismen zu verstehen, die das mechanische Verhalten von realen, festen Schäumen bestimmen.

Die Geometrien der Kelvin- und der Weaire-Phelan-Strukturen werden mit dem Programm *Surface Evolver* berechnet. Surface Evolver ermöglicht die Berechnung der Form von Flüssigkeitsfilmen, die durch das Phänomen der Oberflächenspannung bestimmt wird. Der Umstand, dass die so vorhergesagten Zellwände leicht gekrümmt sind, beeinflusst das mechanische Verhalten der Modelle von Schäumen mit geringer Dichte. Die mit Surface Evolver vorhergesagten Geometrien werden in Finite Elemente Einheitszellenmodelle umgewandelt und so einer Spannungs- und Deformationsanalyse zugänglich gemacht.

Für die Ermittlung des effektiven Elastizitätstensors wurde von einem linear-elastischen Grundmaterial ausgegangen. Die Resultate umfassen den vollständigen Elastizitätstensor und seine Abhängigkeit von der relativen Dichte. Die Abhängigkeit des effektiven E-Moduls von der Belastungsrichtung wird erörtert und mit der kubischen Symmetrie der Strukturen in Beziehung gesetzt. Die leichte Krümmung der Zellwände beeinflusst das linear-elastische Verhalten für relative Dichten unter 4%.

Im Hinblick auf Metallschäume wurde für die nichtlinearen Analysen ein elastoplastisches Materialverhalten des Grundmaterials angenommen. Die Nichtlinearität des effektiven Materialverhaltens wird von der Nichtlinearität des Grundmaterials dominiert. Geometrische Nichtlinearitäten spielen eine untergeordnete Rolle. Verschiedene Ansätze für die Definition von Anfangsfließflächen werden besprochen, und Anfangsfließflächen werden mit Hilfe einer nichtlinearen Methode für beide Schaumstrukturen berechnet.

In einem Abschnitt der vorliegenden Arbeit werden auch nasse Schaumstrukturen behandelt, die von *Plateau Borders* dominiert werden. Mit Surface Evolver wird eine Einheitszelle für einen nassen Weaire-Phelan-Schaum berechnet. Diese Einheitszelle ist ein Erfolg versprechender Kandidat für weiterführende Untersuchungen.

Acknowledgement

First and foremost, my thank goes to my advisor Dr. Thomas Daxner, whose guidance and support taught me a great deal during the preparation of this thesis.

I would also like to thank Prof. Helmut J. Böhm, who impressed me with the thoroughness and quality of his review of this text.

Furthermore, I would like to thank Prof. Kenneth A. Brakke for his assistance with the computer program Surface Evolver.

The greatest thanks I owe to my parents for their great love and support.

Für meinen Großvater

Herrn Paul Bitsche

Contents

1 Introduction

Metal foams are a promising new class of materials, still unfamiliar to most engineers. As metal foams are entering the stage of practical application it is important to close remaining gaps in the knowledge about these materials.

In this introduction we first discuss the production, properties and applications of metal foams. Lastly, we present a short literature overview over existing micromechanical simulation studies.

1.1 Production of Metal Foams

Today most commercially available metal foams are based on aluminum or nickel and their respective alloys. However, it is also possible to produce foams from steel, titanium, magnesium or other metals. Figure 1.1 shows a microscopic cross-section through a closed-cell aluminum foam.

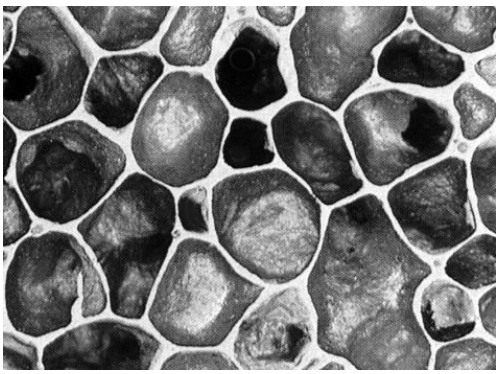

Figure 1.1: Cross-section through a closed-cell aluminum foam. Image courtesy of Neuman Aluminium.

Metal foams are made by several different processing techniques. Many of these techniques are still under rapid development. Three basic concepts are shortly described in the following paragraphs.

Bubbling gas through a liquid metal

A simple way of producing a metal foam is bubbling gas (most commonly air) through a liquid metal (most commonly aluminum). The bubbles float to the

surface and form a foam. At this point of the process drainage of liquid down the walls of the bubbles occurs. For pure metals the rate of drainage is very high and the foam does not remain stable long enough to solidify. Thus, small, insoluble particles are added to the liquid metal. These particles raise the viscosity and slow down drainage. The closed cell foams produced this way have cell diameters between 5 mm and 20 mm. The relative densities lie in the range between 0.03 and 0.1. Figure 1.2 shows a schematic illustration of the process.

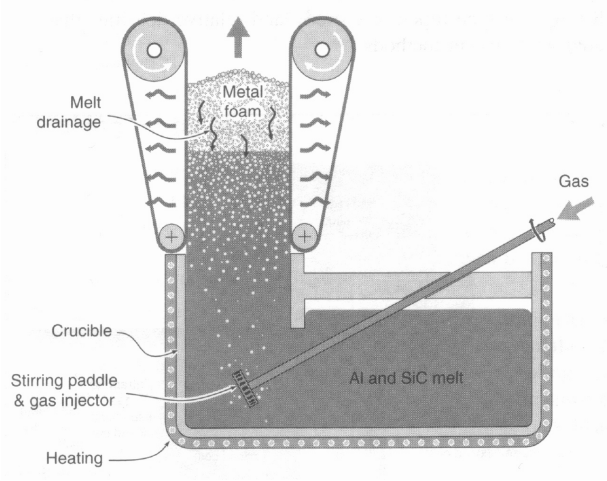

Figure 1.2: Production of aluminum foam by gas-injection.
Picture from [Ashby et al., 2000, p. 8].

Gas-releasing particle decomposition in the melt

Another way of producing a metal foam is based on *foaming agents* such as titanium hydride (TiH_2). If titanium hybride in the form of small particles is added to an aluminum melt, the foaming agent decomposes into Ti and H_2. Thus, large volumes of hydrogen gas are produced and foam forms above the melt. The cell diameters lie between 0.5 mm and 5 mm. The relative densities lie in the range between 0.07 and 0.2.

Gas-releasing particle decomposition in semi-solids

The particles of a foaming agent (TiH_2) are mixed with an aluminum alloy powder. The powder is then consolidated and heated up. As hydrogen gas is produced, voids with a high internal pressure are created. These voids expand and finally form a foam.

Several methods not described here are also used for producing metal foams. A discussion of the different processes can be found in [Ashby et al., 2000].

1.2 Properties of Metal Foams

The mechanical properties of metal foams depend on those of the material from which they are made and on their *relative density* (or apparent density) ρ_{rel}, which is the average density ρ^* of the foam divided by the density ρ_{s} of the solid metal from which it is made.

$$\rho_{\mathrm{rel}} = \frac{\rho^*}{\rho_{\mathrm{s}}} \tag{1.1}$$

Fortunately, the relative density can be measured easily by weighing a sample of known volume.

Moreover, it is important whether the foam has open or closed cells. In this report we will only address closed cell foams.

At first sight one might think that the cell size should also be an important parameter. However, most mechanical properties depend only weakly on cell size.

1.3 Applications for Metal Foams

Lightweight structures

Let us consider a plate with variable thickness loaded in bending. When we require a certain bending stiffness the mass of the plate scales with $\rho/E^{1/3}$:

$$m \sim \frac{\rho}{E^{1/3}} \tag{1.2}$$

When we require bending strength instead of bending stiffness the mass of the plate scales with $\rho/{\sigma_{\mathrm{y}}}^{1/2}$, where σ_{y} is the yield strength of the material:

$$m \sim \frac{\rho}{{\sigma_{\mathrm{y}}}^{1/2}} \tag{1.3}$$

Metal foams have very attractive values of both $\rho/E^{1/3}$ and $\rho/{\sigma_{\mathrm{y}}}^{1/2}$. Therefore, they are very well suited for lightweight structures.

Metal foams are also used as cores for sandwich structures.

Energy absorbers

Metal foams have a long, flat stress-strain curve. When their compressive strength is exceeded the stress stays almost constant (plateau stress) until the densification strain is reached. This feature makes metal foams ideal energy absorbers. The

energy absorbers are designed so that the plateau stress is just below the stress that would cause damage.

Sound absorption and vibration suppression

Metal foams have higher mechanical damping than the solids of which they are made. So by using metal foams it is possible to design parts that are stiff and strong at low weight and have the ability of damping vibrations. This is a very interesting combination for example for the transportation and the machine tool industry.

Other possible applications are heat exchangers, thermal insulation, buoyancy applications, biocompatible inserts, and many others. Moreover, metal foams are recyclable, non-toxic and at least some of them are relatively cheap.

1.4 Simulation of Metal Foams

Numerous micromechanical models have been developed to predict the macroscopic behavior of solid foams. Here we present a short overview over some studies related to the present text.

Grenestedt [Grenestedt, 1999] calculated the effective elastic behavior of various models for solid foams using analytical and numerical techniques. The paper includes an FEM model of the flat-faced Kelvin foam. (As a simplification, the slightly curved faces of the Kelvin foam were regarded as flat.) The effective Young's modulus and shear modulus of Kelvin foams were found to scale almost linearly with the relative density.

Grenestedt [Grenestedt, 1998] also derived upper bounds on the stiffness of closed cell cellular solids with cell walls featuring wavy imperfections. The calculations were based on a square plate with uniform thickness and a sinusoidal imperfection with arbitrary amplitude. The small, wavy imperfections were shown to significantly reduce the stiffness of the models.

Grenestedt and Bassinet [Grenestedt & Bassinet, 2000] used an FEM model of the flat-faced Kelvin foam to study the influence of cell wall thickness variations on the stiffness of closed cell foams. They found that the decrease of foam stiffnesses is minor even for large thickness variations.

Grenestedt and Tanaka [Grenestedt & Tanaka, 1999] modelled the effect of cell shape variations on the stiffness of closed cell cellular solids. They used the Voronoi tessellation of the body-centered cubic lattice (which is exactly the flat-faced Kelvin foam) as a reference model, and then randomly perturbed the "seed-points" of the Voronoi tessellation. The effective elastic moduli were shown not to be sensitive to cell shape variations.

Roberts and Garboczi [Roberts & Garboczi, 2001] studied the effective elastic properties of random closed cell cellular solids. They employed non-periodic, large FEM models (122 cells) based on Voronoi tessellations and Gaussian random fields.

In this report we will use the Finite Element method to study the effective mechanical behavior of two different dry foam structures. The first one is the Kelvin foam, also studied in several papers mentioned above. However, in contrast to these works we do not neglect the slight curvature of the faces of the Kelvin foam dictated by the laws of Plateau [Plateau, 1873].

The second foam structure studied is the *Weaire-Phelan foam* introduced by Denis Weaire and Robert Phelan in 1994 [Weaire & Phelan, 1994]. The Weaire-Phelan foam has lower surface energy than the Kelvin foam, and is thus the new candidate for the optimal monodisperse[1] foam structure. The Weaire-Phelan foam can be considered a more realistic representation of real foams than the Kelvin foam. Like the Kelvin foam, the Weaire-Phelan foam has slightly curved faces.

[1] That is, foam structures built up by cells of equal volume.

2 Introduction to Liquid Foams

2.1 Elements of a Liquid Foam

In this section we will qualitatively describe the elements of a liquid foam structure.

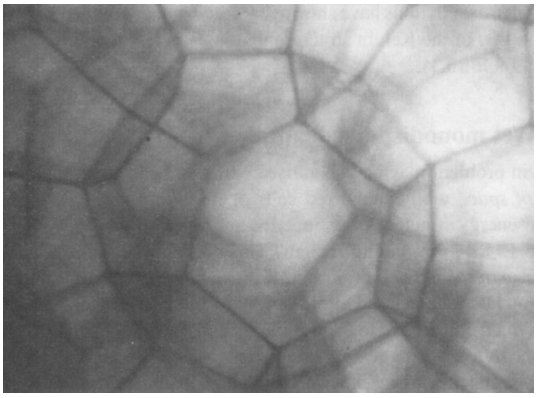

Figure 2.1: Photograph of a dry, liquid foam; Picture from [Weaire & Hutzler, 1999, p. 161].

A liquid foam is a two-phase system in which gas cells are enclosed by a liquid. A foam may contain more or less liquid. If it has little liquid we speak of a dry foam.

A dry foam consists of thin films, which can be idealized as single surfaces. The bubbles are *polyhedral cells* with these surfaces as their faces. (As we will see later, even in a "perfect foam" these faces are not perfectly flat.) The films meet in lines, which are the edges of the polyhedra. The lines meet in vertices. Figure 2.1 is a photograph of a dry, liquid foam structure. In the middle of the picture we can see a polyhedron with five-sided and six-sided faces.

The description presented in the last paragraph is only true for foams containing very little liquid. If the amount of liquid is increased, the edges of the dry foam are replaced by *Plateau borders*. Most of the liquid of the foam is found there. The cross-section of a Plateau border is a concave triangle (Figure 2.2).

As all the edges of the dry foam structure are replaced by Plateau borders, the Plateau borders form a continuous network. Figure 2.3 shows a small section of

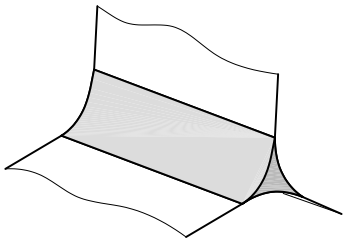

Figure 2.2: Cross-section of a Plateau border with adjacent films.

such a network. For the sake of clarity the faces of the polyhedral cells have been removed from the picture. Figure 2.3 is the result of a computer simulation, based on the polyhedral cell in Figure 2.4 (left) - see Section 4.3.

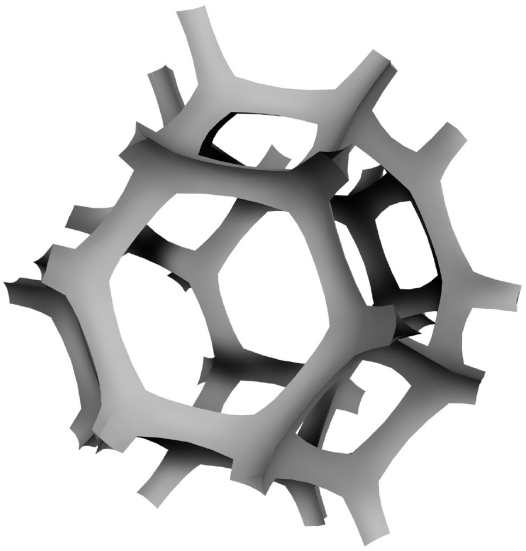

Figure 2.3: Continuous network of Plateau borders; The faces of the polyhedral cells have been removed!

If we look at a single polyhedral cell, we can see that the formation of the Plateau borders rounds off the sharp edges of the cells. Figure 2.4 shows two polyhedral cells. The left one has sharp edges - so this cell is part of a very dry foam. The right one shows the same cell with the amount of liquid having been increased. (The volume liquid fraction is about 2%.) Here the sharp edges are rounded off.

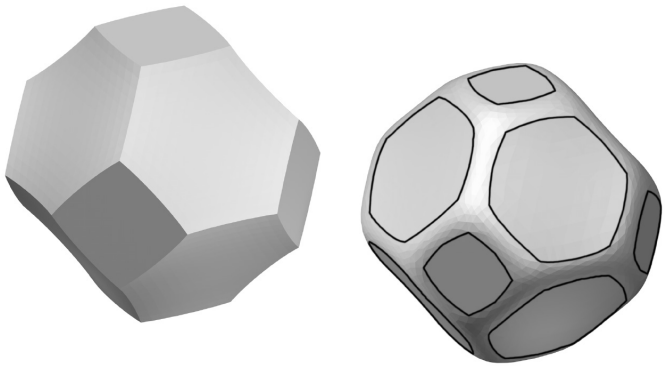

Figure 2.4: With the formation of the Plateau borders the sharp edges of the polyhedral cells are rounded off. The volume liquid fraction is about 2%.

2.2 Elastic Properties of a Liquid Foam

Under low applied stress a liquid foam has some of the properties of a solid material. So it is possible to specify elastic moduli for a liquid foam. The shear modulus of such a foam is mainly a result of the surface tension of the liquid phase. This is why the shear modulus is typically very small. The bulk modulus is mainly a result of the gas pressure in the cells. So the bulk modulus is usually much bigger than the shear modulus. [Weaire & Hutzler, 1999]

It is obvious that these elastic properties of a liquid foam have nothing to do with the elastic properties of a solid metal foam, which will be examined in this report.

2.3 Local Equilibrium Rules

2.3.1 Mean Local Curvature

Let us have a look at the point X on the general surface shown in Figure 2.5. A plane which includes the surface normal at X intersects the surface in a curve. This curve has a local radius of curvature R. It can be shown that it is always possible to specify two directions at right angles to each other, such that the radii R_1 and R_2 take maximal and minimal values. Their inverses $\kappa_1 = \frac{1}{R_1}$ and $\kappa_2 = \frac{1}{R_2}$ are the principal curvatures of the surface at X. The mean of these principal curvatures is called the *mean local curvature* H:

$$H = \frac{1}{2}(\kappa_1 + \kappa_2) = \frac{1}{2}\left(\frac{1}{R_1} + \frac{1}{R_2}\right) \tag{2.1}$$

Remark: The mean curvature is not to be confused with the Gaussian curvature.

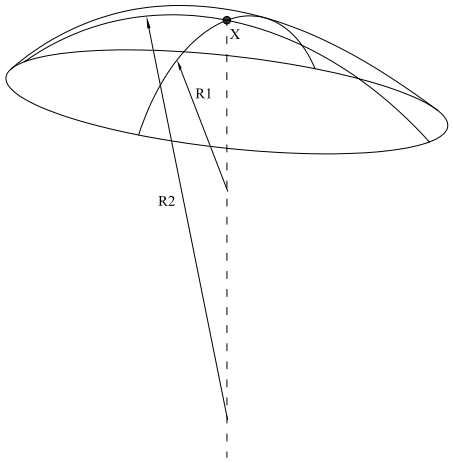

Figure 2.5: Curved surface illustrating principal curvatures.

2.3.2 The Law of Laplace

For a homogeneous liquid the work δU required to create a new surface is proportional to the increase of surface δA:

$$\delta U = \gamma \, \delta A \tag{2.2}$$

The proportionality constant γ is called *surface tension*. It has the dimension force per unit length or, as one can see from Equation (2.2), surface energy per unit area.

At a gas-liquid interface there must be a balance of the pressure difference across the interface (Δp) and the force of surface tension. This is known as the *law of Laplace*:

$$\Delta p = 2\gamma H \quad \text{or} \quad \Delta p = \frac{2\gamma}{r} \quad (r = \frac{1}{H}) \tag{2.3}$$

In (2.3) H is the mean local curvature, and $r = \frac{1}{H}$ is the local radius of curvature of the surface. So the law of Laplace relates the pressure difference to the mean curvature for a liquid surface in equilibrium.

If we insert (2.1) into (2.3) we see that the law of Laplace can also be written as:

$$\Delta p = \gamma \left(\frac{1}{R_1} + \frac{1}{R_2} \right) \tag{2.4}$$

An example: If you dip a metal wire frame into a soap solution, a soap film forms. Obviously here $\Delta p = 0$. Thus, for every point of the surface (2.3) yields:

$$H = \frac{1}{2} \left(\frac{1}{R_1} + \frac{1}{R_2} \right) = 0 \tag{2.5}$$

Such a surface is called *surface of zero mean curvature*. Of course (2.5) is true for a flat surface where $R_1 = \infty$ and $R_2 = \infty$. But it is also true for $R_1 = -R_2$! In Figure 2.6 you can see such a surface. The picture shows a numerically generated image of the surface obtained by dipping a wire frame (thick black line) into a soap solution. The resulting surface has zero mean curvature everywhere.

It can be shown that a surface like the one in Figure 2.6 has minimal surface area for the given boundary (the wire frame). So the mean curvature of a minimal surface is zero everywhere.

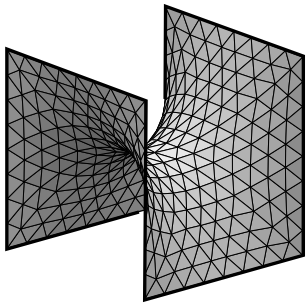

Figure 2.6: Least-area surface spanning a wire frame. The mean curvature of such a minimal surface is zero everywhere.

When dealing with foam structures we will also have surfaces between cells with different pressure ($\Delta p \neq 0$). Then from (2.3) we get:

$$H = \frac{1}{2\gamma}\,\Delta p = \text{const} \quad \text{or} \tag{2.6}$$

$$H = \frac{1}{2}\left(\frac{1}{R_1} + \frac{1}{R_2}\right) = \text{const} \tag{2.7}$$

Such a surface is called *surface of constant mean curvature* or CMC.

2.3.3 The Laws of Plateau

Joseph Plateau (1801 - 1883) added to the law of Laplace some further rules which are necessary for equilibrium. Here, a very condensed version of these rules is presented. For more details see for example [Weaire & Hutzler, 1999].

- *For a dry foam, the films can intersect only three at a time, and must do so at an angle of 120°.*
- *For a dry foam, at the vertices no more than four intersection lines may meet. This tetrahedral vertex is perfectly symmetric, i.e. the angle between two intersection lines is* $\arccos(-1/3) \approx 109.47°$.

- *Where a Plateau border joins an adjacent film, the surface is joined smoothly, that is, the surface normal is the same on both sides of the boundary.*

An intersection of four or more films is not stable. (For example an intersection of four films, immediately splits up to form two intersections of three films.) The angle of 120° is dictated by the equilibrium of the three equal surface tension force vectors. See Figure 2.2 on page 14 for the last rule.

2.4 Voronoi Tessellation

We have seen in Section 2.3.3 that three films intersect in one line in an equilibrium foam structure, and four lines intersect at one vertex. This combinatorics is the same as is observed generically in Voronoi tessellations. Therefore, it is possible to describe foam structures as Voronoi tessellations [Kusner & Sullivan, 1996].

To produce a Voronoi tessellation one starts with a list of points in space called sites. Then the *Voronoi cell* of each site is defined to be the region containing all points closer to that site than to any other. The Voronoi tessellation of a symmetric collection of sites will share its symmetry.

Figure 2.7 shows a two-dimensional example. On the left one can see the Voronoi tessellation of a hexagonal lattice. The Voronoi cells are regular hexagonal honeycombs. On the right one can see what happens when the sites are slightly perturbed.

For an example in three-dimensional space see Figure 3.3 on page 21.

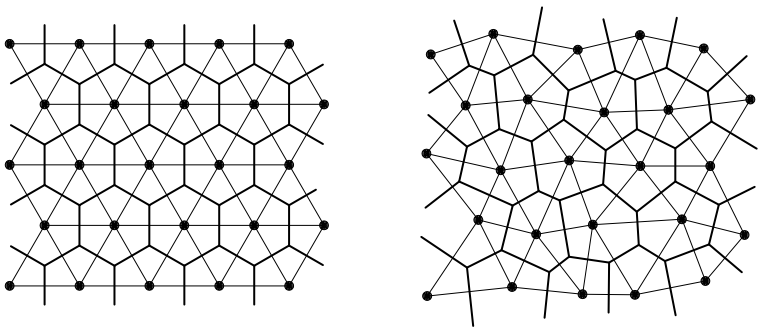

Figure 2.7: Two-dimensional Voronoi tessellations.

3 Ideal Dry Foam Structures

3.1 The Kelvin Problem

Sir William Thomson (later Lord Kelvin) (1824 - 1907) was a British physicist. Kelvin was concerned with a model of the ether[1] and in 1887 asked the following question: *What space-filling arrangement of cells of equal volume has minimal surface area?* This question is today called the Kelvin problem. The problem arises naturally in the theory of dry foams, as a dry foam structure has an energy proportional to the surface area of the films. So trying to minimize the total energy is the same as trying to minimize the total surface area.

The Problem has fascinated mathematicians and physicists since then. The book "The Kelvin Problem" [Weaire, 1996] gives a very good overview on the topic. Many key papers have been reprinted in this book.

The two-dimensional analogon of the Kelvin Problem is: What area-filling arrangement of cells of equal area has minimal line length? The solution is known: it is the regular hexagonal honeycomb. This was proven by Thomas C. Hales in 1999. [Hales, 2001]

In three dimensions the solution for the Kelvin problem is not known. In his paper "On the Division of Space with Minimum Partitional Area" [Lord Kelvin, 1887] Kelvin proposed a solution.

3.2 Kelvin's Solution: The Kelvin Foam

Kelvin considered only those structures in which the cells are identical. (This is not required by the general problem.) Three possibilities are shown in Figure 3.1. The pentagonal dodecahedron (left) looks like a very good choice. However, it simply cannot fill space. The rhombic dodecahedron (middle) can fill space. However, it contradicts Plateau's rules (see Section 2.3.3). So it is not stable. The tetrakaidecahedron (right) was Kelvin's choice. It can fill space (see Figure 3.4) and it approximately obeys Plateau's rules. (The various angles between lines and surfaces do not have exactly the values required.)

[1] The ether was a hypothetical medium the vibrations of which were identified with light waves. This idea is obsolete today.

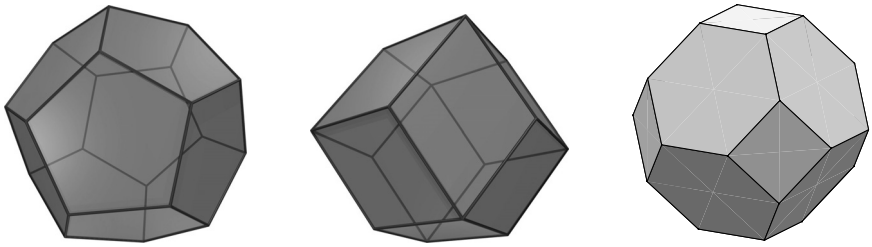

Figure 3.1: Kelvin's candidates: left: Pentagonal dodecahedron; middle: rhombic dodecahedron; right: Tetrakaidecahedron.

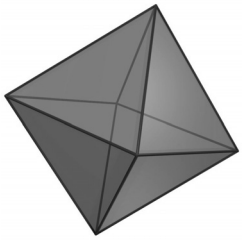

Figure 3.2: Regular octahedron consisting of eight equilateral triangles.

You can look at the tetrakaidecahedron from two different perspectives. One possibility is to start with a regular octahedron consisting of eight equilateral triangles (see Figure 3.2) and truncate the six corners. You do this in such a way that the triangles of the octahedron become equilateral hexagons. The second possibility is to view the tetrakaidecahedron as the Voronoi tessellation (see Section 2.4) for the body-centered cubic (bcc) lattice. Figure 3.3 shows the body-centered cubic lattice (left), and the body-centered cubic lattice with one tetrakaidecahedron sitting in the middle (right).

As already mentioned the tetrakaidecahedron does not exactly obey Plateau's rules. For equilibrium the angles between surfaces should be 120°. The angles between lines meeting at vertices should be $\arccos(-1/3) \approx 109.47°$. Kelvin showed how a slight distortion of the hexagonal faces was sufficient to solve this problem. This distortion reduces the surface area of the cell by about 0.2%! The quadrilateral faces stay flat. We are going to call this distorted tetrakaidecahedron *"The Kelvin Cell"*.

It is not possible to describe the geometry of the Kelvin Cell by an explicit formula. Kelvin used an approximation - a low order harmonic function. However, using the program *Surface Evolver* (see Chapter 4) we can calculate a very good approximation to the Kelvin Cell. We start with the tetrakaidecahedron and let Surface Evolver "relax" the structure. The relaxed structure then fulfills Plateau's

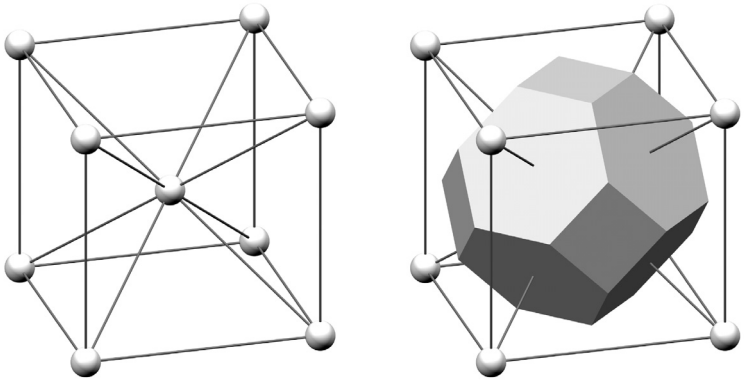

Figure 3.3: Left: body-centered cubic lattice; right: body-centered cubic lattice with one tetrakaidecahedron sitting in the middle.

laws.

Figure 3.4 (left) shows a group of Kelvin cells. Figure 3.4 (right) shows a cubic unit cell. This unit cell fills space, when repeated in a simple cubic lattice. A single Kelvin Cell has to be repeated in a body-centered cubic lattice to fill space.

As mentioned before, in the Kelvin foam all cells are identical. This also means that the pressure in all cells is the same. As we have seen in Section 2.3.2 this means that the surface between two cells must be a surface of zero mean curvature like the one shown in Figure 2.6 on page 17. So $R_1 = -R_2$ everywhere on the surface. But what do these surfaces look like?

To be able to show the distortion of the hexagonal faces we wrote a program that can take the results from Surface Evolver and magnify the distortions of the hexagonal faces. The program uses the plane of the vertices of one of the hexagons as its reference plane and scales the deviations from this plane with a given factor (e.g. 10). This way we obtained the pictures shown in Figures 3.5 and 3.7. Both are scaled with a factor of 10. The maximum deviation from the plane is about 1.3% of the length of a diagonal of a hexagonal face.

When the Kelvin foam relaxes (from the tetrakaidecahedron to the Kelvin Cell) all the symmetries are preserved. These symmetries are the symmetries of the body-centered cubic lattice that can be seen in Figure 3.3. As the quadrilateral faces correspond to mirror planes of the lattice, they stay flat. The hexagonal faces do not correspond to mirror planes, so they do not stay flat. However, the diagonals of the hexagonal faces are two-fold axes of symmetry. Thus, these diagonals stay straight when the foam relaxes. In Figure 3.6 one of these two-fold axes of symmetry, which spans across the hexagons, is shown. In Figure 3.7 one can clearly see that the diagonals of the hexagonal faces stay straight.

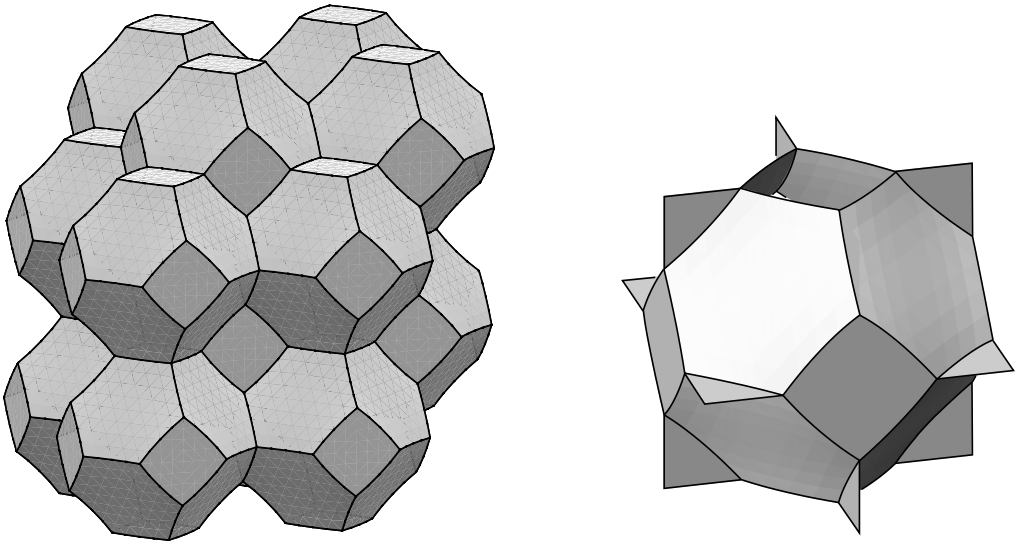

Figure 3.4: Left: 16 Kelvin Cells; right: Cubic unit cell.

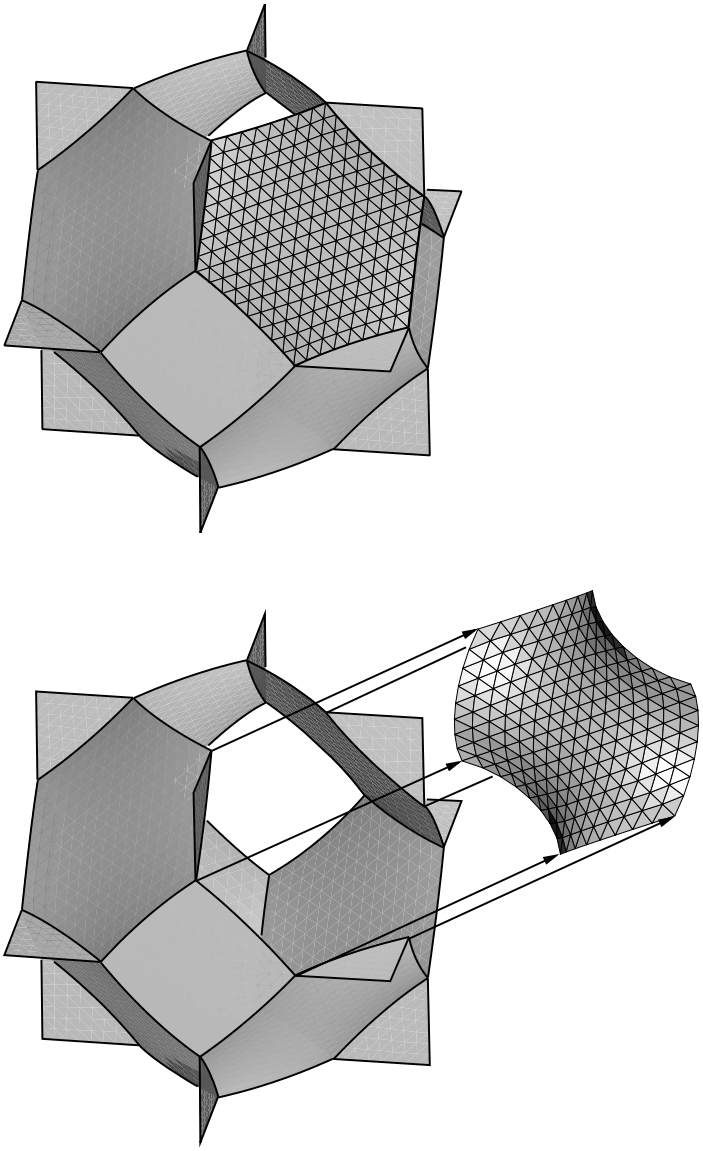

Figure 3.5: Kelvin Cell with the distortion of one hexagonal face being magnified by a factor of 10.

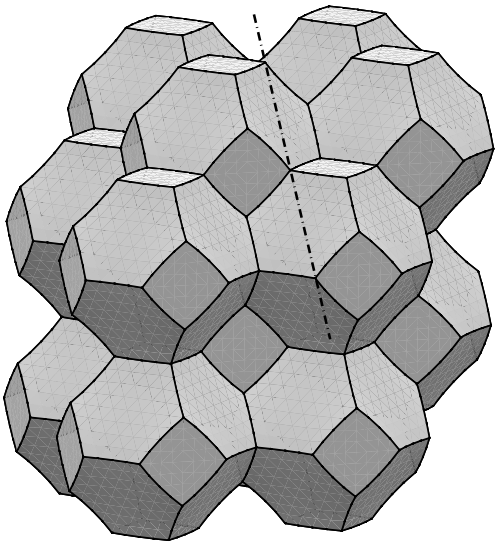

Figure 3.6: Two-fold axis of symmetry.

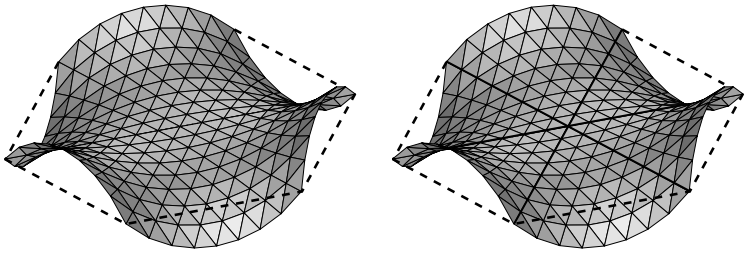

Figure 3.7: Hexagonal face of a Kelvin Cell with the distortions being magnified by a factor of 10. The dotted line represents a flat hexagonal face of the tetrakaidecahedron. Right: The diagonals of the hexagonal face stay straight.

3.3 The Weaire-Phelan Foam

Kelvin never claimed that his cell was the optimal solution. However, for over a century, nobody could improve on Kelvin's partition. But then in 1994, Denis Weaire and Robert Phelan (of Trinity College, Dublin) came up with a partition of space that beats Kelvin's partition by about 0.3% in surface area [Weaire & Phelan, 1994]. 0.3% is a big amount in this context. This structure is called the *Weaire-Phelan foam.*

Figure 3.8: Denis Weaire and Robert Phelan.

As shown in Section 2.3.3 (the laws of Plateau) it would be desirable to find a polyhedral cell with flat faces and symmetrical tetrahedral vertices for solving the Kelvin problem. (Such a cell would definitely be the solution.) However, such a cell does not exist. Nevertheless, it is interesting to calculate the characteristics of this hypothetical cell. It turns out to have 13.397 faces and 5.1043 sides per face [Sullivan, 1999]. In [Weaire & Hutzler, 1999] Weaire explains that "this suggests that a structure should be sought in which the polyhedra have numbers of faces and sides which deviate from these ideal values as little as possible". The Weaire-Phelan foam uses five and six-sided faces exclusively to get as close as possible to this ideal.

Weaire and Phelan started with the Voronoi tessellation of the lattice shown in Figure 3.9. Eight cells form a basic unit that can fill space when replicated in a cubic lattice. The coordinates of the 8 sites (centers) are given in Table 3.1 for a unit cell of dimension 2x2x2.

Then they used Surface Evolver (see Chapter 4) for minimizing the energy (surface area) of the structure. The cells generated by the Voronoi tessellation do not have exactly equal volumes. Fortunately, Surface Evolver can relax the structure (minimize the energy) and equalize the volumes of the cells at the same time. After the relaxation the Weaire-Phelan foam has a surface area which is approximately 0.3% less than that of Kelvin's solution. Kusner and Sullivan outlined a mathematical proof that the Weaire-Phelan partition does in fact beat Kelvin using a weighted Voronoi tessellation [Kusner & Sullivan, 1996].

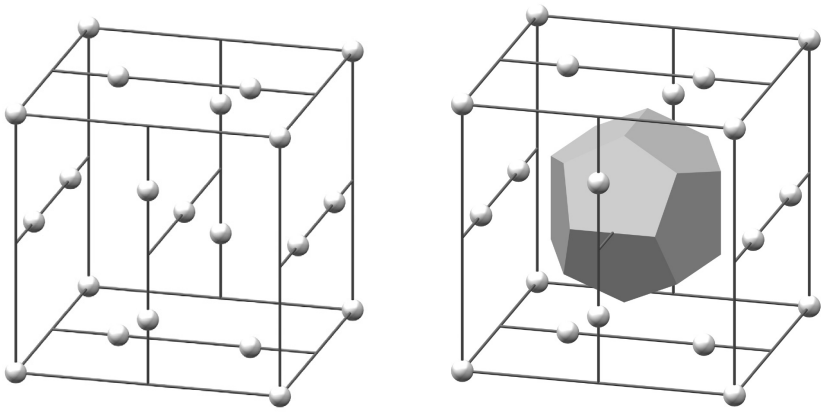

Figure 3.9: Lattice for the voronoi tessellation of the Weaire-Phelan Foam; right: One pentagonal dodecahedron sitting in the middle.

x	y	z	x	y	z
0.0	0.0	0.0	0.0	1.0	0.5
1.0	1.0	1.0	0.0	1.0	1.5
0.5	0.0	1.0	1.0	0.5	0.0
1.5	0.0	1.0	1.0	1.5	0.0

Table 3.1: Sites (cell centers) for the Voronoi tessellation of the Weaire-Phelan Foam in a cubic unit cell of dimension 2x2x2.

Eight cells that form a unit cell for the Weaire-Phelan foam are shown in Figure 3.10. This unit cell fills space when replicated in a cubic lattice. The eight cells are of two types: two (irregular) pentagonal dodecahedra and six 14-hedra. The two types of cells are shown in Figure 3.11 (middle and right).

The pentagonal dodecahedra have 12 pentagonal faces. The 14-hedra have 12 pentagonal and two hexagonal faces. The three different faces of the Weaire-Phelan foam are shown in Figure 3.12. The pentagonal dodecahedra consist of 12 pentagons like the one on the left. The 14-hedra consist of all three types of faces shown in Figure 3.12.

The eight cells shown in Figure 3.10 are a valid unit cell. However, it is often desirable to have a cubic unit cell. So Figure 3.13 shows the cubic unit cell corresponding to the lattice in Figure 3.9. This cubic unit cell, too, can be replicated in a cubic lattice to fill space.

If we compare Figure 3.13 to Figure 3.9 we find that the site in the middle and the eight sites in the corners of Figure 3.9 correspond to a pentagonal dodecahedron.

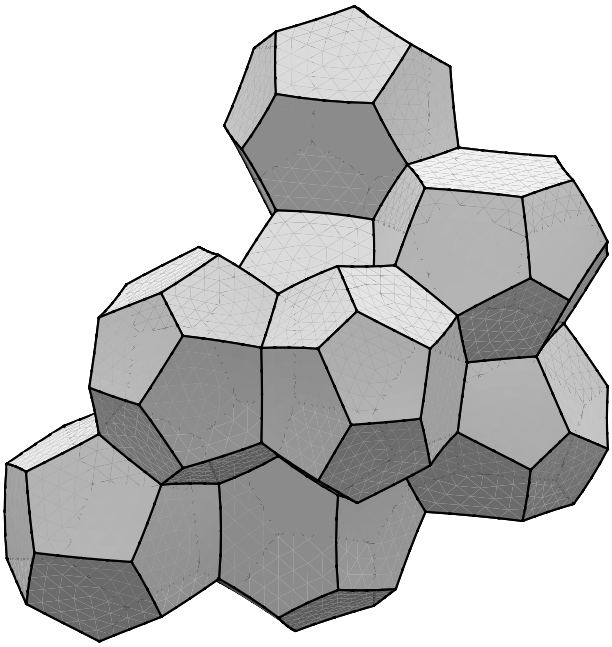

Figure 3.10: The Weaire-Phelan Foam; These eight cells fill space when replicated in a cubic lattice.

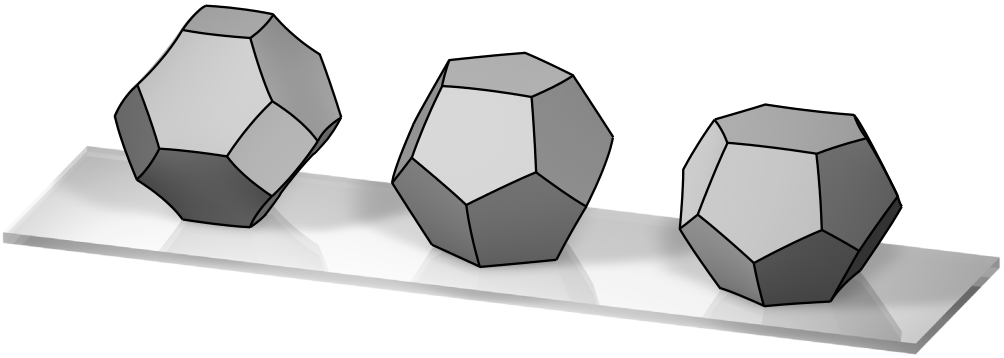

Figure 3.11: Middle: (irregular) pentagonal dodecahedra; right: 14-hedra; Two dodecahedra (middle) plus six 14-hedra (right) form a basic unit for the Weaire-Phelan Foam. The Kelvin Cell on the left is only shown for comparison.

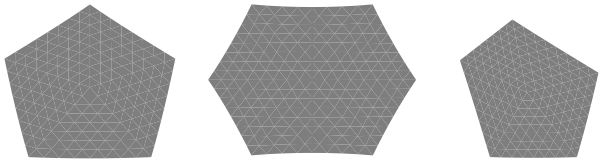

Figure 3.12: The three different faces of the Weaire-Phelan foam.

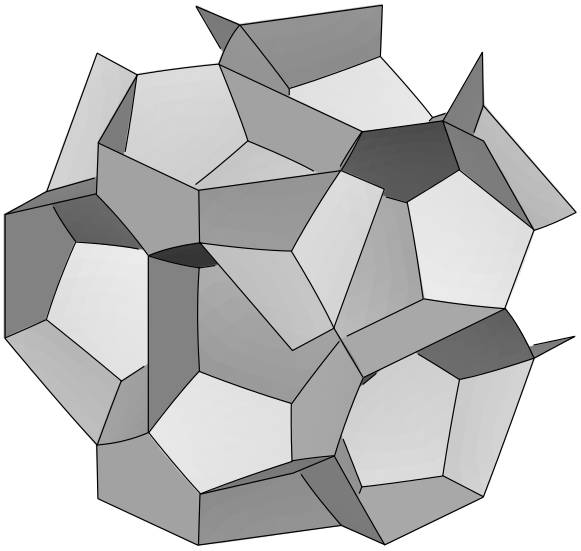

Figure 3.13: Cubic unit cell of the Weaire-Phelan foam corresponding to the lattice in Figure 3.9.

All the other sites in Figure 3.9 correspond to a 14-hedron.

If we look closely at Figure 3.13 we can see that the 14-hedra are arranged as mutually perpendicular, interlocking columns. The pentagonal dodecahedra lie between them on a body-centered cubic lattice. The mutually perpendicular, interlocking columns of the 14-hedra can also be seen in Figure 3.14.

Remark:
The Weaire-Phelan foam belongs to a class of crystal structures known as tetrahedrally close packed (TCP). The TCP structures contain up to four different polyhedra with $f = 12$, 14, 15 or 16 faces (not 13). All these f-hedra have 12 pentagonal faces and $f - 12$ hexagonal faces. Moreover, two hexagons never share an edge [Kraynik et al., 2003].

If you look closely at Figure 3.10 you can see that the vertices of the cells are curved. Certainly some of the faces are non-flat. However, it is again not possible to see the

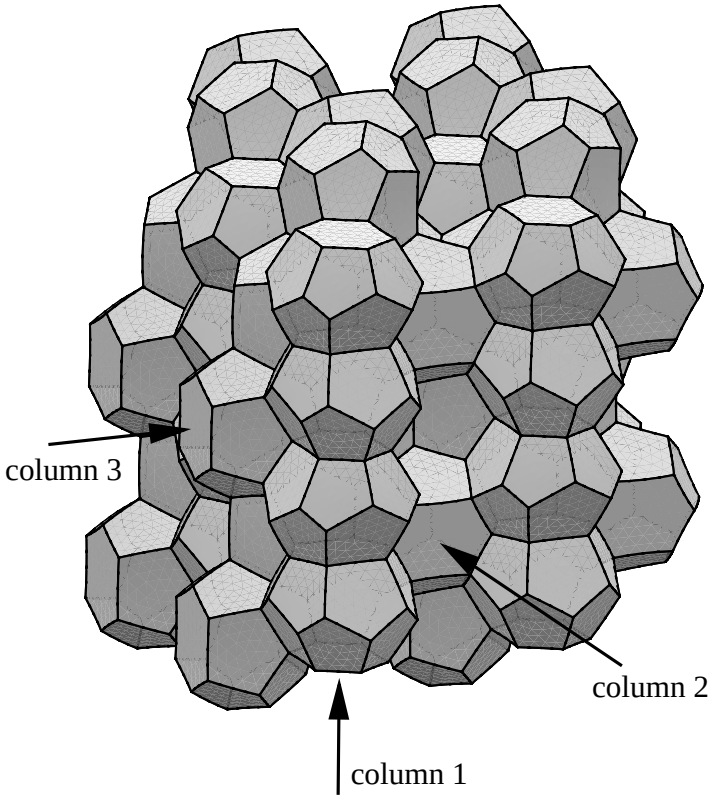

Figure 3.14: The 14-hedra are arranged as mutually perpendicular, interlocking columns.

exact form of the distortions of the faces. So we are going to take a closer look.

When we let the Weaire-Phelan foam relax (from the Voronoi tessellation in Figure 3.9 to the Weaire-Phelan foam) all the symmetries are preserved. These symmetries are the symmetries of the lattice that can be seen in Figure 3.9. All the hexagonal faces of the foam correspond to mirror planes of the lattice. So the hexagonal faces stay flat! All of the other faces do not stay flat.

When we were talking about the Kelvin Cell we argued that as all the cells of the Kelvin foam are identical, the pressure in the cells is also the same. In the Weaire-Phelan foam we have two types of cells (dodecahedra and 14-hedra). The pressure in this two types of cells is not the same. So we have a small pressure difference across faces that are shared by a dodecahedron and a 14-hedron. These are all faces except for the hexagonal faces.

As we have seen in Section 2.3.2 faces between cells with different pressure ($\Delta p \neq 0$) are *surfaces of constant mean curvature*. For this surfaces the law of Laplace yields:

$$H = \frac{1}{2}\left(\frac{1}{R_1} + \frac{1}{R_2}\right) = \frac{1}{2\gamma}\,\Delta p = \text{const} \tag{3.1}$$

What do these surfaces look like? As in Section 3.2 we took the results from Surface Evolver and magnified the distortions of the non-flat faces. The non-flat faces are pentagons of two types (see Figure 3.12 left and right).

The distortions of the pentagons of "Type 1" are shown in Figure 3.15. Here four vertices of the (relaxed) pentagon lie in a plane and are used for defining the reference plane. The distortions of the face have been magnified by a factor of 20. The maximum deviation is about 1.74% of the length of a diagonal of the pentagonal face.

The distortions of the pentagons of "Type 2" are shown in Figure 3.16. Here, three vertices of the (relaxed) pentagon are used for defining the reference plane. The distortions of this face have been magnified by a factor of 15.

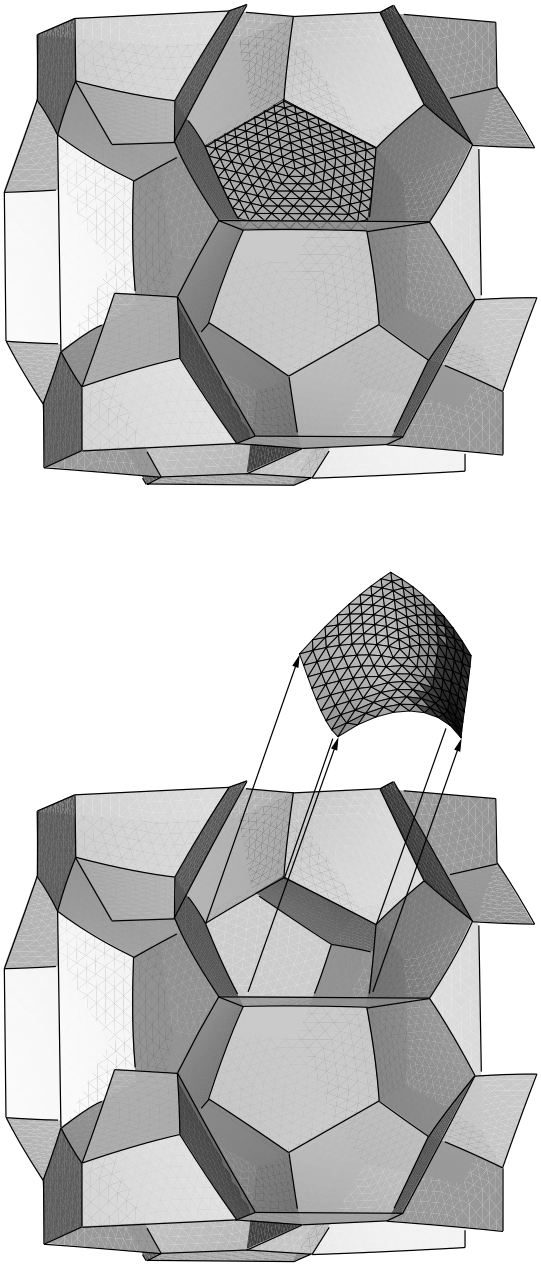

Figure 3.15: Weaire-Phelan unit cell with the distortion of a "Type 1" pentagonal face being magnified by a factor of 20.

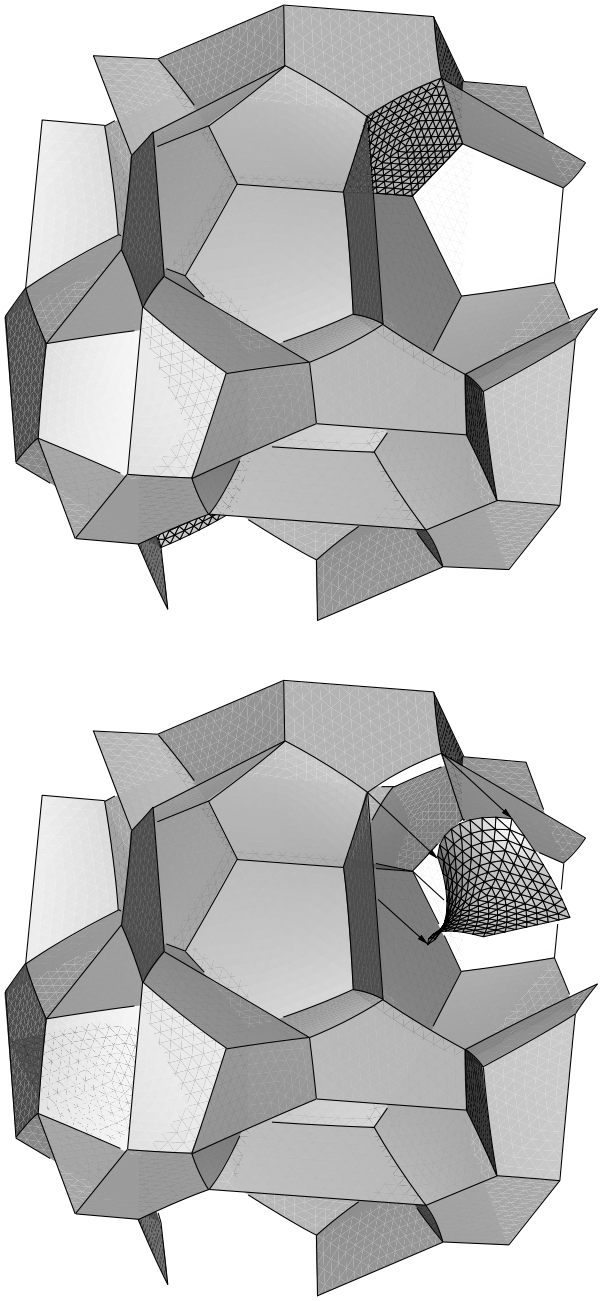

Figure 3.16: Weaire-Phelan unit cell with the distortion of a "Type 2" pentagonal face being magnified by a factor of 15.

3.4 Experimental Observations

Not only physicists and mathematicians but also biologists were fascinated by Kelvin's conjecture and the idea of an "ideal cell". In the 1940s the biologist Edwin Matzke conducted an extremely labor intensive experiment [Matzke, 1946]. He produced soap bubbles of equal size with the help of a syringe and placed them in a glass container one by one. This way Matzke produced about 25000 bubbles and studied each bubble individually.

In the bulk Matzke found an average of $f = 13.7$ faces per bubble. However, the most important result was: not a single Kelvin Cell could be found.

Matzke's experiments are often criticized for various reasons. In [Weaire & Hutzler, 1999] some much more effective methods of experimental foam production are described. However, concerning Kelvin Cells Weaire and Hutzler arrive at the same result: No Kelvin Cells can be found in the bulk.

Fragments of the Weaire-Phelan structure in contrast have been experimentally observed [Weaire & Hutzler, 1999].

4 The Surface Evolver

4.1 Introduction

The *Surface Evolver* is a software package for the modelling of liquid surfaces shaped by surface tension and other energies. The program was developed by Kenneth Brakke in the 1990s and is under continuing development. Surface Evolver is freely available[1] for various systems (Unix/Linux, Windows, Macintosh).

For an introduction to Surface Evolver we refer to [Brakke, 1992]. A comprehensive manual is included in the download.

A surface is described as a union of triangles (called facets) in Surface Evolver. The user defines an initial surface in a datafile. The program then evolves the surface toward minimal energy by a gradient descent method. In our case this energy will simply be surface tension. (The surfaces are assumed to have an energy proportional to their area.) But Evolver can also handle other energies like gravitational energy or user-defined surface integrals.

As an example Figure 4.1 shows how Surface Evolver calculates the surface of zero mean curvature we have already seen on page 17.

In the input datafile we define eight vertices followed by eight edges joining pairs of vertices. Then we define a single face as a loop over all edges. The vertices and edges can be seen in Figure 4.1 (left).

[1] see http://www.susqu.edu/brakke

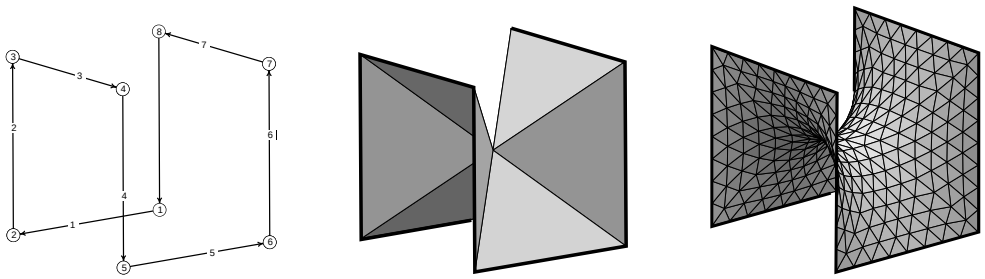

Figure 4.1: Left: definition of the "wire frame"; middle: After automatic triangulation; right: After refinement and energy minimization.

The faces defined in the input file need not be triangles. The face we have defined is not even flat. When Surface Evolver reads the input file it will automatically triangulate the face by putting a vertex at its center and adding edges to each of the original vertices. Figure 4.1 (middle) shows the face after this automatic triangulation.

Now, we can alternately refine the triangulation and do a couple of iteration steps to minimize the energy. After three refinement steps we have the surface shown in Figure 4.1 (right).

Figure 4.2 shows how Surface Evolver refines the triangulation. Each facet (triangle) is replaced by four smaller ones. So with each refinement step the number of facets in the model is quadrupled.

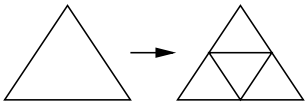

Figure 4.2: Refinement of the triangulation in Surface Evolver.

4.2 Computation of Dry Foam Structures

As already said, Surface Evolver can also calculate approximations to periodic surfaces like the Kelvin foam and the Weaire-Phelan foam. In this section we will explain briefly how this is done.

4.2.1 Computation of the Kelvin and Weaire-Phelan Foams

The input datafiles for the Kelvin and the Weaire-Phelan foams are included in the sample files that come with Surface Evolver. The files are called twointor.fe (Kelvin foam) and phelanc.fe (Weaire-Phelan foam).

Table 4.1 shows the input file for the Kelvin foam. The input file starts with the keyword `TORUS_FILLED`[2]. This indicates that we want to calculate a periodic surface. After the keyword `periods` the basis vectors of the unit cell are defined. The unit cell can be an arbitrary parallelepiped. In our case it is simply a cube of dimension 1x1x1.

Next the `vertices` are defined. The vertices all lie in the unit cell. However, this is not necessary. In Figure 4.3 one of the tetrakaidecahedra we want do define and the cubic unit cell are shown. Moreover, the positions of the 12 vertices defined in

[2]The term *torus* refers to the fact that the topology of the periodic surface can be represented by a flat 3-torus.

```
TORUS_FILLED

periods
1.000000 0.000000 0.000000
0.000000 1.000000 0.000000
0.000000 0.000000 1.000000

vertices
1  0.50 0.00 0.75
2  0.25 0.00 0.50
3  0.00 0.25 0.50
4  0.75 0.00 0.50
5  0.00 0.50 0.75
6  0.50 0.00 0.25
7  0.00 0.75 0.50
8  0.50 0.25 0.00
9  0.25 0.50 0.00
10 0.00 0.50 0.25
11 0.50 0.75 0.00
12 0.75 0.50 0.00

edges  /* with torus wrap symbols */
1     1  2 * * *
2     2  3 * * *
3     1  4 * * *
4     3  5 * * *
5     2  6 * * *
6     2  7 * - *
7     1  8 * * +
8     4  6 * * *
[...]
24    9 10 * * *

faces
1      1   2   4   9  16  -7
2     -2   5  12 -16  24 -10
3     -4  10  18 -21
4      7  15  20  -4  11  -3
5     -1   3   8  -5
6      6  14 -11  -2
[...]
14   -19  22  20  21  14  -3

bodies
1    -1 -2 -3 -4  -5   9   7  11 -9 10  12 5 14  3 volume 0.500
2     2 -6 -7  8 -10 -12 -11 -13  1 13 -14 6  4 -8 volume 0.500
```

Table 4.1: twointor.fe - Surface Evolver input datafile for the Kelvin foam; A few lines have been removed.

the input file are marked with small spheres. At first sight one might think that 12 more vertices are missing in Figure 4.3. However, if we shift the unit cell by one periodicity vector in each direction we can see that no more than these 12 vertices are required.

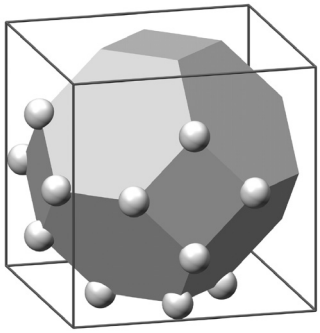

Figure 4.3: Tetrakaidecahedron in the unit cell; The positions of the 12 vertices defined in the input file are marked with small spheres.

Next, 24 `edges` are defined. As we want to define a periodic surface we need a possibility to say how the surface wraps around the unit cell. This is why Surface Evolver uses "torus wrap symbols" to define how edges cross the faces of the unit cell:

- `*` does not cross face of the unit cell,
- `+` crosses in same direction as periodicity vector,
- `-` crosses in opposite direction as periodicity vector.

For example edge number 6 runs from vertex 2 to vertex 7. It does not cross a face in x-direction, it does cross a face in negative y-direction and it does not cross a face in z-direction.

Next 14 `faces` are defined as a loop over the corresponding edges. Finally two `bodies` (two tetrakaidecahedra) are defined by listing the boundary faces.

Why *two* bodies?
It is not sufficient to define one tetrakaidecahedron as one tetrakaidecahedron cannot fill the cubic unit cell. If we look at Figure 4.3 we can see that one tetrakaidecahedron is sitting in the middle, and one eighth of a tetrakaidecahedron is needed for filling up the eight corners of the cubic unit cell.

The lines defining the two bodies in the input file end with `volume 0.500`. This means that the volumes of both bodies are constrained to be 0.5. When Surface Evolver tries to minimize the energy it must keep the volumes at 0.5. (The volume of the cubic unit cell is 1. As two tetrakaidecahedra fill one unit cell, the volume of each tetrakaidecahedron must be 0.5.)

Computation of the Weaire-Phelan foam:
The structure of the input file for the Weaire-Phelan foam (phelanc.fe) is the same as described above. Naturally, it is much longer. 46 vertices, 92 edges, 54 faces and 8 bodies are used. The bodies defined in the input file have been generated by a Voronoi tessellation and do not have exactly equal volumes. However, Surface Evolver will relax the structure and equalize the volumes of the cells at the same time. Various pictures of the resulting Kelvin and Weaire-Phelan foams have been shown in the previous chapter.

4.2.2 Automatic Generation of Surface Evolver Input Files

It is obvious that generating an input file like the one listed in Table 4.1 will be very difficult to do by hand. Therefore, J. M. Sullivan has written a program called vcs which computes three-dimensional Voronoi tessellations and can format the output as a Surface Evolver input file. All that vcs needs for generating the input file for the Weaire-Phelan foam are the coordinates of the eight Voronoi sites (see Table 3.1).

vcs is freely available[3]. However, the program's C code is from 1988. We tried to compile the code, but were not successful. The code would require some updates, so that it can be compiled with a current C compiler.

4.2.3 Reported Areas and the Isoperimetric Quotient

The surface area that Surface Evolver reports after each iteration is the area of the surface within one unit cell. (We will use this number later to calculate the volume of the bulk material by multiplying the surface area within one unit cell with the thickness of the shell elements.) After evolving one of the foams it is a good idea to compare the surface area reported by Surface Evolver with values given in the literature e.g. [Weaire & Phelan, 1994].

In the literature normally no areas are reported, but a figure of merit, the so-called isoperimetric quotient is used. The isoperimetric quotient is defined as:

$$I = 36\pi \frac{V^2}{\bar{A}^3} \tag{4.1}$$

In (4.1) $\bar{A}$ is the *average cell surface area* and V is the cell volume. The isoperimetric quotient is defined in such a way that it is 1 for a sphere. (Naturally, spheres are non-space-filling.) The higher the isoperimetric quotient the lower is the surface area (or energy) of the structure.

[3] http://torus.math.uiuc.edu/jms/software/

Every facet in Surface Evolver is shared by two bodies, but Surface Evolver counts the area of the facet only once. So if we want to calculate *the average cell surface area* we have to multiply the area A_{SE} reported by Surface Evolver by 2 and divide by the number of cells n_{cells} in the unit cell:

$$\bar{A} = \frac{2\,A_{\mathrm{SE}}}{n_{\mathrm{cells}}} \tag{4.2}$$

The cell volume is defined as a volume constraint in the input file, and it is of course the volume of the unit cell divided by the number of cells in the unit cell.

Using the areas reported by Surface Evolver and the formulas above we get:

$$I_{\mathrm{Kelvin}} \approx 0.757 \tag{4.3}$$

$$I_{\mathrm{Weaire\text{-}Phelan}} \approx 0.764 \tag{4.4}$$

These values are also found in the literature e.g. [Weaire & Phelan, 1994].

4.3 Computation of Wet Foam Structures

4.3.1 Modelling Wet Foam Structures in Surface Evolver

Though Surface Evolver was initially developed for studying surfaces, additional features have enabled its application to foams of arbitrary liquid fraction [Phelan et al., 1995; Weaire & Hutzler, 1999].

We already explained that the lines (edges) of a dry foam structure are replaced by Plateau borders if the amount of liquid is increased. The Plateau borders form a continuous network. A small section of such a network can be seen in Figure 2.3 on page 14.

In Surface Evolver a body is defined by giving its bounding faces. Modeling dry foam structures we used one body for each cell of the foam. To model wet foams we will use one body for each cell and one additional body for the entire network of plateau borders. This additional body is exactly what can be seen in Figure 2.3 on page 14.

In our model there are two different kinds of surfaces now. Surfaces between two cells (as we had with dry foams) and surfaces that are shared by a cell and the network of Plateau borders. In Figure 4.4 one can see that where a Plateau border joins an adjacent film two surfaces are attached to one. This is why the surfaces between cells must be given twice the surface tension of the surfaces shared by a cell and the network of Plateau borders.

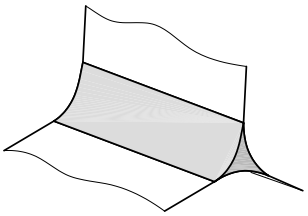

Figure 4.4: Plateau border joins adjacent films.

The pressure in the network of Plateau borders is lower than the pressure in the cells. As we have seen in Section 2.3.2 this means that the surface shared by a cell and the network of Plateau borders is a surface of constant mean curvature.

Of course the input file for such a wet foam structure is even more complicated than the input files for dry foam structures. Fortunately, a program comes with Surface Evolver that can convert an existing input file for a dry foam into an input file for a wet foam. This program is called *wetfoam2.cmd* and is written in the Surface Evolver command language.

The program replaces the edges of the dry foam structure with triangular tubes. These triangular tubes are initial approximations for the Plateau borders. At each vertex of the dry foam structure (where four lines join) an octahedron is used as a junction for the triangular tubes. Figure 4.5 (left) shows such an initial configuration. Moreover, the program adjusts the surface tension of surfaces between cells as explained above.

After refining the triangulation and minimizing the energy with Surface Evolver the Plateau border junction looks like the one shown in Figure 4.5 (right).

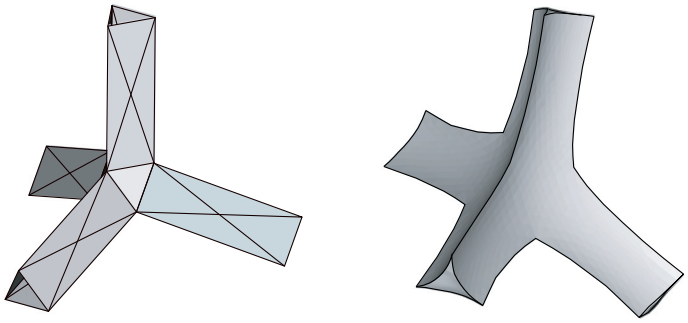

Figure 4.5: Left: initial approximation for a Plateau border junction; right: Plateau border junction after energy minimization.

4.3.2 Computation of a Wet Weaire-Phelan Foam Structure

As Surface Evolver's features for calculating wet foams are not documented at great length we will present an example here. We will model a wet foam based on the input file for the dry Weaire-Phelan foam. The wet foam will have a volume liquid fraction of 10%. The final result of this example can be seen in Figures 4.6 and 4.7.

We start Surface Evolver with the input file for the dry Weaire-Phelan foam:

```
evolver224 phelanc.fe
```

Then we read in the program defined in wetfoam2.cmd:

```
read "wetfoam2.cmd"
```

Next we run the program and redirect the output to a new file:

```
wetfoam >>> "phelanc_wet.fe"
```

Now we have a new input file called phelanc_wet.fe, so we quit Surface Evolver and restart with the new input file. All the edges of the dry foam structure were replaced by triangular tubes as described above.

If we enter "v" Surface Evolver displays the actual volumes and the target volumes for the nine bodies. (Body number nine is the network of Plateau borders.) Surface Evolver has set the target volumes of the nine bodies to agree with the new actual volumes. However, these are not the volumes we want. As we want a volume liquid fraction of 10% the volume of the Plateau borders should be 10% of the volume of the unit cell. The volume of the unit cell is 8.0, so the Plateau borders should have a volume of 0.8. The eight cells are given a volume of 0.9 each so that the volumes sum up to 8.0. The following commands set the body target volume of body number nine to 0.8, and the body target volume of the other bodies to 0.9.

```
set body target 0.8 where id==9
set body target 0.9 where id!=9
```

Before refining the triangulation we do a couple of iterations to adjust the volumes. Now the actual volumes match our desired target volumes and we can refine the triangulation and minimize the energy. The resulting wet foam structure can be seen in Figures 4.6 and 4.7. The structure is approximated by about 16200 triangles. Certainly, further refinement is possible.

Figure 4.6 only shows the individual cells. The network of Plateau borders between them is not shown. Black lines were added to the picture to indicate where Plateau borders join adjacent films.

The eight bubbles in Figure 4.6 fill space when replicated in a cubic lattice. However, it might be easier to again work with a cubic unit cell. So Figure 4.7 shows the

cubic unit cell of the wet Weaire-Phelan structure. As explained above for Surface Evolver the Plateau borders are hollow, but in reality they are filled with liquid. To account for that flat faces corresponding to cross-sections through the plateau borders have been added to the picture.

In the example presented above the triangulation of the surfaces is quite nice. However, in many cases one ends up with a bad triangulation. For example very pointed triangles may appear. Several commands are available that can help to repair such a bad triangulation. Commands that we have found to be very useful are listed in Table 4.2.

K	Skinny triangle long edge divide
l	Subdivide long edges
t	Remove tiny edges
w	Weed out small triangles
u	Equiangulate

Table 4.2: Surface Evolver commands used to repair bad triangulations.

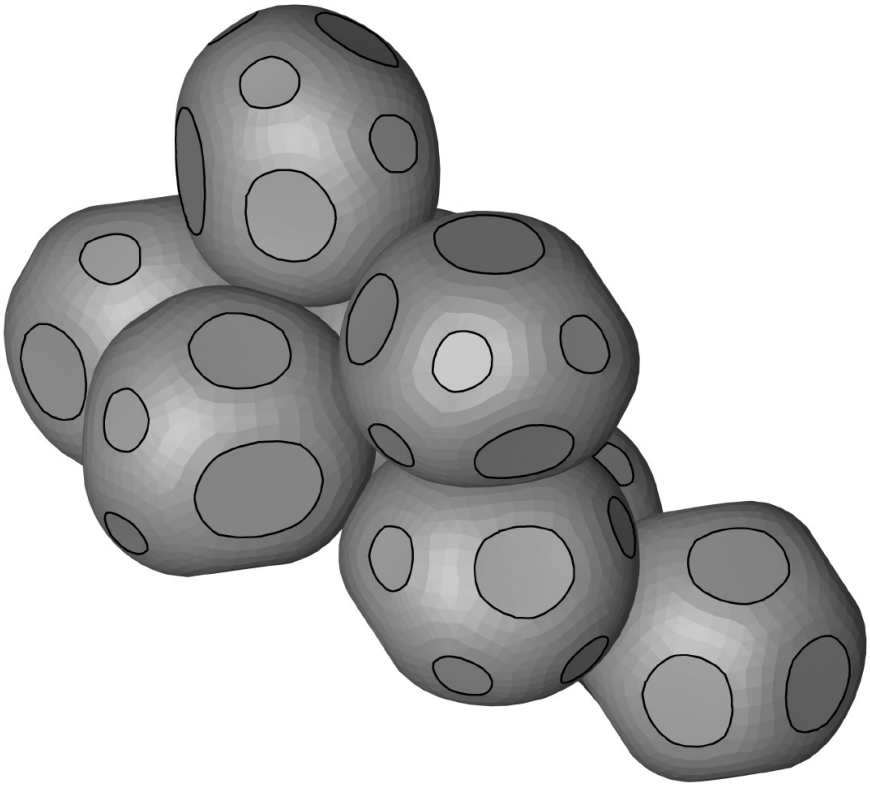

Figure 4.6: Wet Weaire-Phelan foam for a liquid fraction of 10%.

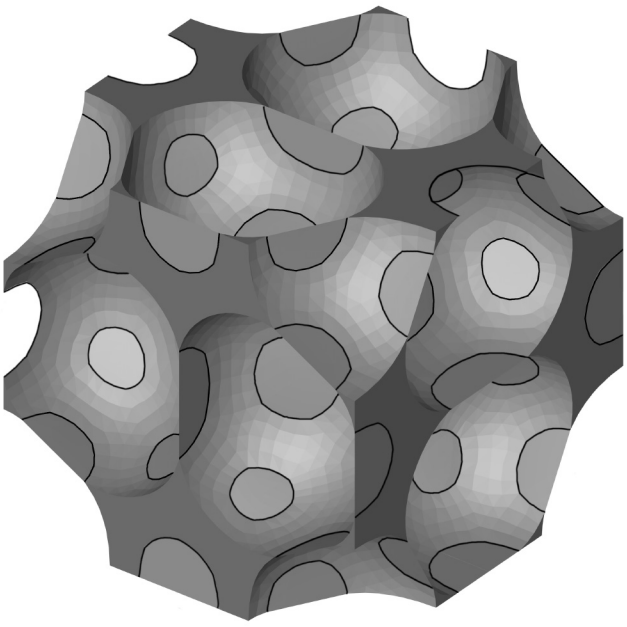

Figure 4.7: Cubic unit cell for the wet Weaire-Phelan foam for a liquid fraction of 10%.

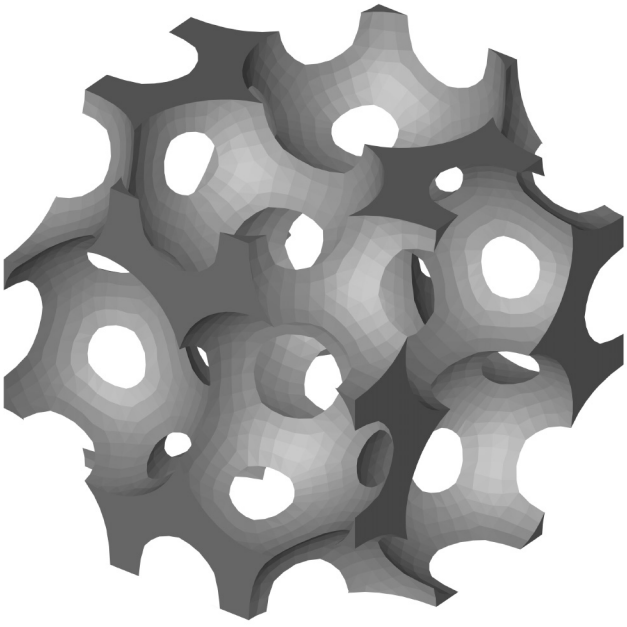

Figure 4.8: Cubic unit cell for the wet Weaire-Phelan foam for a liquid fraction of 10%. The surfaces between cells have been removed so that only the Plateau borders remain.

4.3.3 Stability of Wet Foam Structures

For any given wet foam structure there is a maximum value of the volume liquid fraction φ_{liq} called the *wet foam limit*. If the liquid fraction of the foam is increased beyond this limit, the bubbles become separated. The foam loses its rigidity and is replaced by a *bubbly liquid*. For the Kelvin foam and the Weaire-Phelan foam the critical liquid fractions are 32% and 47% [Phelan et al., 1995].

However, before the bubbles become separated completely, instabilities develop that cause structural change. For the Kelvin foam the first instability occurs at $\varphi_{\text{liq}} \approx 11\%$. At this point the contact areas of what were originally quadrilateral faces are lost. Figure 4.9 shows the Kelvin foam for a liquid fraction of 10%. It can be seen that the contact areas of what were originally quadrilateral faces have become very small. If the liquid fraction is further increased contact will be lost. For the Weaire-Phelan foam the first instability occurs at $\varphi_{\text{liq}} = 15 \pm 2\%$ as reported in [Phelan et al., 1995].

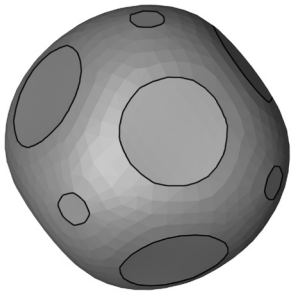

Figure 4.9: Wet Kelvin Cell for a liquid fraction of 10%. If the liquid fraction is increased beyond 11% contact will be lost.

4.3.4 Wet Foam Structures as Mechanical Models for Solid Foams

The initial aim of this thesis was to use dry foam structures generated by Surface Evolver as models for solid foams. Surface Evolver's capabilities to model wet foam structures like the one shown in Figure 4.7 were "discovered" in the course of work. Though this would be very interesting, we will not examine the mechanical properties of such a model. This remains as an interesting challenge for the future.

Creating such a model two problems will have to be addressed. It is quite clear that solid elements must be used for the Plateau borders and shell elements are best used for the surfaces between cells. The surfaces between cells predicted by Surface Evolver have a thickness of zero. However, the shell elements in the finite element model must have a finite thickness. How can this shell thickness be chosen and how does it affect the overall behavior of the structure?

The second problem occurs when we attach the shell elements to the solid elements representing the Plateau borders. As the solid elements don't have rotational degrees of freedom, no bending moments can be transfered to the shell elements. Probably we can argue that the influence of this problem is rather small as long as the shell elements are very thin compared to the thickness of the Plateau borders.

Alternatively the surfaces between cells could be removed completely and the remaining network of Plateau borders could be regarded as a model for an open cell foam.

5 Finite Element Unit Cell Models

5.1 Introduction

To examine the mechanical behavior of the dry foam structures described in the previous chapters we will make use of the *periodic microfield approach* also referred to as the *unit cell method*. A detailed introduction to finite element unit cell methods can be found in [Daxner, 2003].

The basic idea is to study a model material that has periodic microstructure, so that the microstructure can be partitioned into periodically repeating unit cells. The analysis is then limited to one of these unit cells. Special boundary conditions are applied to the unit cell to ensure periodicity of the structure in the deformed state.

The boundary conditions of the unit cell must be specified in such a way that all deformation modes appropriate for the considered load cases can be attained. Three principal types of boundary conditions are possible: periodicity, symmetry and antisymmetry boundary conditions. The most general of these boundary conditions is periodicity. The other two types of boundary conditions allow only for deformation states that do not break the symmetry [Rammerstorfer & Böhm, 2004].

Because of the symmetries of the Kelvin and the Weaire-Phelan foams it would be possible to use symmetry boundary conditions for load cases that do not break those symmetries. This would reduce the size of the unit cells and thus the computational resources needed. Figures 5.1 and 5.2 show the cubic unit cell for the Kelvin and the Weaire-Phelan foam together with the corresponding unit cells that make use of mirror symmetries. Because we wanted to be able to handle shear-deformations that break the mirror symmetry of the unit cells we used periodicity boundary conditions exclusively.

Figure 5.3 shows the application of periodicity boundary conditions to a 2D unit cell. The unit cell has four edges N (north), E (east), S (south), W (west) and four corners NE, SE, SW, NW. The displacements of the corners SW and SE are constrained to restrict rigid body movement.

To ensure periodicity of the unit cell in the deformed state the following coupling equations are used:

$$\mathbf{u}_{\mathrm{E}}(y) = \mathbf{u}_{\mathrm{W}}(y) + \mathbf{u}_{\mathrm{SE}} \tag{5.1}$$

$$\mathbf{u}_{\mathrm{N}}(x) = \mathbf{u}_{\mathrm{S}}(x) + \mathbf{u}_{\mathrm{NW}} \tag{5.2}$$

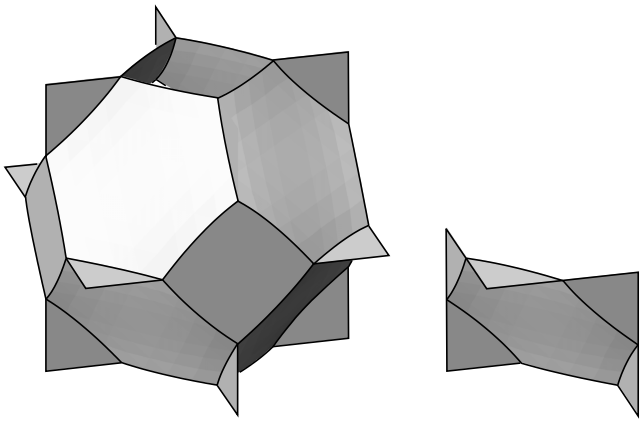

Figure 5.1: Left: Cubic unit cell of the Kelvin foam; right: Smaller unit cell making use of mirror symmetries.

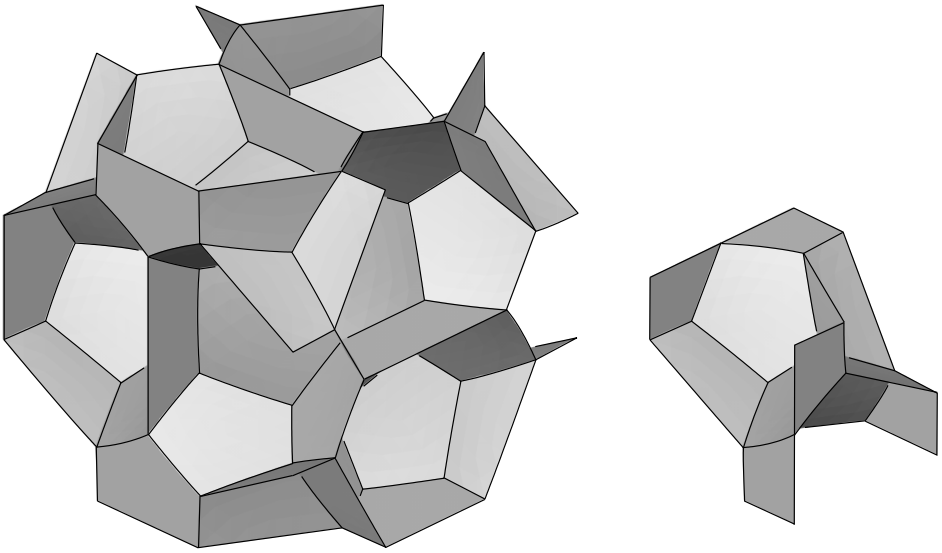

Figure 5.2: Left: Cubic unit cell of the Weaire-Phelan foam; right: Smaller unit cell making use of mirror symmetries.

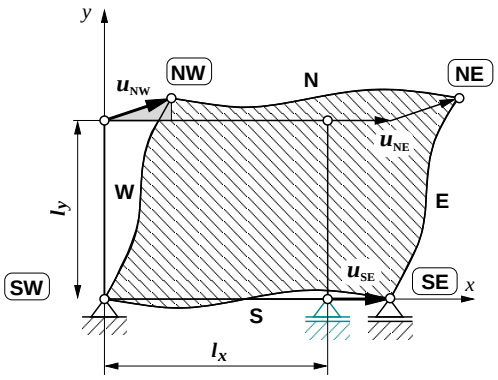

Figure 5.3: 2D unit cell in the undeformed and the deformed configurations. From [Daxner, 2003, p. 13].

As one can see the displacements of points on the edge E (the slave) are constrained to be identical to those on the edge W (the master) except for a constant additional offset vector $\mathbf{u}_{\mathrm{SE}}$. In analogy, the degrees of freedom of points on the edge N (the slave) are constrained to be identical to those on the edge S (the master) except for a constant additional offset vector $\mathbf{u}_{\mathrm{NW}}$. The displacements $\mathbf{u}_{\mathrm{SE}}$ and $\mathbf{u}_{\mathrm{NW}}$ are related to the global deformation modes of the unit cell. Therefore, the nodes SE and NW are called *master nodes*.

For small strains and displacements the components of the vectors $\mathbf{u}_{\mathrm{NW}} = \{u_{\mathrm{NW}}, v_{\mathrm{NW}}\}$ and $\mathbf{u}_{\mathrm{SE}} = \{u_{\mathrm{SE}}, 0\}$ are related to the macroscopic strain state of the unit cell by:

$$\varepsilon_{xx} = \frac{u_{\mathrm{SE}}}{l_{\mathrm{x}}}\,, \qquad \varepsilon_{yy} = \frac{v_{\mathrm{NW}}}{l_{\mathrm{y}}}\,, \qquad \gamma_{xy} = \frac{u_{\mathrm{NW}}}{l_{\mathrm{y}}}\,. \tag{5.3}$$

The master nodes SE and NW are also used as points for load application. *It can be shown that unit cell models react to concentrated loads on master nodes like the infinite periodic structure would react to homogenized applied stresses* [Smit et al., 1998; Daxner, 2003]. With H and V as horizontal and vertical forces, resprectively, we get for the engineering stresses:

$$\sigma_{xx} = \frac{H_{\mathrm{SE}}}{l_{\mathrm{y}}}\,, \qquad \sigma_{yy} = \frac{V_{\mathrm{NW}}}{l_{\mathrm{x}}}\,, \qquad \sigma_{xy} = \frac{H_{\mathrm{NW}}}{l_{\mathrm{x}}}\,. \tag{5.4}$$

The same framework can be used for defining a three-dimensional unit cell. Figure 5.4 shows a three-dimensional unit cell in a general deformation state. For the sake of clarity the local deformation field is not shown. The three master nodes are SEB (South-East-Bottom), NWB (North-West-Bottom) and SWT (South-West-Top). Together these three master nodes have six unconstrained degrees of freedom corresponding to the six global deformation modes (three normal strain modes and three shear strain modes).

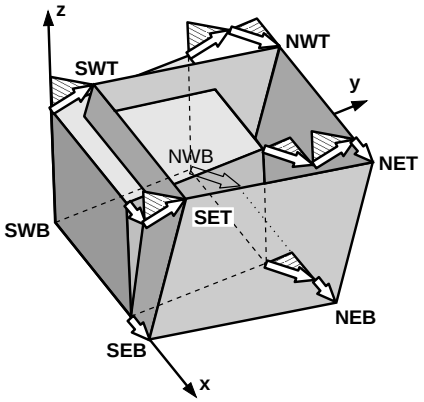

Figure 5.4: 3D unit cell in a general deformation state; From [Daxner, 2003, p. 16].

5.2 Building Unit Cell Models for the Kelvin and Weaire-Phelan Foams

5.2.1 Converting Results from Surface Evolver to Finite Element Models

In this section we will describe a method for converting the results from Surface Evolver to a finite element model that can be used in ABAQUS. We will also address some unexpected problems that occurred in this process.

Surface Evolver uses triangular facets to represent a surface. It is convenient to translate these triangular facets to triangular shell elements. There are several triangular shell elements available in ABAQUS. However, only element type S3 is suitable for large-strain analysis. So this element type was chosen. The S3 Element has three nodes, uses linear interpolation and has one integration point. Thus, a fine mesh is generally required. For calculations including nonlinear material behavior 11 integration points were used through the shell section.

In Surface Evolver the command "`d`" dumps the current data to a file in the same format as the initial data file. (See Table 4.1 on page 36.) It is certainly possible to build a finite element model for a cubic unit cell based on this data. However, the wrapping of the edges around the unit cell would have to be accounted for, and additional vertices would have to be created where the structure crosses a clipping plane of the cubic unit cell.

Fortunately, there is a way around this. One can first display a cubic unit cell in Surface Evolver (command `s`) and then write the data to a file in OFF-format[1]

[1]The OFF-format is 3D graphics format for the interactive viewing program Geomview. Geomview is freely available: http://www.geomview.org

(command `P`). Now Surface Evolver does the wrapping and the creation of additional vertices for us. The OFF file contains a list of vertices followed by a list of triangles. As this is almost identical to the way a mesh is defined in ABAQUS, it was simple to write a program that converts the OFF file to an ABAQUS mesh definition file. However, problems occurred in conjunction with the conversion that will be addressed in the following paragraphs.

The first problem has to do with surfaces that lie exactly in a clipping plane. Sometimes one part of such a surfaces is positioned on one side of the unit cell while the other part is positioned on the other side. Though such a unit cell is valid it is certainly undesirable. This problem could be solved using the script `rewrap.cmd` that comes with Surface Evolver. Simply enter `read "rewrap.cmd"` and then `rewrap`.

The second problem was that the OFF file contained some degenerate triangles where two or three vertices of the triangle were identical. I reported this problem to Prof. Brakke who maintains Surface Evolver. Prof. Brakke solved the problem and provided a revised version of the program (2.24b) within short time.

The third problem occurs because the vertices defined in the file phelanc.fe (the input file for the Weaire-Phelan foam) are not exactly where one would expect. As explained in Section 3.3 the Weaire-Phelan foam starts as the Voronoi tessellation of a certain lattice. The sites are given in Table 3.1 on page 26. According to this the first vertex in phelanc.fe should exactly have the coordinates `1.375, 0.0, 0.3125`. However, the first vertex in phelanc.fe reads `1.374833, 0.000542, 0.313036`. Obviously there is a small offset. Prof. Brakke advised me that the coordinates in phelanc.fe are inherited from what Weaire and Phelan originally sent him. I assume that Weaire and Phelan used the program vcs (see Section 4.2.2) to produce the file phelanc.fe, and that the algorithm vcs uses to compute the Voronoi tessellation causes the offset.

As the Weaire-Phelan structure converges toward an equilibrium the small initial offsets are not a problem. However, when Surface Evolver clips the structure to produce a cubic unit cell vertices lying very close to (but not on) a clipping plane lead to the formation of very pointed triangles. In the example above the y-coordinate of the vertex should be 0.0. So the vertex should be exactly on the clipping plane of the cubic cell. But as there is a small offset a very pointed triangle will be produced. Figure 5.5 schematically shows this. For numerical reasons these pointed triangles are not acceptable in a finite element model. Two possible solutions have been found to overcome this problem.

Prof. Brakke proposed a quick solution making use of the Surface Evolver command language. After evolving the Weaire-Phelan structure the following commands put the vertices that are very close to the clipping planes on the clipping planes:

```
set vertex x 0 where abs(x) < 0.001
set vertex y 0 where abs(y) < 0.001
```

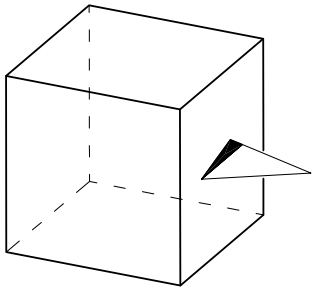

Figure 5.5: When Surface Evolver clips the structure vertices lying very close to a clipping plane lead to the formation of very pointed triangles.

```
set vertex z 0 where abs(z) < 0.001
set vertex x 2 where abs(x-2) < 0.001
set vertex y 2 where abs(y-2) < 0.001
set vertex z 2 where abs(z-2) < 0.001
```

As this means altering the geometry of the structure after evolution we decided for another approach.

The problem can also be solved by modifying the input file. At a closer glance we find that only 17 different coordinate values are admissible in the cubic unit cell for the Weaire-Phelan foam. These values are the same in all three directions. We constructed the Voronoi Tessellation shown in Figure 3.9 on page 26 with a 3D CAD-Software and obtained the true coordinate values. The values are listed in Table 5.1. Finally we wrote a script that runs through the file phelanc.fe and replaces each coordinate value by the value from Table 5.1 it is closest to. The vertices that are now exactly on the clipping planes in the input file remain there throughout the evolution and no pointed triangles are produced anymore.

0.00000	0.50000	1.00000	1.50000	2.00000
0.31250	$0.58333\dot{3}$	1.31250	$1.58333\dot{3}$	
0.37500	0.62500	1.37500	1.62500	
$0.41666\dot{6}$	0.68750	$1.41666\dot{6}$	1.68750	

Table 5.1: True coordinate values for the vertices in phelanc.fe.

As already explained Surface Evolver refines its triangulation by replacing each triangle by four smaller ones (see Figure 4.2 on page 35). For both the Kelvin and the Weaire-Phelan structure the first five refinements were converted to finite element models. “Refinement 1” is Surface Evolver’s automatic triangulation. Figures 5.6 to 5.9 show the different meshes.

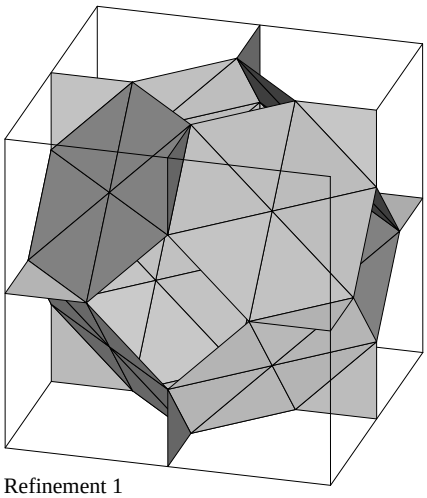

Refinement 1
Nodes: 47
Elements: 72

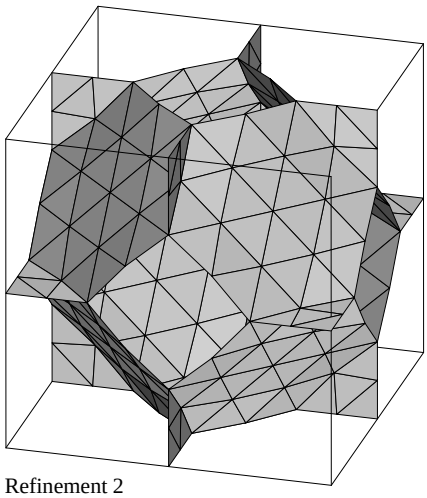

Refinement 2
Nodes: 167
Elements: 288

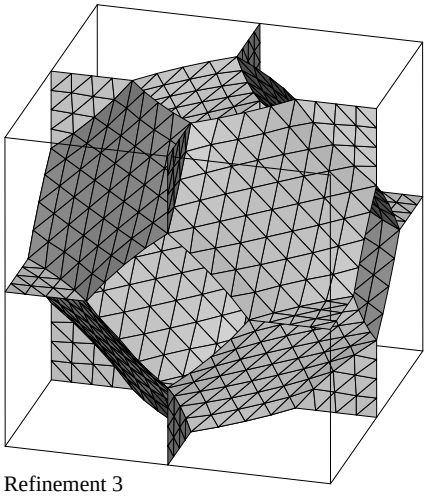

Refinement 3
Nodes: 623
Elements: 1152

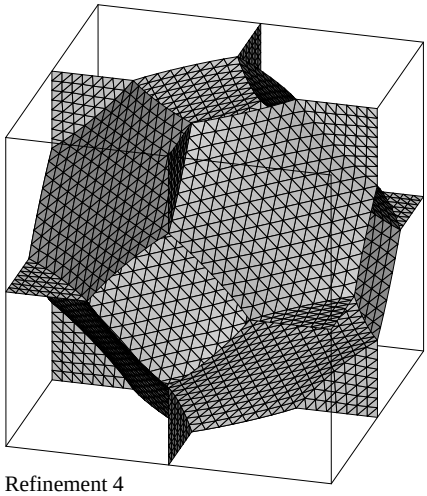

Refinement 4
Nodes: 2399
Elements: 4608

Figure 5.6: Kelvin unit cell: refinements 1 to 4.

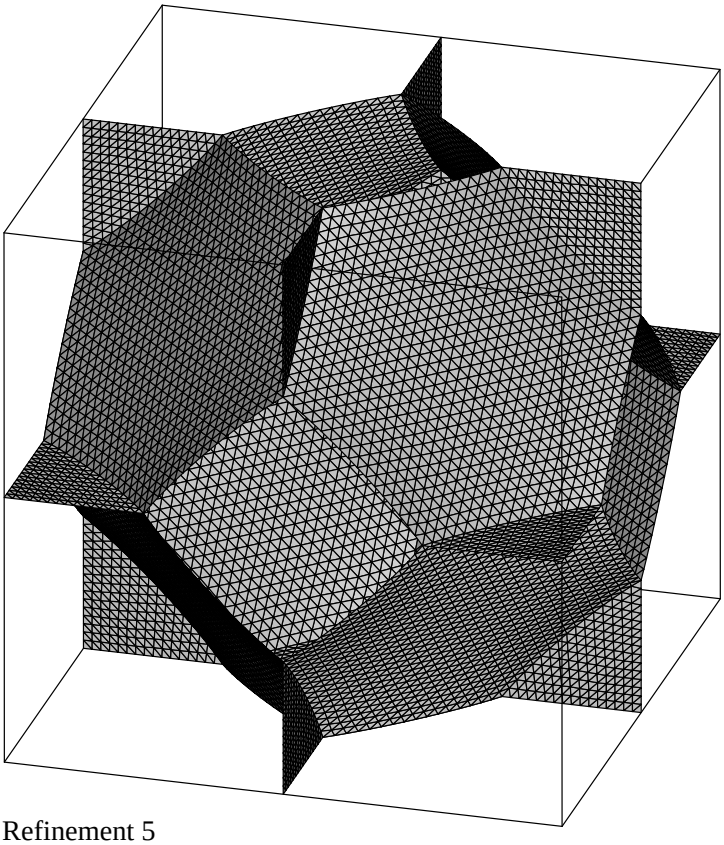

Refinement 5
Nodes: 9407
Elements: 18432

Figure 5.7: Kelvin unit cell: refinement 5.

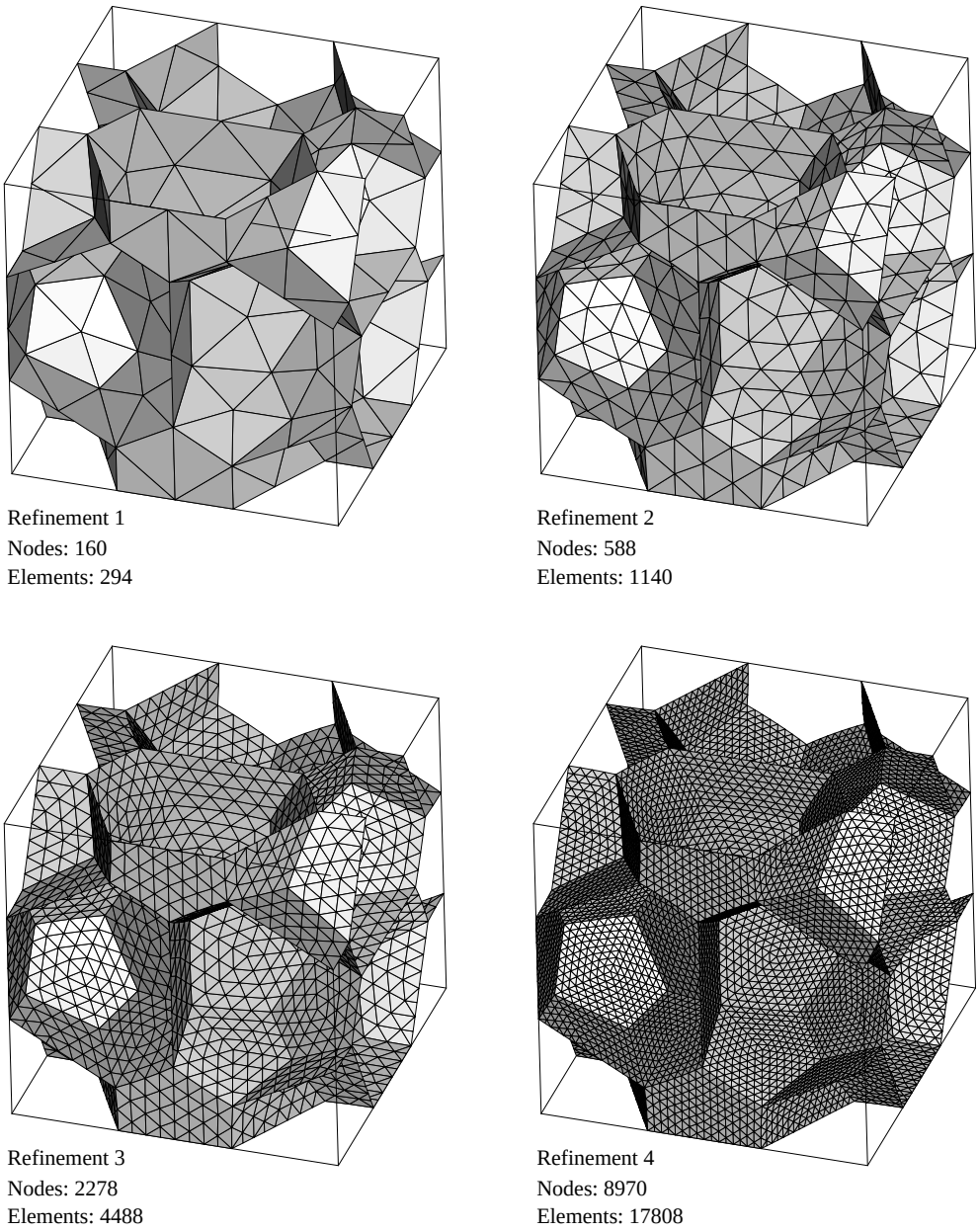

Figure 5.8: Weaire-Phelan unit cell: refinements 1 to 4.

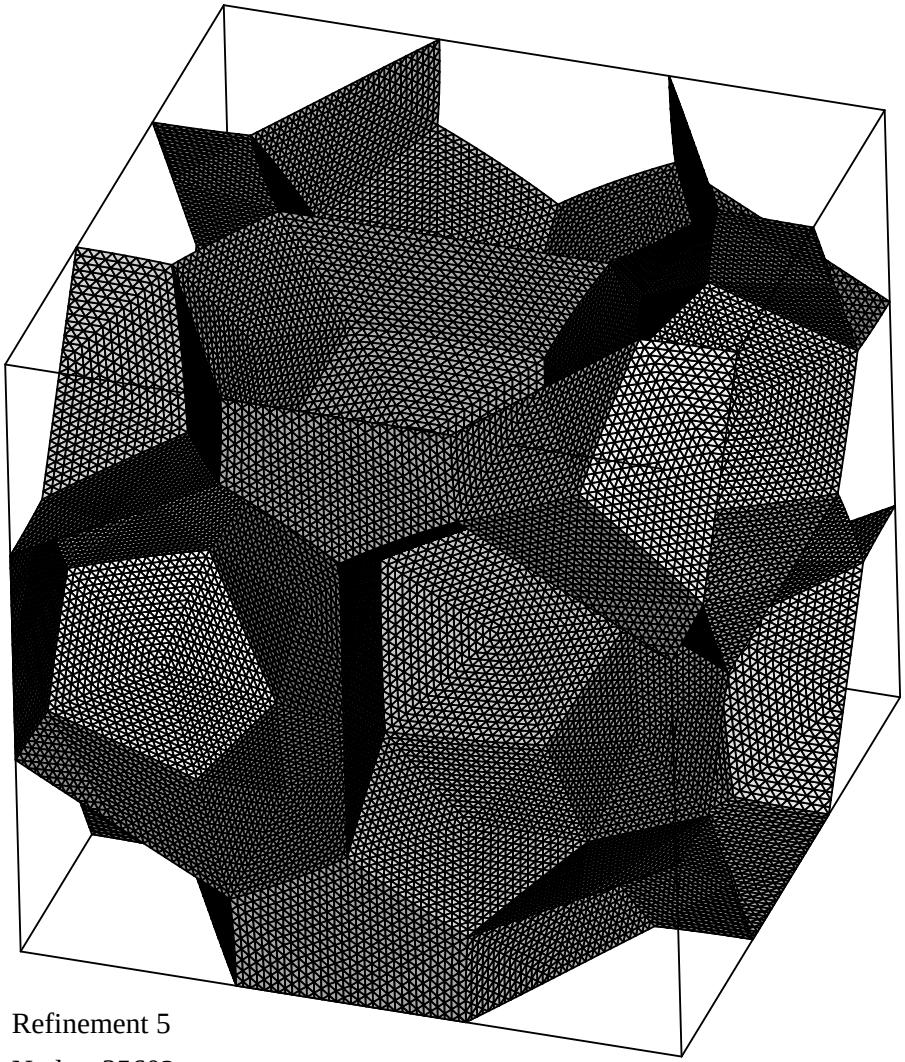

Refinement 5
Nodes: 35602
Elements: 70944

Figure 5.9: Weaire-Phelan unit cell: refinement 5.

5.2.2 "Flat" Kelvin and Weaire-Phelan Models

It is interesting to compare the results obtained from the meshes described above to results obtained from "flat" Kelvin and Weaire-Phelan unit cells. The corresponding meshes were obtained by successively refining the initial triangulation in Surface Evolver without doing any energy minimization. Without energy minimization the faces stay flat. So these models correspond to the initial Voronoi tessellation of the structures described in Chapter 3.

5.2.3 Generation of Periodicity Boundary Conditions

Now that we have the meshes we need to specify the periodicity boundary conditions which are the three-dimensional analogon of Equations 5.1 and 5.2.

To achieve this in ABAQUS the displacements of corresponding finite element nodes are coupled using linear constraint equations. It would be cumbersome to define these equations by hand. Fortunately, a preprocessing tool was developed at the ILSB which can generate the constraint equations automatically.

5.2.4 Choosing the Shell Thickness

To complete our model we have to choose an appropriate shell thickness. As already mentioned the relative density of a foam is defined as:

$$\rho_{\mathrm{rel}} = \frac{\rho^*}{\rho_{\mathrm{s}}}\,, \tag{5.5}$$

where ρ^* is the average density of the foam and ρ_{s} is the density of the solid metal. For our unit cells this can also be written:

$$\rho_{\mathrm{rel}} = \frac{V_{\mathrm{s}}}{V_{\mathrm{uc}}}\,, \tag{5.6}$$

where V_{uc} is the total volume of the unit cell and V_{s} is the volume of the solid material in the unit cell. The volume of the solid material is simply:

$$V_{\mathrm{s}} = A_{\mathrm{SE}}\, t\,, \tag{5.7}$$

where A_{SE} is the area of the surface in a unit cell as reported by Surface Evolver and t is the shell thickness. This is only an approximation since it implies an overlapping of the faces along the edges. However, for thin faces the resulting error is negligible.

From(5.6) and (5.7) we get:

$$t = \rho_{\mathrm{rel}}\, \frac{V_{\mathrm{uc}}}{A_{\mathrm{SE}}} \tag{5.8}$$

The appropriate values for the Kelvin and the Weaire-Phelan unit cells (as defined in twointor.fe and phelanc.fe) are:

$$V_{\text{uc}} = 1.0 \qquad A_{\text{SE}} = 3.3427 \qquad \text{(Kelvin)} \tag{5.9}$$

$$V_{\text{uc}} = 8.0 \qquad A_{\text{SE}} = 21.1539 \qquad \text{(Weaire-Phelan)} \tag{5.10}$$

The shell thicknesses computed for the non-flat Kelvin and Weaire-Phelan models were also used for the flat models. Strictly speaking this is not correct, as the flat models have a slightly larger surface area. However, the difference is negligible.

Figures 5.10 and 5.11 show rendered images of the Kelvin and the Weaire-Phelan unit cells, respectively, with the appropriate shell thicknesses for six different relative densities.

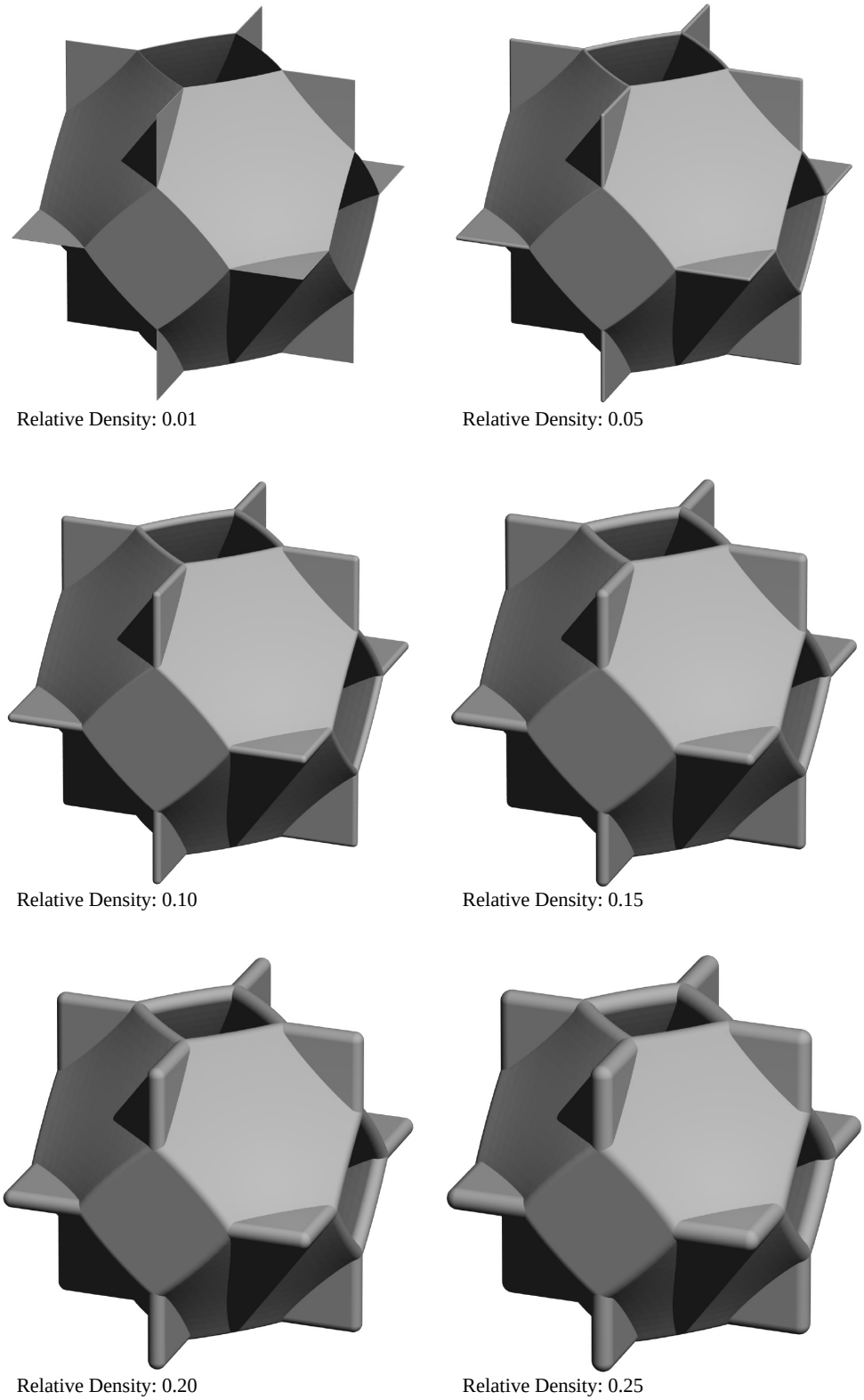

Figure 5.10: Kelvin unit cell with appropriate shell thicknesses for six different relative densities.

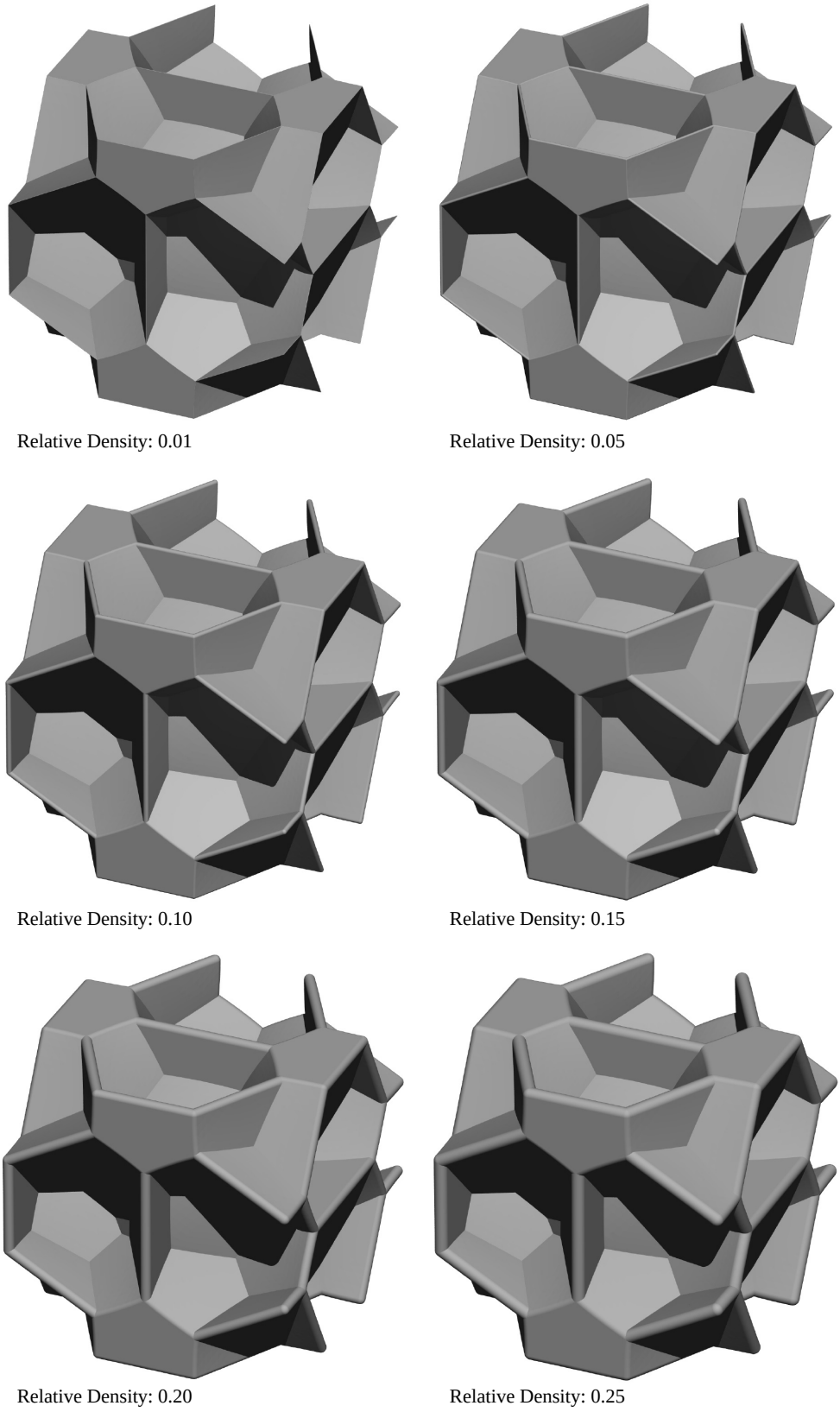

Figure 5.11: Weaire-Phelan unit cell with appropriate shell thicknesses for six different relative densities.

6 Prediction of the Linear Elastic Behavior

6.1 Introduction

In this chapter we assume that the bulk material is isotropic and linear elastic with:

$$E_\mathrm{s} = 70000\,\mathrm{MPa} \tag{6.1}$$

$$\nu_\mathrm{s} = 0.3 \tag{6.2}$$

$$G_\mathrm{s} = \frac{E_\mathrm{s}}{2\,(1+\nu_\mathrm{s})} = 26923\,\mathrm{MPa} \tag{6.3}$$

The linear elastic behavior of the homogenized material is described by Hooke's Law. Using the stress tensor σ_{ij}, the strain tensor ε_{ij} and the tensor of elasticity E_{ijkl} Hooke's Law can be written in indical notation as:

$$\sigma_{ij} = E_{ijkl}\,\varepsilon_{kl} \tag{6.4}$$

E_{ijkl} is a fourth-rank tensor and has 81 components.

Often an alternative notation is used. With the vector of stress components[1] $\underset{\sim}{\sigma}$ and the vector of strain components $\underset{\sim}{\varepsilon}$:

$$\underset{\sim}{\sigma} = (\sigma_{11}, \sigma_{22}, \sigma_{33}, \sigma_{23}, \sigma_{31}, \sigma_{12})^T\,, \tag{6.5}$$

$$\underset{\sim}{\varepsilon} = (\varepsilon_{11}, \varepsilon_{22}, \varepsilon_{33}, \gamma_{23}, \gamma_{31}, \gamma_{12})^T\,, \tag{6.6}$$

Hooke's Law can be written:

$$\underset{\sim}{\sigma} = \underset{\approx}{\mathbf{E}}\,\underset{\sim}{\varepsilon}\,, \tag{6.7}$$

with the 6x6 elasticity matrix $\underset{\approx}{\mathbf{E}}$. The inverse of $\underset{\approx}{\mathbf{E}}$ is called the compliance matrix $\underset{\approx}{\mathbf{C}} = \underset{\approx}{\mathbf{E}}^{-1}$:

$$\underset{\sim}{\varepsilon} = \underset{\approx}{\mathbf{C}}\,\underset{\sim}{\sigma} \tag{6.8}$$

As $\underset{\approx}{\mathbf{E}}$ and $\underset{\approx}{\mathbf{C}}$ are symmetric they have 21 independent components. So in the most general case 21 components are needed to describe the elastic behavior of a material.

[1] Different conventions for the ordering of the subscripts are used. The one used here is that of Nye [Nye, 1985].

As the symmetry of the material increases, fewer moduli are required. In the case of orthotropic symmetry (meaning that the structure has three perpendicular mirror planes) nine moduli are required – for example: E_1, E_2, E_3, G_{23}, G_{31}, G_{12}, ν_{12}, ν_{13}, ν_{23}. If the coordinate axes are aligned with the material axes the compliance matrix $\underset{\approx}{\mathbf{C}}$ for such an orthotropic material is:

$$\underset{\approx}{\mathbf{C}} = \begin{bmatrix} \frac{1}{E_1} & -\frac{\nu_{12}}{E_1} & -\frac{\nu_{13}}{E_1} & 0 & 0 & 0 \\ -\frac{\nu_{12}}{E_1} & \frac{1}{E_2} & -\frac{\nu_{23}}{E_2} & 0 & 0 & 0 \\ -\frac{\nu_{13}}{E_1} & -\frac{\nu_{23}}{E_2} & \frac{1}{E_3} & 0 & 0 & 0 \\ 0 & 0 & 0 & \frac{1}{G_{23}} & 0 & 0 \\ 0 & 0 & 0 & 0 & \frac{1}{G_{31}} & 0 \\ 0 & 0 & 0 & 0 & 0 & \frac{1}{G_{12}} \end{bmatrix} \tag{6.9}$$

As the Kelvin and the Weaire-Phelan foam both have cubic symmetry, the elastic moduli are the same in all three directions:

$$E_1 = E_2 = E_3 = E \tag{6.10}$$

$$G_{23} = G_{31} = G_{12} = G \tag{6.11}$$

$$\nu_{12} = \nu_{13} = \nu_{23} = \nu \tag{6.12}$$

So for the Kelvin and the Weaire-Phelan foam the compliance matrix can be written:

$$\underset{\approx}{\mathbf{C}} = \begin{bmatrix} \frac{1}{E} & -\frac{\nu}{E} & -\frac{\nu}{E} & 0 & 0 & 0 \\ -\frac{\nu}{E} & \frac{1}{E} & -\frac{\nu}{E} & 0 & 0 & 0 \\ -\frac{\nu}{E} & -\frac{\nu}{E} & \frac{1}{E} & 0 & 0 & 0 \\ 0 & 0 & 0 & \frac{1}{G} & 0 & 0 \\ 0 & 0 & 0 & 0 & \frac{1}{G} & 0 \\ 0 & 0 & 0 & 0 & 0 & \frac{1}{G} \end{bmatrix} \tag{6.13}$$

This looks exactly like the compliance matrix of an isotropic material. However, we have three independent moduli (E, G and ν) and not two, like in the case of an isotropic material. For an isotropic material the condition $G = \frac{E}{2(1+\nu)}$ must be fulfilled. Here, this is not the case.

6.2 Determination of the Elastic Moduli

In the general case it is necessary to calculate six load cases (three normal stress and three shear stress load cases) to determine the elasticity matrix of a unit cell model.

The first load case is the application of a normal stress in the 1-direction. So the homogenized stress vector is chosen to be: $\underset{\sim}{\sigma} = (1\,\mathrm{MPa}, 0, 0, 0, 0, 0)^T$. Next, the

appropriate concentrated load is calculated and applied to the respective master node. After the linear finite element analysis the macroscopic strain vector $\underset{\sim}{\varepsilon}$ is calculated from the displacements of the master nodes. Inserting $\underset{\sim}{\sigma}$ and $\underset{\sim}{\varepsilon}$ into Equation (6.7) yields six equations for the unknown components of the elasticity matrix.

The procedure is repeated for the remaining load cases. Thus, 36 equations for the 36 components of the elasticity matrix are obtained.

Due to the cubic symmetry of the Kelvin and the Weaire-Phelan foam the application of effective normal stresses in 2- and 3-directions yields the same result as normal stress in 1-direction. The same applies to shear stresses. So it was sufficient to calculate two load cases: one normal stress and one shear stress case.

6.3 Results

The analysis described above was carried out for 17 different relative densities in the range from 0.001 to 0.25 for both the Kelvin and the Weaire-Phelan structures. Five different mesh refinements were used as shown in Figures 5.6 to 5.9. Moreover, "flat" models (see Section 5.2.2) were analyzed for comparison. The effective elastic moduli reported in this sections characterize the elastic response of the material along the principal material axes.

6.3.1 Kelvin Foam

Figure 6.1 shows the ratios E^*/E_s and G^*/E_s plotted over the relative density for the five different mesh refinements. Figure 6.2 shows Poisson's ratio ν^*. (Symbols with a superscript "$*$" refer to effective properties of the foam, whereas symbols with a subscript "s" refer to properties of the solid material.) With increasing mesh refinement the model becomes softer and Poisson's ratio increases. Obviously, a fine mesh is required for obtaining reliable results. The moduli predicted with mesh refinements 4 and 5 differ by less than 1%.

Figures 6.3 and 6.4 give a comparison of the moduli of the non-flat and the flat Kelvin models, respectively. The sudden increase of Poisson's ratio for relative densities below 4% only occurs with the non-flat model. The two figures also show results for a flat Kelvin model published by Grenestedt [Grenestedt, 1999]. The results from our flat model are in good agreement with the results obtained by Grenestedt.

Figure 6.5 shows Young's modulus and shear modulus, E^* and G^*, of the non-flat model divided by the corresponding moduli of the flat model. Both ratios rapidly decrease for relative densities below 4%.

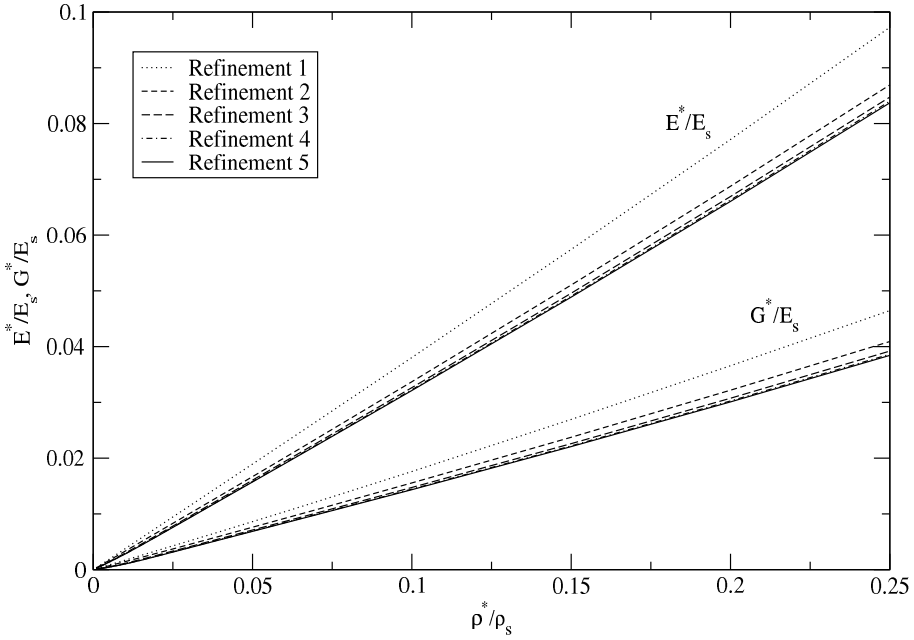

Figure 6.1: Relative Young's modulus E^*/E_s and relative shear modulus G^*/E_s of the Kelvin foam for different mesh refinements.

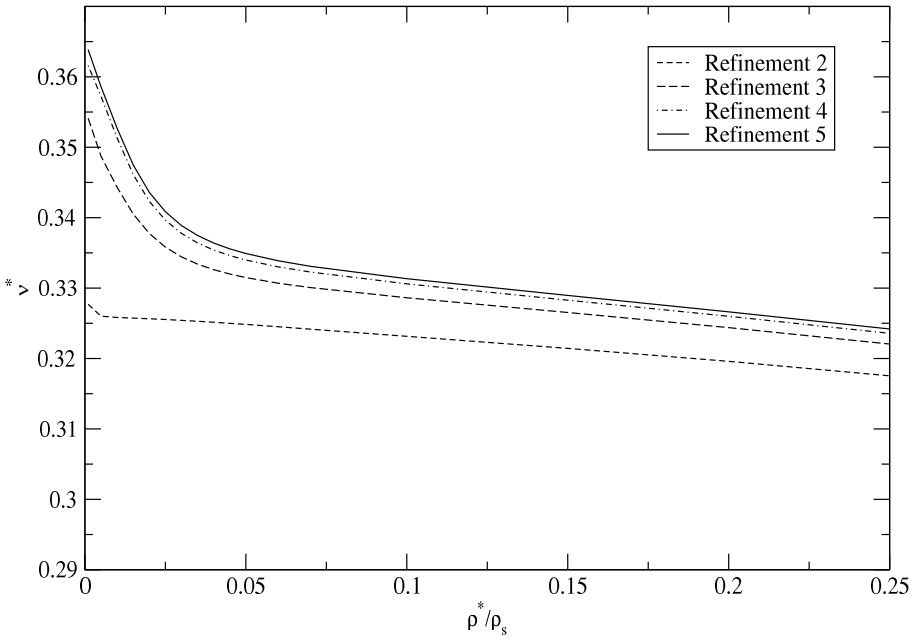

Figure 6.2: Poisson's ratio of the Kelvin foam for different mesh refinements.

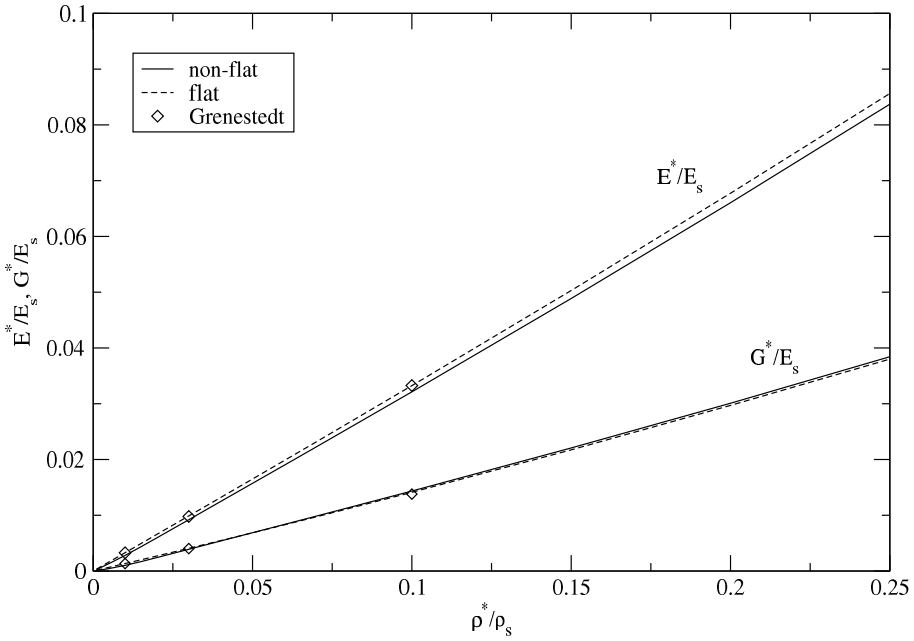

Figure 6.3: Comparison of the relative Young's modulus E^*/E_s and the relative shear modulus G^*/E_s of the non-flat and flat Kelvin foams (mesh refinement 5).

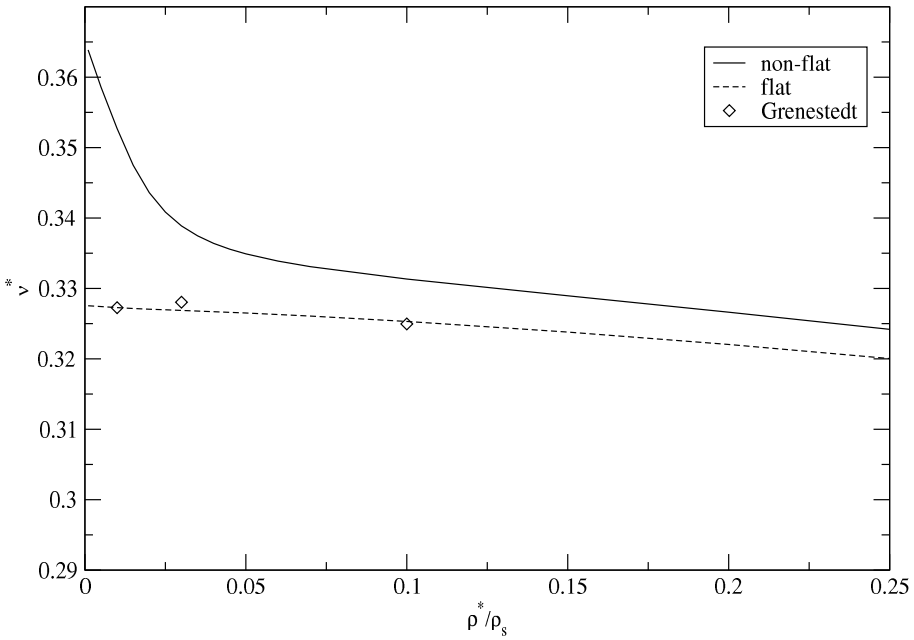

Figure 6.4: Comparison of Poisson's ratio of the non-flat and flat Kelvin foams (mesh refinement 5).

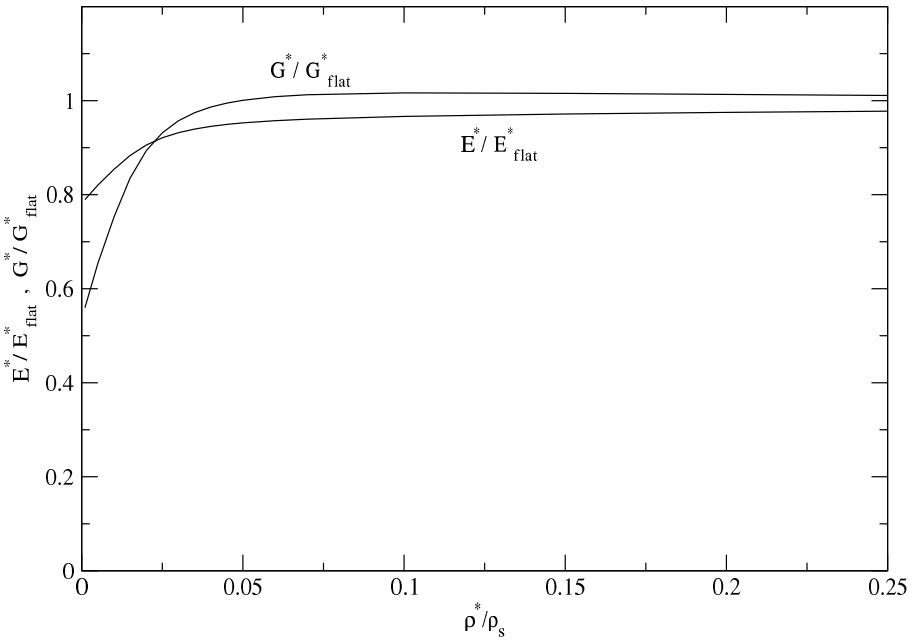

Figure 6.5: Young's modulus and shear modulus of the non-flat Kelvin foam divided by the corresponding moduli of the flat foam (mesh refinement 5).

In order to understand what is happening for relative densities below 4% Figures 6.6 to 6.9 compare the deformed configurations of the Kelvin Cells for high ($\rho^*/\rho_s = 0.1$) and for low ($\rho^*/\rho_s = 0.02$) relative densities.

Figure 6.6 shows a Kelvin Cell deformed by compressive loading for high relative density. Figures 6.7 shows the deformation under compressive loading for low relative density. The deformations of the hexagonal faces perpendicular to the plane of these faces are now large compared to the overall deformation of the cell. Of course the deformations have been scaled up for visualization. Linear analysis assumes that equilibrium can be established on the undeformed structure. Deformations as large as the ones shown in Figure 6.7 would violate this assumption.

It is interesting to compare the deformations of the hexagonal faces with the initial distortions of these faces that can be seen in Figures 3.5 and 3.7 on page 23 and 24. The diagonals of the hexagonal faces that can be seen in Figure 6.7(b) are straight in the unloaded configuration.

The flat Kelvin model *always* deforms like the "high density" Kelvin Cell in Figure 6.6 even if the relative density is very low.

Figures 6.8 and 6.9 show the deformations of the Kelvin cell under shear loading for high and low relative densities. The different behavior with respect to high and low relative densities is similar to the behavior under compressive loading. Again the flat Kelvin model deforms like the "high density" Kelvin Cell in Figure 6.8 even if the relative density is low.

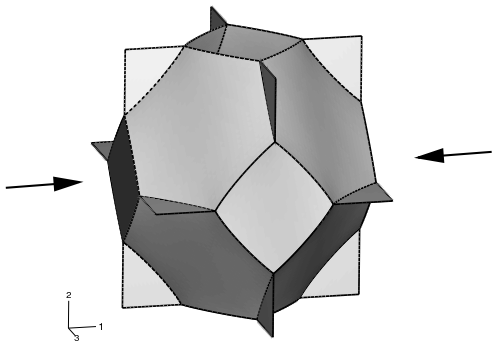

Figure 6.6: Deformed configuration of a Kelvin model for high relative density ($\rho^*/\rho_s = 0.1$) under compressive loading (Deformation scale factor: 120).

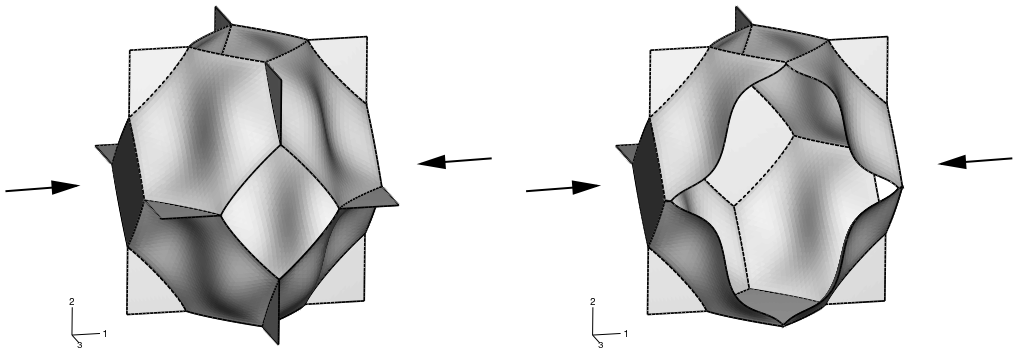

(a) Whole Kelvin Cell

(b) In order to show the deformation of the hexagonal faces the cell was sectioned perpendicularly to the 3-axis.

Figure 6.7: Deformed configuration of a Kelvin model for low relative density ($\rho^*/\rho_s = 0.02$) under compressive loading (Deformation scale factor: 35).

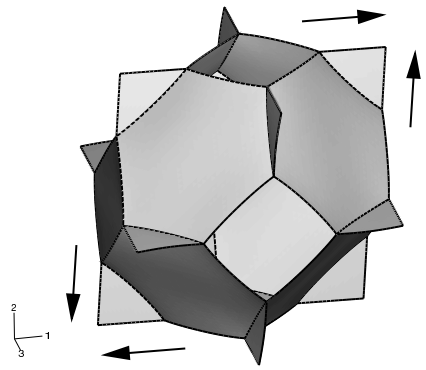

Figure 6.8: Deformed configuration of a Kelvin model for high relative density ($\rho^*/\rho_s = 0.1$) under shear loading (Deformation scale factor: 75).

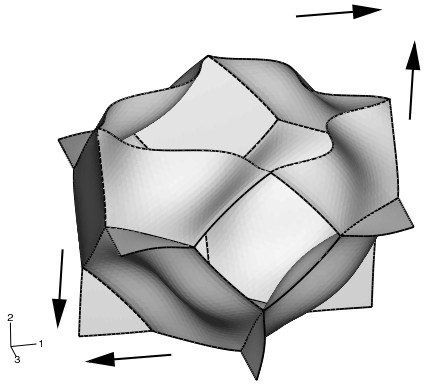

Figure 6.9: Deformed configuration of a Kelvin model for low relative density ($\rho^*/\rho_s = 0.02$) under shear loading; In order to show the deformations of the hexagonal faces the cell was sectioned perpendicularly to the 2-axis (Deformation scale factor: 15).

6.3.2 Weaire-Phelan Foam

Figures 6.10 to 6.14 show the results obtained for the Weaire-Phelan foams. From Figures 6.10 and 6.11 we can see that again a fine mesh is required for obtaining reliable results. The moduli predicted with mesh refinement four and five differ by less than 1%.

Figures 6.12 and 6.13 give a comparison of the moduli of the non-flat and the flat Weaire-Phelan models, respectively. Figure 6.14 shows Young's modulus and shear modulus, E^* and G^*, of the non-flat model divided by the corresponding moduli of the flat model. Both ratios rapidly decrease for relative densities below 4%.

Figures 6.15 to 6.20 show the deformations of the Weaire-Phelan foam models with high and low relative densities. Again it is interesting to compare the deformations with the initial distortions of the faces that can be seen in Figures 3.15 and 3.16 on page 31 and 32, respectively.

6.3.3 Comparison Kelvin - Weaire-Phelan

Finally, we will compare the results obtained for the Kelvin and Weaire-Phelan foam models. Figure 6.21 shows Young's moduli and shear moduli of both foams. Figure 6.22 shows the Young's modulus and shear modulus of the Weaire-Phelan foam divided by the corresponding moduli of the Kelvin foam.

For high relative densities the Weaire-Phelan foam is stiffer than the Kelvin foam regarding Young's modulus and softer than the Kelvin foam regarding shear modulus. For low relative densities it is the other way round – the Weaire Phelan foam is softer than the Kelvin foam regarding Young's modulus and stiffer than the Kelvin foam regarding shear modulus.

Poisson's ratio is lower for the Weaire-Phelan foam than for the Kelvin foam – compare Figures 6.4 and 6.13.

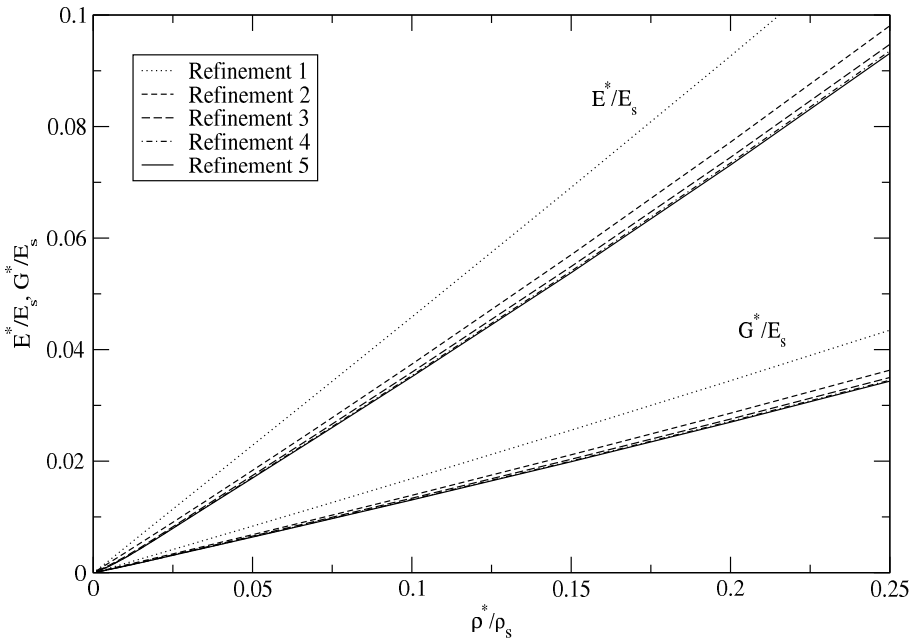

Figure 6.10: Relative Young's modulus E^*/E_s and relative shear modulus G^*/E_s of the Weaire-Phelan foam for different mesh refinements.

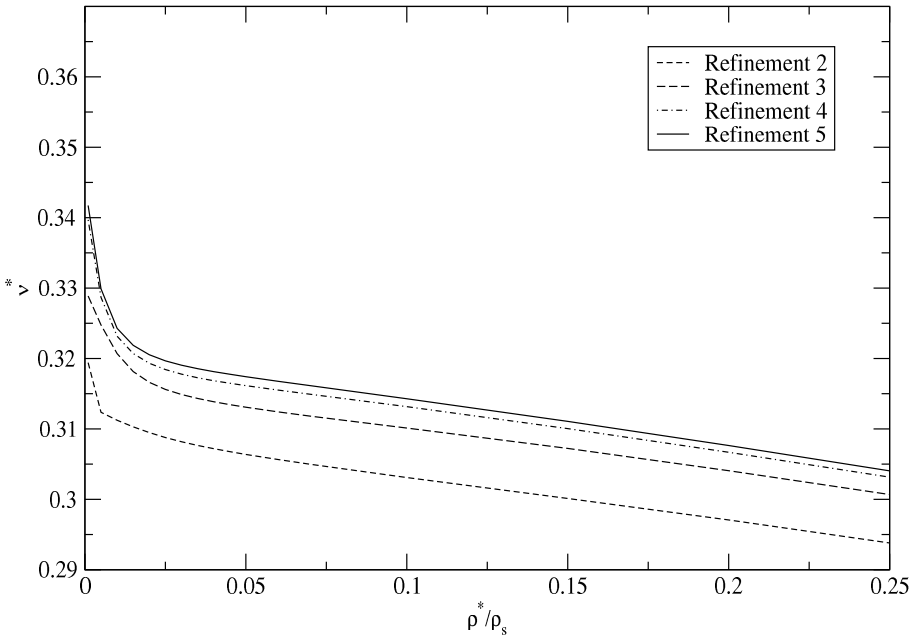

Figure 6.11: Poisson's ratio of the Weaire-Phelan foam for different mesh refinements.

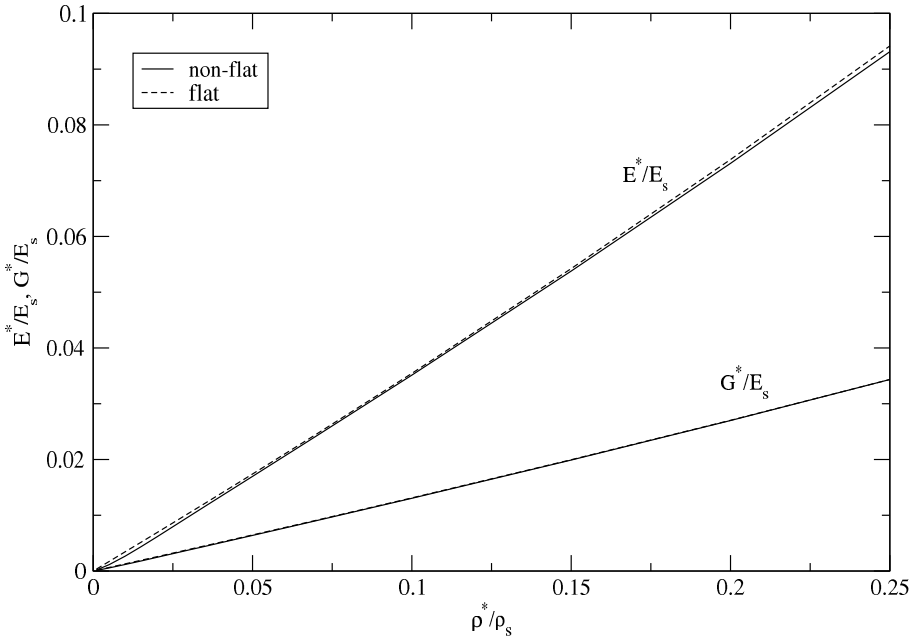

Figure 6.12: Comparison of the relative Young's modulus E^*/E_s and the relative shear modulus G^*/E_s of the non-flat and flat Weaire-Phelan foams (mesh refinement 5).

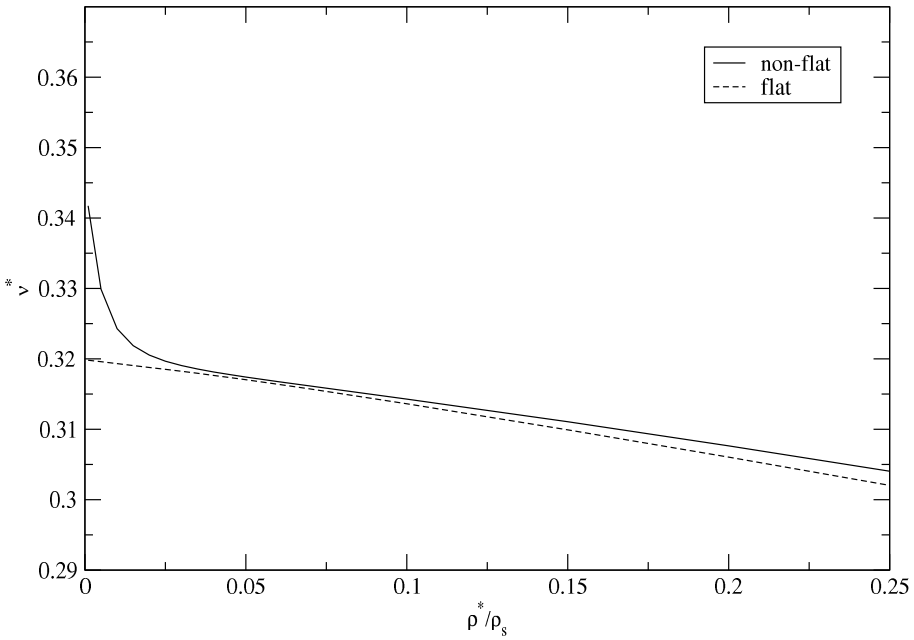

Figure 6.13: Comparison of Poisson's ratio of the non-flat and flat Weaire-Phelan foams (mesh refinement 5).

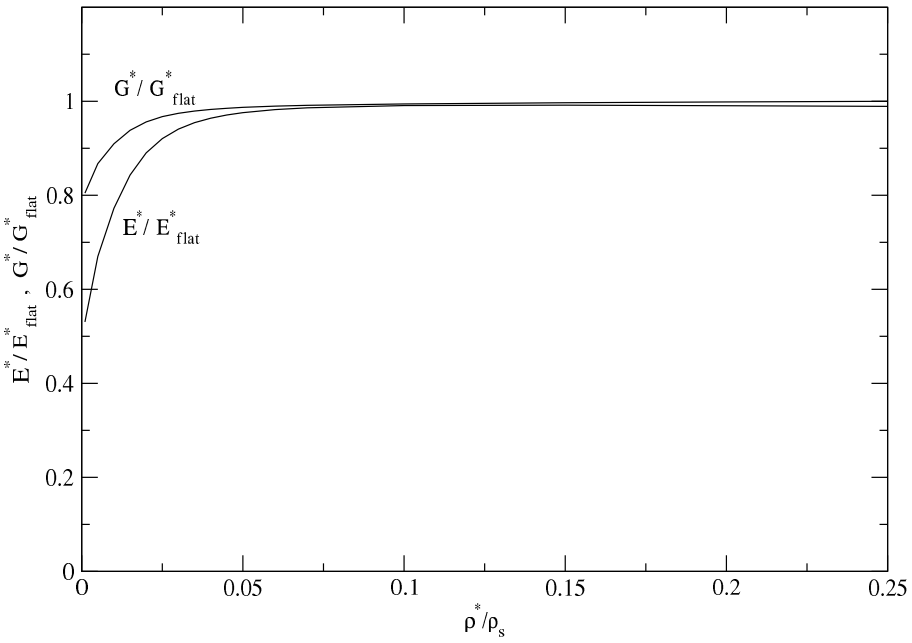

Figure 6.14: Young's modulus and shear modulus of the non-flat Weaire-Phelan foam divided by the corresponding moduli of the flat model (mesh refinement 5).

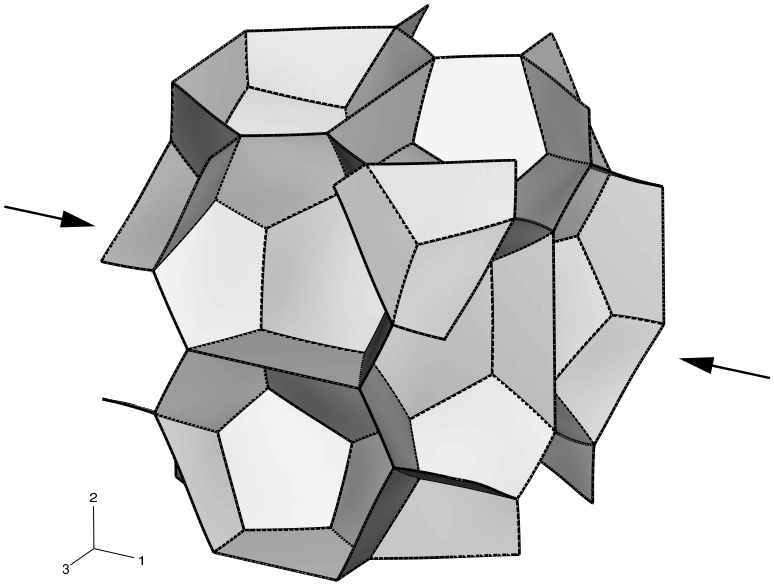

Figure 6.15: Deformed configuration of a Weaire-Phelan model for high relative density ($\rho^*/\rho_s = 0.1$) under compressive loading (Deformation scale factor: 120).

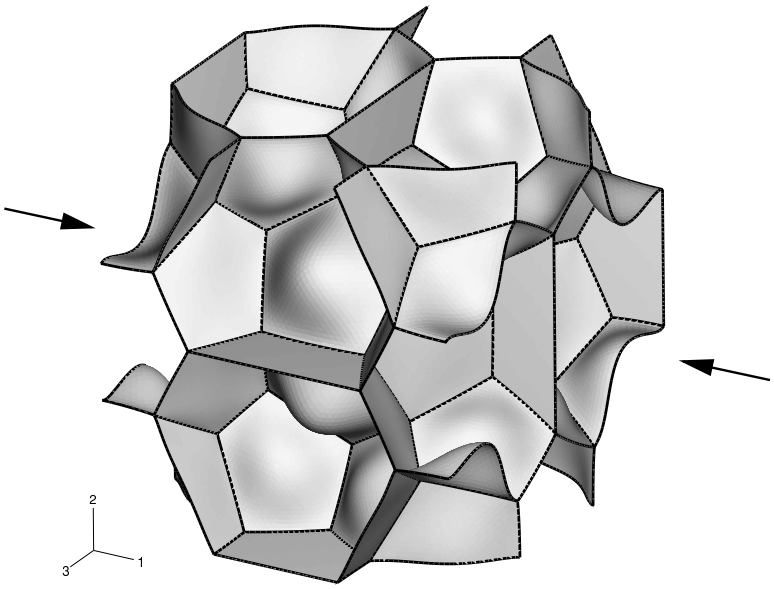

Figure 6.16: Deformed configuration of a Weaire-Phelan model for low relative density ($\rho^*/\rho_s = 0.02$) under compressive loading (Deformation scale factor: 25).

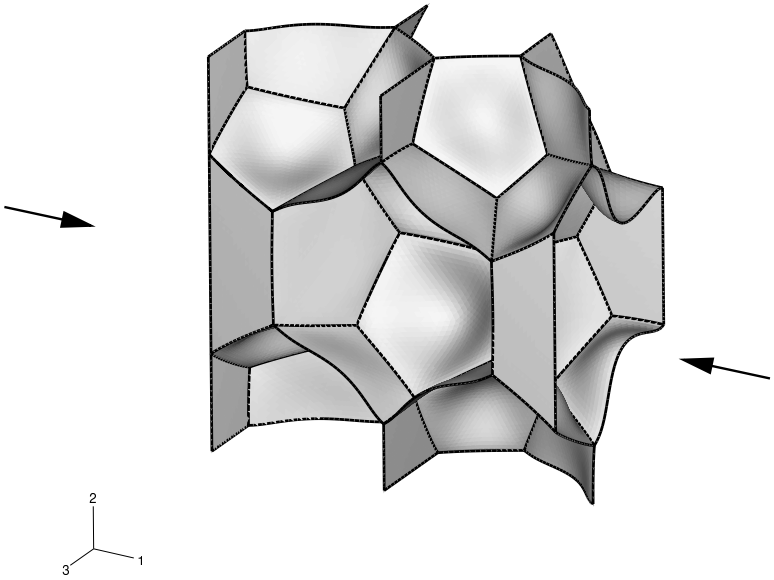

Figure 6.17: Deformed configuration of a Weaire-Phelan model for low relative density ($\rho^*/\rho_s = 0.02$) under compressive loading. The structure was sectioned perpendicularly to the 3-axis (Deformation scale factor: 25).

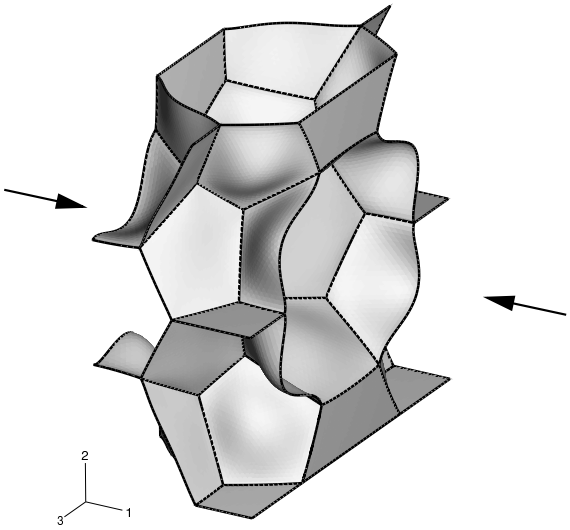

Figure 6.18: Deformed configuration of a Weaire-Phelan model for low relative density ($\rho^*/\rho_s = 0.02$) under compressive loading. The structure was sectioned perpendicularly to the 1-axis (Deformation scale factor: 25).

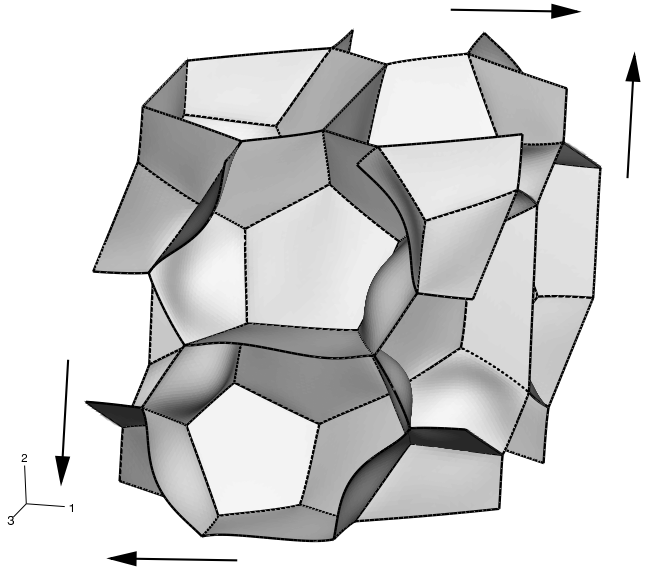

Figure 6.19: Deformed configuration of a Weaire-Phelan model for low relative density ($\rho^*/\rho_s = 0.02$) under shear loading (Deformation scale factor: 20).

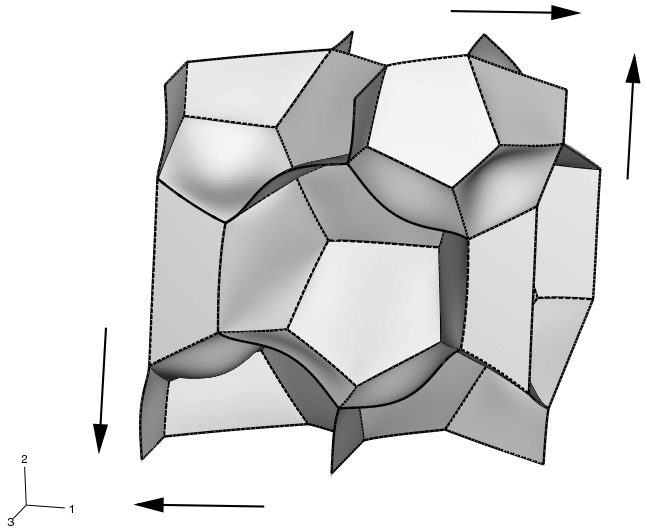

Figure 6.20: Deformed configuration of a Weaire-Phelan model for low relative density ($\rho^*/\rho_s = 0.02$) under shear loading. The structure was sectioned perpendicularly to the 3-axis (Deformation scale factor: 20).

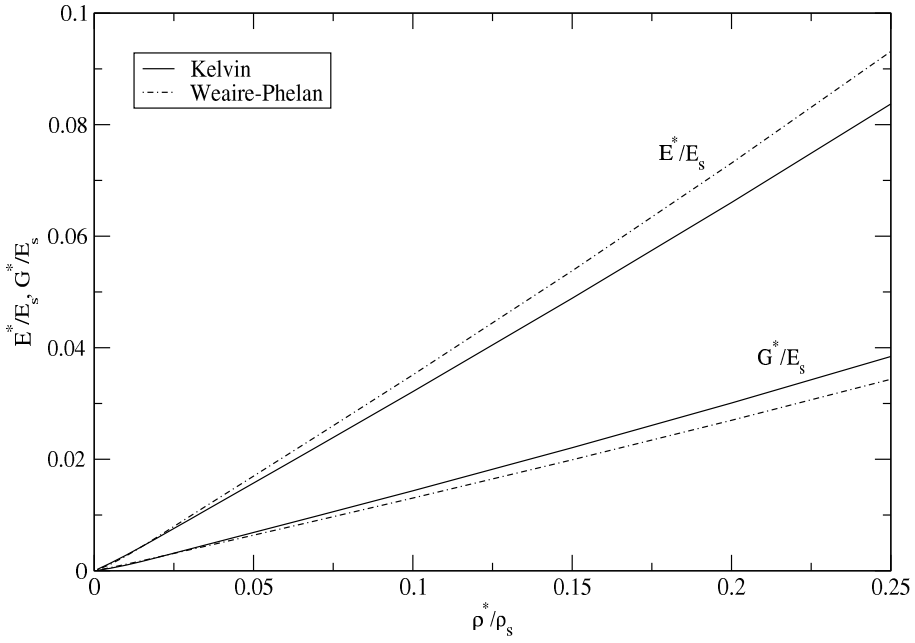

Figure 6.21: Comparison of the relative Young's moduli E^*/E_s and the relative shear moduli G^*/E_s of the Kelvin and Weaire-Phelan models (mesh refinement 5).

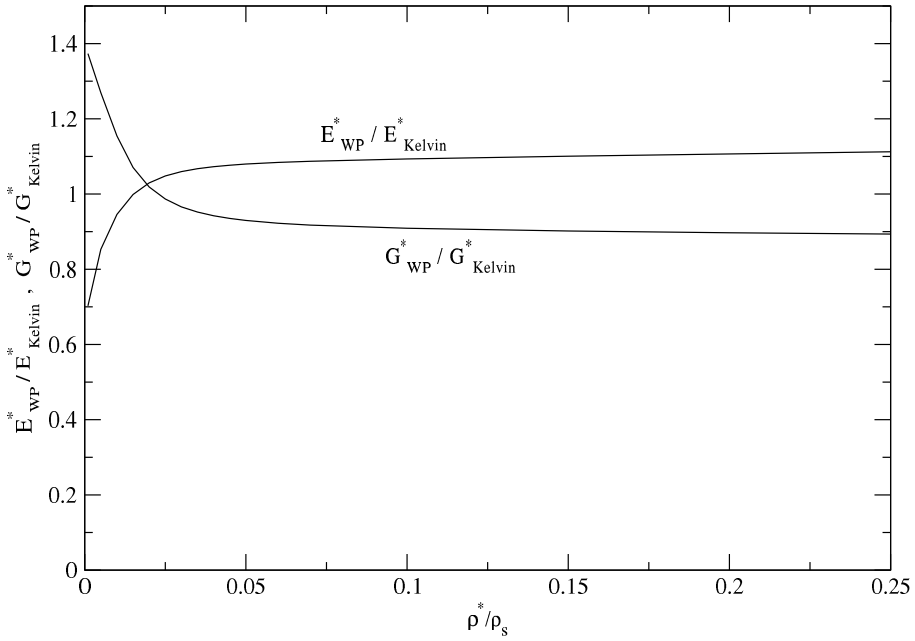

Figure 6.22: Young's modulus and shear modulus of the Weaire-Phelan foam divided by the corresponding moduli of the Kelvin foam (mesh refinement 5).

6.4 Comparison with a Curved Beam

In this section we will try to explain the results presented in the previous sections by investigating the elastic behavior of a slightly curved beam under compressive loading. The beam has a length of $l = 1\,\mathrm{m}$ and a rectangular cross-section of height $h = 0.01\,\mathrm{m}$, width $b = 0.01\,\mathrm{m}$, area $A = bh$ and moment of inertia $I = bh^3/12$. A compressive force $F = 100\,\mathrm{N}$ is applied to the beam. The material is linear elastic with a Young's modulus $E = 70\,\mathrm{GPa}$.

The initial, undeformed shape of the beam is described by the parabola:

$$w_0(x) = w_{0\max}\left[1 - \left(x - \frac{l}{2}\right)^2 \frac{4}{l^2}\right] \tag{6.14}$$

where $w_{0\max}$ is maximum deviation in the middle of the beam. We chose $w_{0\max} = 0.01\,\mathrm{m}$ (1% of the length) as this is the same magnitude as the one that we have found for the non-planar faces of the Kelvin and the Weaire-Phelan foam (see Section 3.2 and 3.3). Figure 6.23 shows the initial shape of the beam.

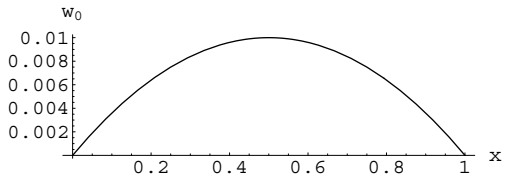

Figure 6.23: Initial shape of the beam.

The bending moment is:

$$M(x) = F\,w_0(x) \tag{6.15}$$

So the governing differential equation for the deflection $w(x)$ becomes:

$$w''(x)\,EI + F\,w_0(x) = 0 \tag{6.16}$$

With boundary conditions $w(0) = 0$ and $w(l) = 0$ the following solution is found:

$$w(x) = \frac{4\,F\,w_{0\max}\,l^2}{E\,bh^3}\left[\left(\frac{x}{l}\right)^4 - 2\left(\frac{x}{l}\right)^3 + \left(\frac{x}{l}\right)\right] \tag{6.17}$$

Figure 6.24 shows the solution $w(x)$, the initial shape $w_0(x)$ and the deformed configuration $w_0(x) + w(x)$.

The axial strain of a straight beam under compressive loading is:

$$\varepsilon = \frac{-F}{EA} = \frac{-F}{E\,bh} \tag{6.18}$$

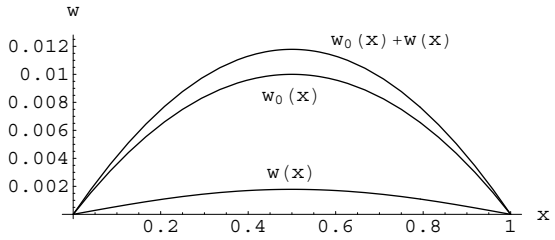

Figure 6.24: Initial shape $w_0(x)$ and solution $w(x)$.

For the length change of a straight beam follows:

$$\Delta l_{\text{straight}} = l\,\varepsilon = \frac{-F\,l}{E\,bh} \tag{6.19}$$

The length change of the curved beam considering the initial curvature and the axial stiffness is:

$$\Delta l_{\text{curved}} = \int_0^l \left[1 - \frac{1}{2}\left(\frac{dw_0}{dx}\right)^2\right] dx - \int_0^l \left[(1+\varepsilon)\left(1 - \frac{1}{2}\left(\frac{dw_0}{dx} + \frac{dw}{dx}\right)^2\right)\right] dx \tag{6.20}$$

In Figure 6.25 the ratio $\Delta l_{\text{curved}}/\Delta l_{\text{straight}}$ is plotted as a function of the height h of the rectangular cross-section.

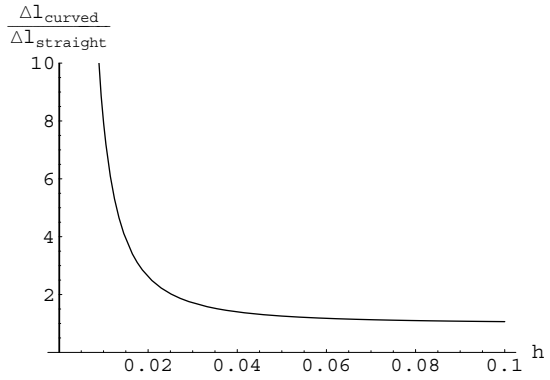

Figure 6.25: Ratio $\Delta l_{\text{curved}}/\Delta l_{\text{straight}}$ plotted over the height h of the cross-section.

For large values of h the ratio is close to 1, indicating that the initial curvature of the beam does not affect the stiffness of relatively thick beams. However, for small values of h the ratio becomes large and the stiffness of the beam is, therefore, reduced. When the height of the beam equals the maximum deviation ($h = w_{0\max} = 0.01\,\text{m}$) the stiffness of the straight beam is 7.95 times higher than the stiffness of the curved beam. When the height of the beam equals twice the maximum deviation

($h = 2\,w_{0\max} = 0.02\,\mathrm{m}$) the stiffness of the straight beam is 2.62 times higher than the stiffness of the curved beam.

Noting the mechanical analogy between the curved beam and the curved cell walls we conclude that the curvature of the cell walls reduces the stiffness noticeably for cell walls the thickness of which is below twice the maximum deviations reported in Sections 3.2 and 3.3. This condition is satisfied for Kelvin foams with a relative density smaller than 6.4% and Weaire-Phelan foams with a relative density smaller than 7.6%.

6.5 Orientation Dependence of Young's Modulus

The effective elastic moduli E^*, G^* and ν^* reported in the previous sections characterize the elastic response of the material along the principal material axes. In this section we are going to examine how the Young's modulus depends on direction for both the Kelvin and the Weaire-Phelan foams.

Using the compliance matrix $\underset{\approx}{\mathbf{C}}$ Hooke's law can be written as:

$$\underset{\sim}{\varepsilon} = \underset{\approx}{\mathbf{C}}\,\underset{\sim}{\sigma} \tag{6.21}$$

In the most general case $\underset{\approx}{\mathbf{C}}$ has 21 independent components. However, the cubic symmetry of the Kelvin and Weaire-Phelan foam simplifies the matrix to:

$$\underset{\approx}{\mathbf{C}} = \begin{bmatrix} C_{11} & C_{12} & C_{12} & 0 & 0 & 0 \\ C_{12} & C_{11} & C_{12} & 0 & 0 & 0 \\ C_{12} & C_{12} & C_{11} & 0 & 0 & 0 \\ 0 & 0 & 0 & C_{44} & 0 & 0 \\ 0 & 0 & 0 & 0 & C_{44} & 0 \\ 0 & 0 & 0 & 0 & 0 & C_{44} \end{bmatrix} \tag{6.22}$$

$$C_{11} = \frac{1}{E}; \quad C_{12} = -\frac{\nu}{E}; \quad C_{44} = \frac{1}{G}; \tag{6.23}$$

When we want to know Young's modulus E_n along any direction $\vec{n} = (n_x, n_y, n_z)^T$ we can transform the compliance matrices obtained in Section 6.3 to a new coordinate system so that the new x-axis equals $\vec{n}$. From the transformed compliance Matrix $\underset{\approx}{\hat{\mathbf{C}}}$ we can then calculate $E_n = 1/\hat{C}_{11}$. For the compliance matrix (6.22) this procedure yields:

$$E_n = \frac{1}{C_{11} + \frac{(2\,C_{12} - 2\,C_{11} + C_{44})(n_y{}^2 n_z{}^2 + n_z{}^2 n_x{}^2 + n_x{}^2 n_y{}^2)}{(n_x{}^2 + n_y{}^2 + n_z{}^2)^2}} \tag{6.24}$$

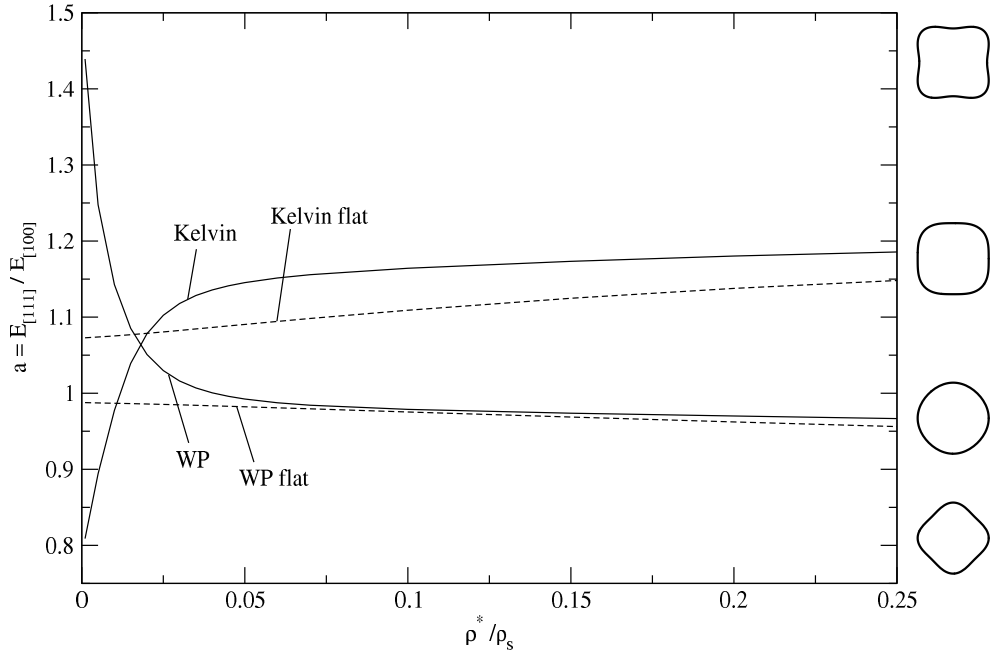

Figure 6.26: Anisotropy ratio $a = E_{[111]}/E_{[100]}$ plotted over the relative density for the four different models.

(We do not require that $|\vec{n}| = 1$.)

The extreme values of E_n in (6.24) are found for $\vec{n} = (1, 0, 0)^T$ and $\vec{n} = (1, 1, 1)^T$. We can conclude that the Young's moduli presented in the previous sections are extreme values (either maxima or minima), and that the other extreme value is found along the space diagonal $\vec{n} = (1, 1, 1)^T$.

We will denote the Young's modulus along $\vec{n} = (1, 0, 0)^T$ as $E_{[100]}$ and the Young's modulus along $\vec{n} = (1, 1, 1)^T$ as $E_{[111]}$. The ratio $a = E_{[111]}/E_{[100]}$ represents the anisotropy in a structure with cubic symmetry [Hosford, 1993]. From (6.24) follows:

$$a = \frac{E_{[111]}}{E_{[100]}} = \frac{3\,C_{11}}{C_{11} + 2\,C_{12} + C_{44}} \tag{6.25}$$

Figure 6.26 shows the ratio a plotted over the relative density for the Kelvin and Weaire-Phelan foam and the corresponding flat models. The values show a sudden change for relative densities lower than about 0.04.

Relative Densities Above 0.04

For the Kelvin foam a lies in the range of $1.14 - 1.19$. So the Young's modulus in the direction of the body diagonal ($E_{[111]}$) is up to 19% higher than the Young's

modulus in the direction of the principal material axes ($E_{[100]}$). Figure 6.28 shows how Young's modulus depends on direction for a Kelvin foam with $\rho^*/\rho_s = 0.25$. These plots were made using Equation (6.24). x, y and z denote the principal material axes. The three-dimensional plots display the Young's modulus according to the following grayscale: bright shades refer to large values, dark shades refer to small values of E_n. In addition to the three-dimensional plots cross-sections for $\varphi = 0°$ and $\varphi = 45°$ are shown. The corresponding coordinate system can be seen in Figure 6.27.

For the Weaire-Phelan foam a lies in the range of $0.965 - 1.0$. So for relative densities above 0.04 the Weaire-Phelan foam is virtually isotropic. Figure 6.29 shows how the Young's modulus depends on direction for a Weaire-Phelan foam with $\rho^*/\rho_s = 0.25$.

Figure 6.32 shows a two-dimensional plot of the Young's modulus plotted over the latitude θ for $\varphi = 0°$ and $\varphi = 45°$. The relative density is 0.1. At this density $a = 1.164$ for the Kelvin foam and $a = 0.975$ for the Weaire-Phelan foam.

Relative Densities Below 0.04

For the Kelvin foam a rapidly decreases for relative densities lower than about 0.04. Figure 6.30 shows how Young's modulus depends on direction for a (hypothetical) Kelvin foam with $\rho^*/\rho_s = 0.001$. For this foam $a \approx 0.81$.

For the Weaire-Phelan foam a rapidly increases for relative densities lower than about 0.04. Figure 6.31 shows how Young's modulus depends on direction for a (hypothetical) Weaire-Phelan foam with $\rho^*/\rho_s = 0.001$. For this foam $a \approx 1.44$.

The Flat Models

For the flat models a changes only slightly for all relative densities evaluated. For the flat Kelvin model a lies in the range of $1.07 - 1.15$, for the flat Weaire-Phelan model a lies in the range of $0.955 - 0.99$.

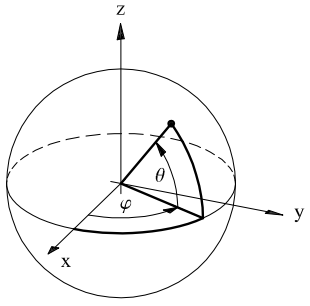

Figure 6.27: Spherical coordinate system; x, y and z denote the principal material axes.

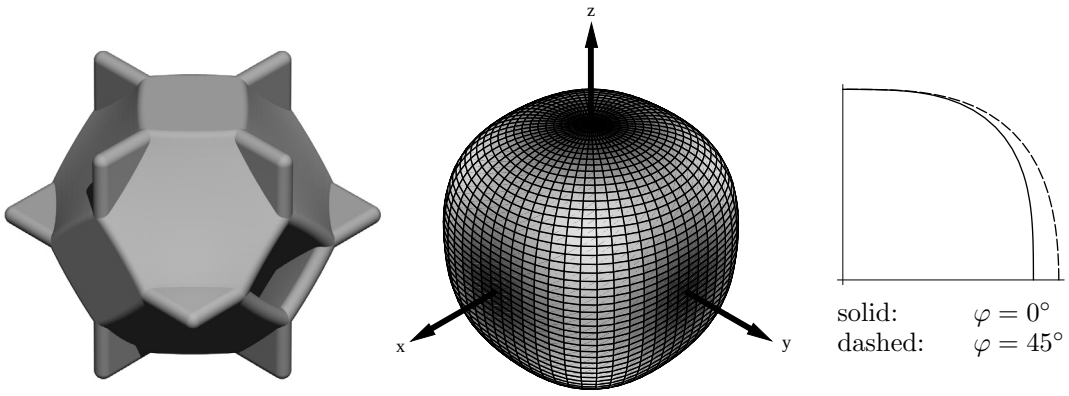

Figure 6.28: Orientation dependence of the Young's modulus for a Kelvin foam with $\rho^*/\rho_s = 0.25$. Bright shades refer to large values of E_n.

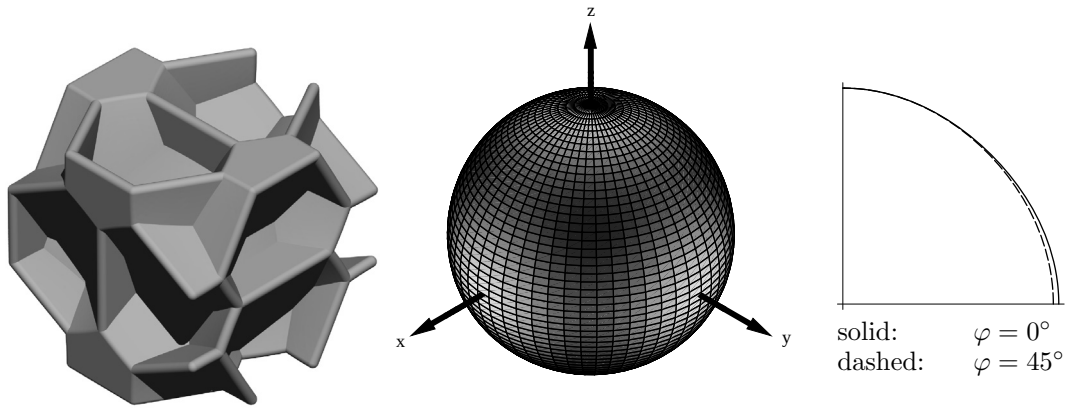

Figure 6.29: Orientation dependence of the Young's modulus for a Weaire-Phelan foam with $\rho^*/\rho_s = 0.25$. Bright shades refer to large values of E_n.

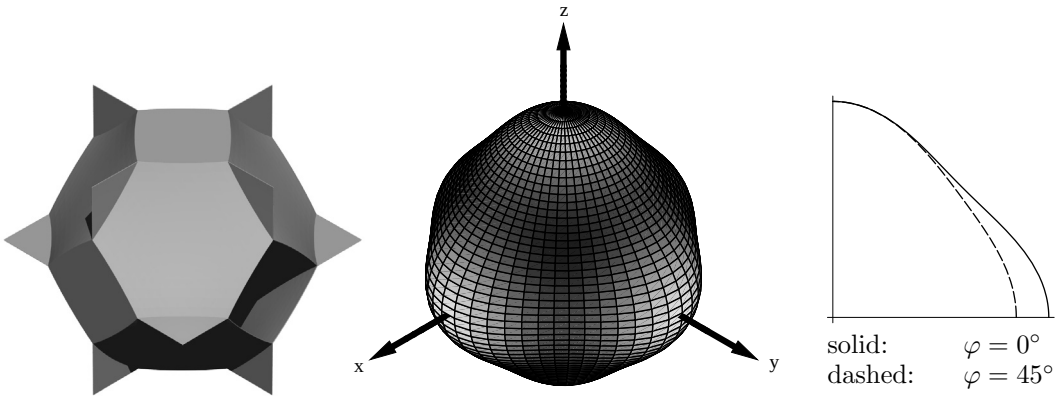

Figure 6.30: Orientation dependence of the Young's modulus for a Kelvin foam with $\rho^*/\rho_s = 0.001$. Bright shades refer to large values of E_n.

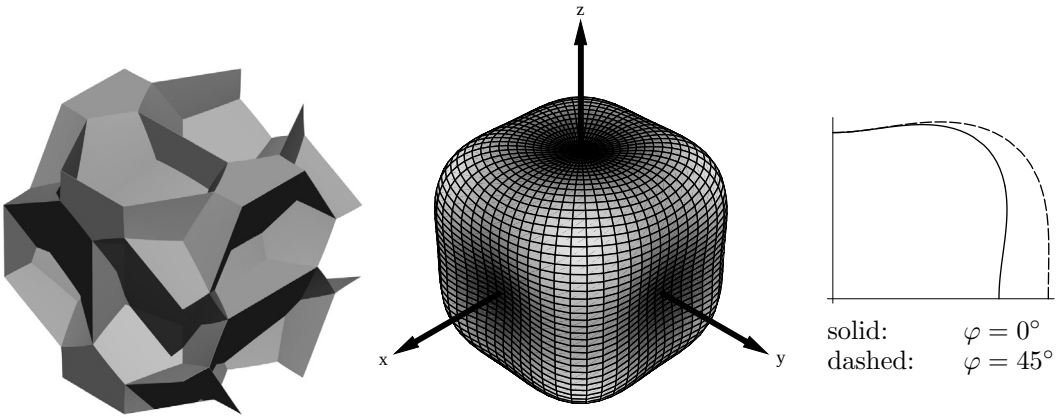

Figure 6.31: Orientation dependence of the Young's modulus for a Weaire-Phelan foam with $\rho^*/\rho_s = 0.001$. Bright shades refer to large values of E_n.

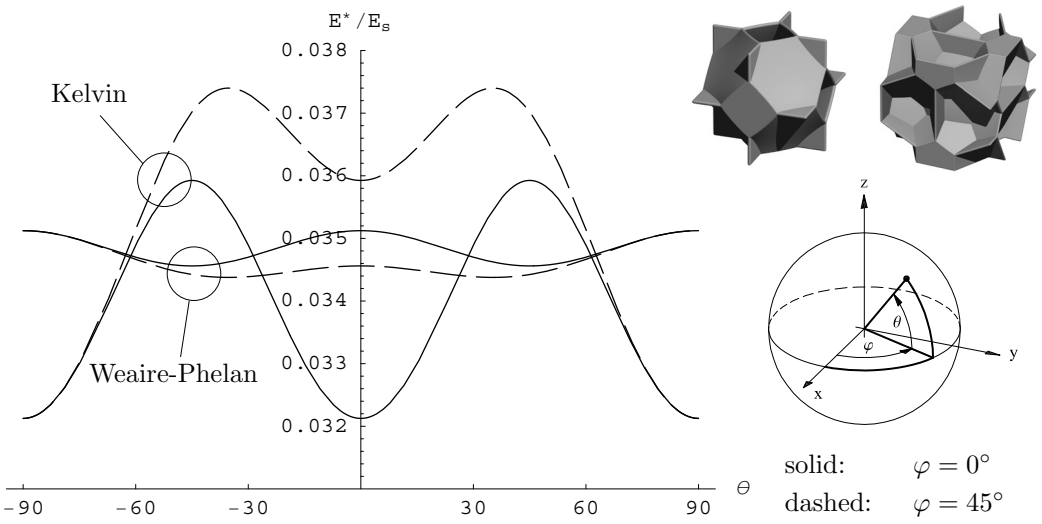

Figure 6.32: Young's modulus plotted over the latitude θ for both foams ($\rho^*/\rho_s = 0.1$).

7 Prediction of the Initial Yield Surface

In this chapter we will determine the initial yield surface of the Kelvin and Weaire-Phelan foam using nonlinear (elasto-plastic) Finite Element analysis. So first we will define an elasto-plastic material law for the bulk material.

7.1 Elasto-Plastic Material Law

We assume an elasto-plastic material with isotropic hardening. The uniaxial stress-strain diagram is described by:

$$\sigma_{xx} = \begin{cases} E\,\varepsilon_{xx} & \text{if } \sigma_{xx} \leq \sigma_{\mathrm{y}} \\ K\,\varepsilon_{xx}^{n} & \text{if } \sigma_{xx} > \sigma_{\mathrm{y}} \end{cases} \tag{7.1}$$

In (7.1) σ_{xx} is the true tensile stress, ε_{xx} is the total logarithmic strain, σ_{y} is the initial yield stress and E is Young's modulus. We chose the following values for the material parameters of the bulk material:

$$E = 70000\,\mathrm{MPa} \tag{7.2}$$
$$\nu = 0.3 \tag{7.3}$$
$$n = 0.1 \tag{7.4}$$
$$K = 486.96\,\mathrm{MPa} \tag{7.5}$$

K was chosen so that the ultimate engineering stress is $\sigma_{\mathrm{ult}} = 350\,\mathrm{MPa}$. The initial yield stress results as $\sigma_{\mathrm{y}} = 280.39\,\mathrm{MPa}$. In Figure 7.1 one curve shows the true stress plotted over logarithmic strain (Equation (7.1)), the other curve shows the engineering stress plotted over engineering strain. The extreme value of the latter curve is $\sigma_{\mathrm{ult}} = 350\,\mathrm{MPa}$.

In ABAQUS the elasto-plastic material is described by pairs of yield stress/plastic strain values. The corresponding section of the ABAQUS input file is shown in Figure 7.2.

In order to adequately capture the nonlinear material behavior 11 integration points were used through the shell section.

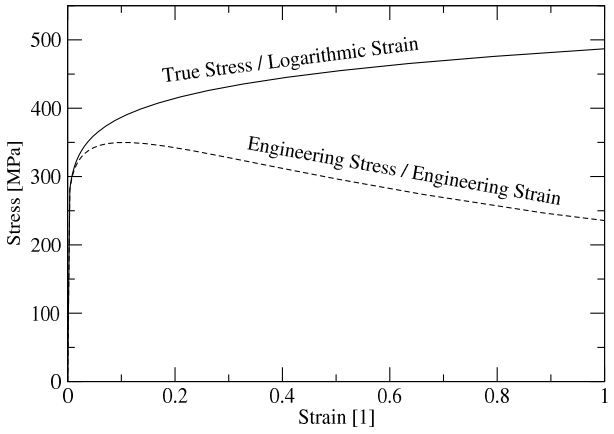

Figure 7.1: Stress-strain diagram as described by Equation (7.1)

```
** Elastic Modulus   E = 70000 MPa
** Strain Exponent   n = 0.1
** Ultimate Strength   = 350 MPa
**
** Stress Factor     K = 486.965 MPa
** Yield Strain        = 0.400559%
** Yield Stress        = 280.391 MPa
**
*MATERIAL, NAME=Matrix
*ELASTIC, TYPE=ISOTROPIC
70000, 0.3
*PLASTIC, HARDENING=ISOTROPIC
280.391, 0
281.083, 9.01106e-05
281.928, 0.000203049
282.952, 0.000344666
284.187, 0.000522332
285.666, 0.000745344
287.423, 0.00102542
289.491, 0.00137734
291.903, 0.00181973
294.685, 0.00237603
297.861, 0.00307572
301.444, 0.00395585
305.444, 0.00506286
309.861, 0.00645496
314.688, 0.008205
319.913, 0.0104041
325.521, 0.0131661
331.494, 0.0166335
337.813, 0.0209841
344.458, 0.0264403
351.413, 0.0332799
358.66, 0.04185
366.186, 0.0525845
373.98, 0.0660257
382.03, 0.0828513
390.331, 0.103909
398.875, 0.130256
407.659, 0.163218
416.68, 0.204448
425.936, 0.256015
435.427, 0.320503
445.154, 0.401143
455.119, 0.501975
465.322, 0.628047
475.768, 0.78567
486.46, 0.982732
497.401, 1.2291
508.595, 1.53708
520.047, 1.92211
531.762, 2.40342
543.745, 3.0051
556.002, 3.75724
568.537, 4.69746
581.357, 5.87277
594.469, 7.34195
607.877, 9.17847
```

Figure 7.2: ABAQUS input data for the elasto-plastic material.

7.2 Prediction of the Initial Yield Surface Using Linear Finite Element Analysis

In [Daxner, 2003] a method for the determination of the initial yield surface of cellular metals is described. It is assumed that fulfilling the von Mises yield criterion anywhere in the unit cell can be interpreted as the onset of both local *and* macroscopic yielding. First a loading path that is radial in macroscopic stress space is chosen and the corresponding macroscopic stresses are applied to a Finite Element unit cell model. Then for each integration point (where stresses are usually evaluated) a load multiplier is calculated that would cause yielding at the respective integration point. The smallest of the load multipliers is the critical global load multiplier associated with the first local fulfillment of the von Mises yield criterion.

It is not necessary to calculate hundreds of radial loading paths to obtain the whole yield surface. Since the method exclusively uses linear analysis the stress state for a given loading path can be calculated by superimposing stress states obtained by the analysis of unit load cases. Only one analysis per dimension of the macroscopic stress space is required. So the method is very efficient.

We intended to use the method described above to calculate the initial yield surface for the Kelvin and Weaire-Phelan unit cell models described in the previous chapters. However, an examination of the local stress fields for uniaxial compression showed that the maximum von Mises stress in the unit cell (found at the vertices) steadily increases with increasing mesh refinement! (For the different mesh refinements see Figures 5.6 to 5.9 on pages 53 to 56.) So for our models the yield surfaces calculated with the method described above would strongly depend on the mesh refinement, which is of course undesirable.

To overcome this problem we considered an alternative criterion for the onset of macroscopic yielding.

7.3 Prediction of the Initial Yield Surface Using Nonlinear Finite Element Analysis

7.3.1 Basic Approach

Our basic approach is not to consider the fulfillment of the von Mises Yield criterion at a single integration point as the onset of *macroscopic* yielding. Instead we define the onset of macroscopic yielding as the point where the equivalent plastic strain equals a prescribed value.

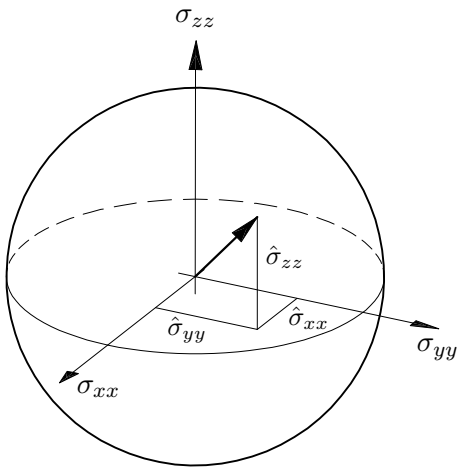

Figure 7.3: Direction in macroscopic stress space.

To simplify things we only consider combinations of macroscopic normal stresses aligned with the material axes.

First, we choose a direction in macroscopic stress space $(\hat{\sigma}_{xx}, \hat{\sigma}_{yy}, \hat{\sigma}_{zz})^T$ (see Figure 7.3). The macroscopic stresses applied to the unit cell are then:

$$\begin{pmatrix} \sigma_{xx} \\ \sigma_{yy} \\ \sigma_{zz} \end{pmatrix} = \lambda \begin{pmatrix} \hat{\sigma}_{xx} \\ \hat{\sigma}_{yy} \\ \hat{\sigma}_{zz} \end{pmatrix} \tag{7.6}$$

In (7.6) λ is the radius in stress space. (We require that $|(\hat{\sigma}_{xx}, \hat{\sigma}_{yy}, \hat{\sigma}_{zz})^T| = 1$.)

Using the elasto-plastic bulk material law from Section 7.1 we perform a nonlinear, force-controlled Finite Element analysis. The analysis stops when the ultimate load is reached. As results we get the displacements of the three master nodes as functions of the radius in stress space λ. From these displacements the engineering strains can be computed:

$$\varepsilon_{xx}(\lambda) = \frac{u_{\mathrm{SEB}}(\lambda)}{l} \qquad \varepsilon_{yy}(\lambda) = \frac{v_{\mathrm{NWB}}(\lambda)}{l} \qquad \varepsilon_{zz}(\lambda) = \frac{w_{\mathrm{SWT}}(\lambda)}{l} \tag{7.7}$$

An exemplary result is shown in Figure 7.4.

Next, we unload the structure from each increment of the loading path to calculate the residual plastic strains. It turned out that it is not necessary to compute nonlinear unloading curves. The unloading is very well described by Hooke's law with the moduli found in Chapter 6.

$$\underset{\sim}{\varepsilon}^{(\mathrm{el})} = \underset{\approx}{\mathbf{C}}\, \underset{\sim}{\sigma} \tag{7.8}$$

$$\underset{\sim}{\varepsilon}^{(\mathrm{pl})} = \underset{\sim}{\varepsilon} - \underset{\sim}{\varepsilon}^{(\mathrm{el})} \tag{7.9}$$

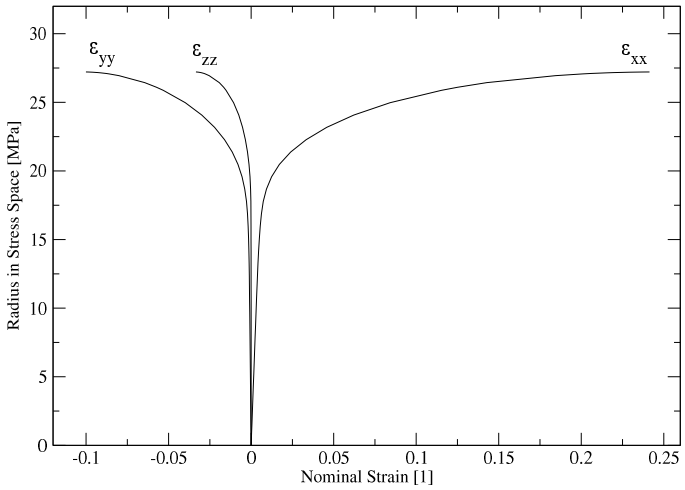

Figure 7.4: Engineering strains as functions of the radius in stress space.

As no macroscopic shear strains or shear stresses occur this yields:

$$\varepsilon_{xx}^{(\mathrm{el})} = \frac{1}{E}\,\sigma_{xx} - \frac{\nu}{E}\,(\sigma_{yy} + \sigma_{zz}) \tag{7.10}$$

$$\varepsilon_{yy}^{(\mathrm{el})} = \frac{1}{E}\,\sigma_{yy} - \frac{\nu}{E}\,(\sigma_{xx} + \sigma_{zz}) \tag{7.11}$$

$$\varepsilon_{zz}^{(\mathrm{el})} = \frac{1}{E}\,\sigma_{zz} - \frac{\nu}{E}\,(\sigma_{xx} + \sigma_{yy}) \tag{7.12}$$

$$\varepsilon_{xx}^{(\mathrm{pl})} = \varepsilon_{xx} - \varepsilon_{xx}^{(\mathrm{el})} \tag{7.13}$$

$$\varepsilon_{yy}^{(\mathrm{pl})} = \varepsilon_{yy} - \varepsilon_{yy}^{(\mathrm{el})} \tag{7.14}$$

$$\varepsilon_{zz}^{(\mathrm{pl})} = \varepsilon_{zz} - \varepsilon_{zz}^{(\mathrm{el})} \tag{7.15}$$

Now we define the equivalent plastic strain as:

$$\bar{\varepsilon}^{(\mathrm{pl})} = \sqrt{{\varepsilon_{xx}^{(\mathrm{pl})}}^2 + {\varepsilon_{yy}^{(\mathrm{pl})}}^2 + {\varepsilon_{zz}^{(\mathrm{pl})}}^2} \tag{7.16}$$

The equivalent plastic strain is again a function of the radius in stress space λ. An exemplary curve is shown in Figure 7.5 which corresponds to the strains shown in Figure 7.4.

We now define the onset of macroscopic yielding as the point where the equivalent plastic strain equals a prescribed value. As a plastic strain of 0.2% is commonly used to define the offset yield strength in tensile tests, we used $\boxed{\bar{\varepsilon}^{(\mathrm{pl})^*} = 0.2\%}$ for

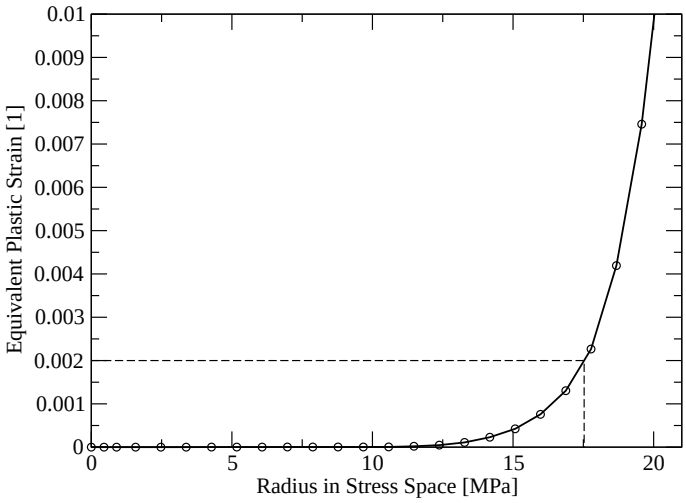

Figure 7.5: Equivalent plastic strain plotted over the radius in stress space.

the following calculations. From the curve in Figure 7.5 the critical radius in stress space λ^* can be calculated using linear interpolation ($\lambda^* \approx 17.5\,\mathrm{MPa}$).

With λ^* we have found one point of the initial yield surface. By repeating the procedure an arbitrary number of points can be calculated.

So next, we define a mesh on a unit sphere which is shown in Figure 7.6(a). Every vertex of this mesh corresponds to a direction in macroscopic stress space. The north and south poles of our mesh lie on the hydrostatic axis ($\sigma_{xx} = \sigma_{yy} = \sigma_{zz}$). Moreover, the mesh becomes finer towards the poles.

The mesh shown in Figure 7.6(a) has 812 vertices. So 812 nonlinear analyses would be required to compute the whole yield surface. However, due to the cubic symmetry of the Kelvin and Weaire-Phelan foams the initial yield surface will also have symmetries. For example it is obvious that the critical radius λ^* will be the same for tension along the x-axis (direction $(1,0,0)^T$) and tension along the y- or z-axis (direction $(0,1,0)^T$ and $(0,0,1)^T$).

It turns out that the three planes spanned by the hydrostatic axis and one of the axes σ_{xx}, σ_{yy} or σ_{zz} are planes of mirror symmetry. Thus, it is sufficient to perform the analysis for the sixth part of the unit sphere shown in Figure 7.6(b). The rest of the initial yield surface results from the mirror symmetries. So instead of 812 only 164 nonlinear analyses are required.

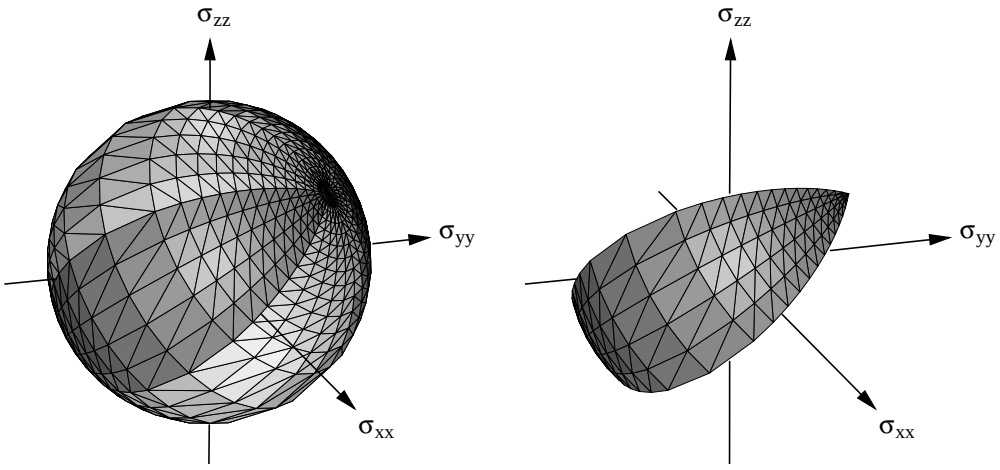

(a) Whole mesh (b) Sixth part of the mesh

Figure 7.6: Mesh on the unit sphere

7.3.2 Basic Results

We performed the calculations described in the previous section for the Kelvin and the Weaire-Phelan foams. Since the calculations are computationally expensive we limited ourselves to mesh refinement 4 (see Figures 5.6 and 5.8 on pages 53 and 55) and to two different relative densities: $\rho^*/\rho_s = 0.05$ and $\rho^*/\rho_s = 0.1$.

The calculations were performed on a Hewlett Packard RX2600, 900 MHz Itanium 2 with 9 GB RAM. The calculation of the yield surfaces for the Kelvin and Weaire-Phelan foam took about 22 and 90 hours respectively.

Figures 7.7 to 7.10 show visualizations of yield surfaces in the three-dimensional space spanned by the normal stress components (σ_{xx}, σ_{yy}, σ_{zz}), which are identical to the principal stress components in the considered three-axial loading scenario. The yield surfaces are based on Kelvin foam models of 5% (Figure 7.7) and 10% (Figure 7.8) relative density as well as Weaire-Phelan models of the same densities (Figures 7.9 and 7.10, respectively).

The shape of the yield surfaces is that of an ellipsoid which is aligned with the axis of purely hydrostatic stress states. The length of the ellipsoid is approximately two times as large as it's equatorial diameter. This indicates that the effective hydrostatic strength is well above the effective uniaxial strength of the respective materials.

For a more detailed discussion on the shape of the predicted yield surfaces several cross-sections and projections will be presented in the following. Before, simulation issues with regard to microstructural instabilities have to be discussed.

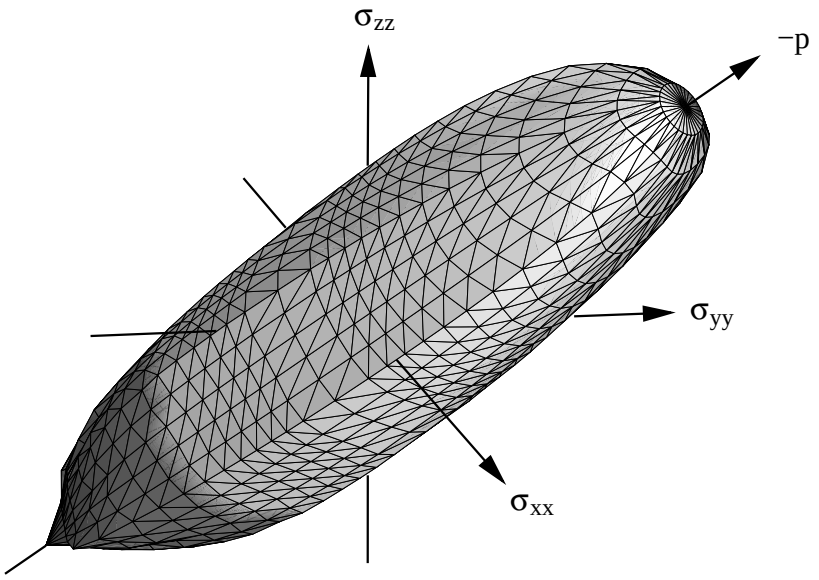

Figure 7.7: Yield surface of the Kelvin foam; $\rho^*/\rho_s = 0.05$.

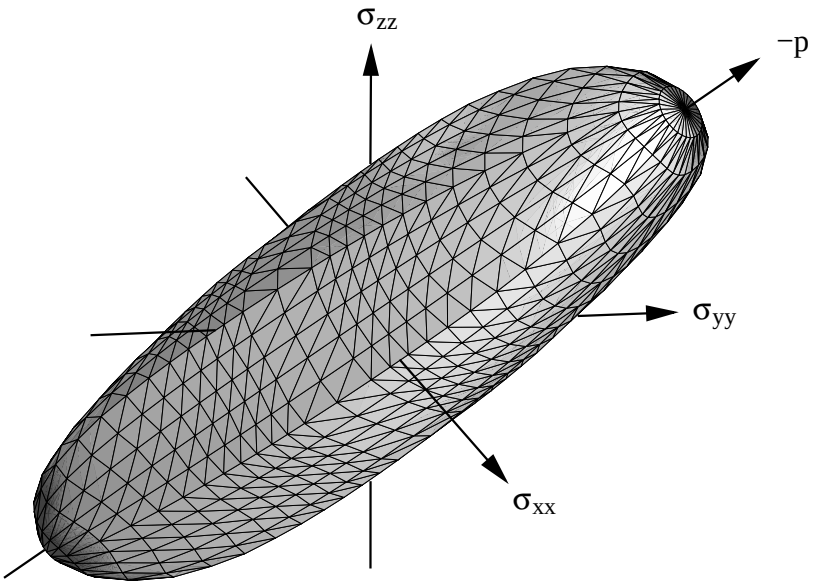

Figure 7.8: Yield surface of the Kelvin foam; $\rho^*/\rho_s = 0.1$.

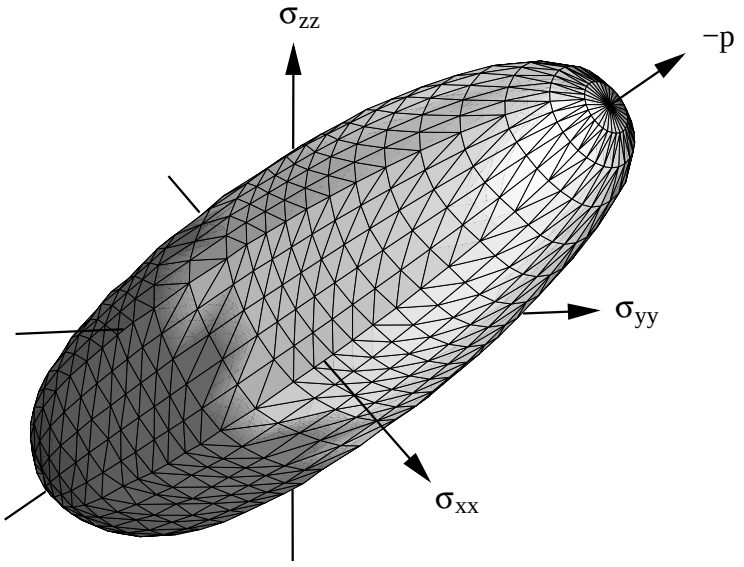

Figure 7.9: Yield surface of the Weaire-Phelan foam; $\rho^*/\rho_s = 0.05$.

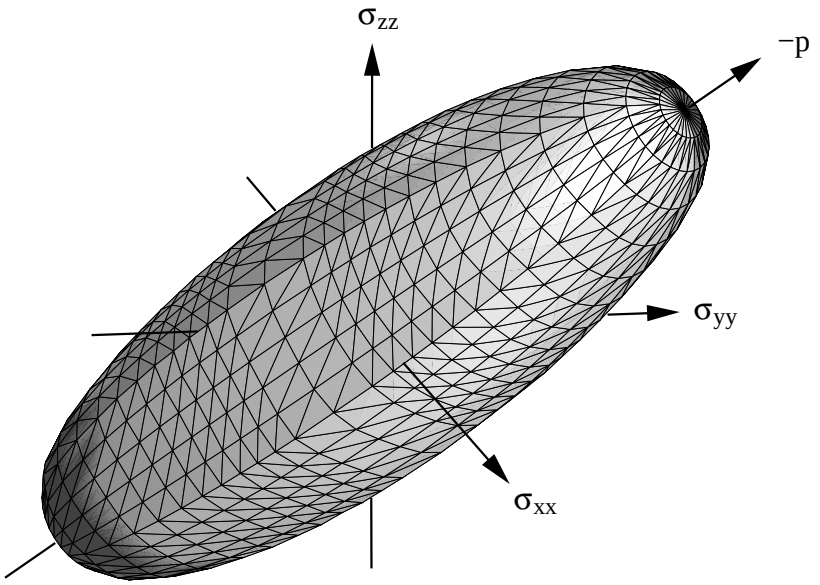

Figure 7.10: Yield surface of the Weaire-Phelan foam; $\rho^*/\rho_s = 0.1$.

At some points of the analyses ABAQUS issued *negative eigenvalue warnings*. These warnings indicate that a bifurcation load (buckling load) may have been exceeded, or that the load may have reached a local maximum.

For each loading path we determined the first increment with a negative eigenvalue warning[1]. If the load corresponding to the onset of macroscopic yielding as defined in Section 7.3.1 is greater than the load corresponding to the first negative eigenvalue warning we consider the result as open to doubt. In Figures 7.7 to 7.10 the respective vertices have been assigned a dark color.

Those vertices for which the first negative eigenvalue warning occurs before the onset of macroscopic yielding are found in a region around the axis corresponding to hydrostatic compression. In this region one of two things may have happened:

First, elasto-plastic buckling may have occurred before the equivalent plastic strain reached 0.2%. ABAQUS eigenvalue buckling prediction indicates that elastic buckling of the flat faces might have occurred. However one has to be cautious here because ABAQUS eigenvalue buckling prediction does not take into account elasto-plastic material behavior.

Second, the macroscopic limit load may have been reached before the equivalent plastic strain reached 0.2%. It turns out that the latter case only appears with the low relative density ($\rho^*/\rho_s = 0.05$) for loads that closely approach hydrostatic compression. In these cases we regard the macroscopic limit load as the load corresponding to the onset of macroscopic yielding.

The region containing vertices for which the first negative eigenvalue warning occurs before the onset of macroscopic yielding is larger for the foams of low relative density ($\rho^*/\rho_s = 0.05$). This is reasonable since thinner cell walls are more likely to buckle. Moreover, for both relative densities the region with potentially problematic results is larger for the Weaire-Phelan than for the Kelvin foam. The reason for this could be that the Weaire-Phelan foam has flat cell walls with a characteristic diameter that is approximately equal to the characteristic diameter of the non-flat cell walls, whereas the Kelvin foam has flat cell walls with a characteristic diameter that is clearly smaller than that of the non-flat cell walls. (See Figures 3.5, 3.15 and 3.16 on pages 23, 31 and 32.)

Figures 7.11 and 7.12 show cross-sections of the yield surfaces obtained by intersection of the respective surface with the "plane of zero mean stress" $\sigma_{xx}+\sigma_{yy}+\sigma_{zz} = 0$. This plane is the "equatorial plane" of the mesh shown in Figure 7.6(a). For comparison the figures also show a circle corresponding to the von Mises yield criterion.

In Figures 7.13 to 7.16 the vertices of the yield surfaces are projected to the von Mises equivalent stress versus mean stress plane. Vertices lying on the same meridian (see Figure 7.6(a)) are connected with a line. "Normal" vertices are marked

[1] In ABAQUS every increment can have several "attempts". Negative eigenvalue warnings issued for any but the last attempt are of course irrelevant and were ignored.

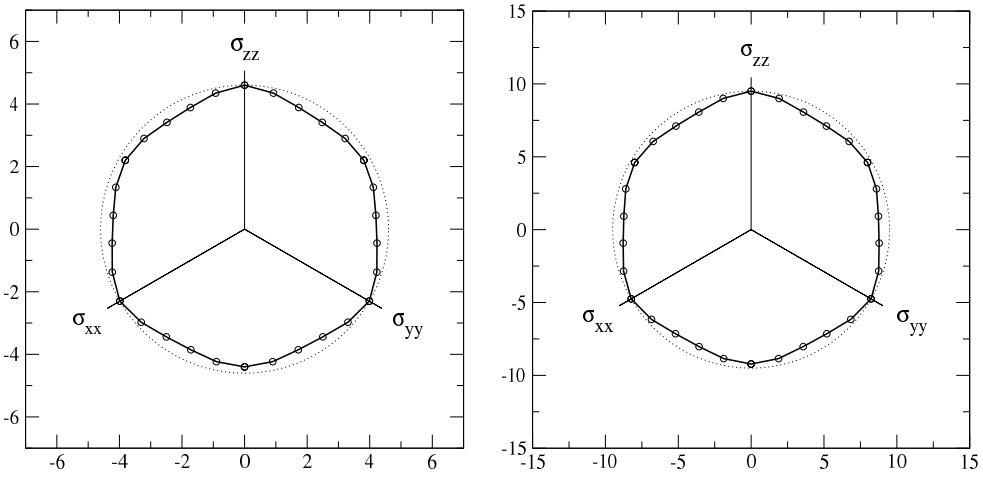

(a) $\rho^*/\rho_s = 0.05$ (b) $\rho^*/\rho_s = 0.1$

Figure 7.11: Cross-sections of the yield surfaces at the plane of zero mean stress; Kelvin foam; A circle corresponding to the von Mises yield criterion is shown for comparison.

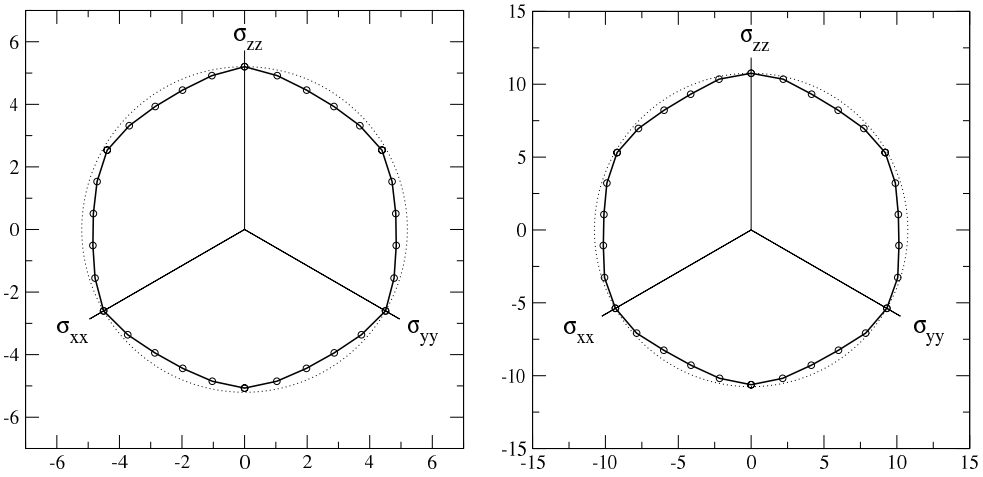

(a) $\rho^*/\rho_s = 0.05$ (b) $\rho^*/\rho_s = 0.1$

Figure 7.12: Cross-sections of the yield surfaces at the plane of zero mean stress; Weaire-Phelan foam; A circle corresponding to the von Mises yield criterion is shown for comparison.

with a circle and vertices where the first negative eigenvalue warning occurs before the onset of macroscopic yielding are marked with an "x".

The von Mises equivalent stress is given by:

$$\sigma_{\mathrm{VM}} = \sqrt{\frac{1}{2}\left[(\sigma_{xx}-\sigma_{yy})^2 + (\sigma_{yy}-\sigma_{zz})^2 + (\sigma_{zz}-\sigma_{xx})^2 + 6\left(\sigma_{xy}^2+\sigma_{yz}^2+\sigma_{zx}^2\right)\right]} \tag{7.17}$$

and, since we do not consider any shear stresses:

$$\sigma_{\mathrm{VM}} = \sqrt{\frac{1}{2}\left[(\sigma_{xx}-\sigma_{yy})^2 + (\sigma_{yy}-\sigma_{zz})^2 + (\sigma_{zz}-\sigma_{xx})^2\right]} \tag{7.18}$$

The mean stress is:

$$\sigma_{\mathrm{m}} = \frac{\sigma_{xx}+\sigma_{yy}+\sigma_{zz}}{3} \tag{7.19}$$

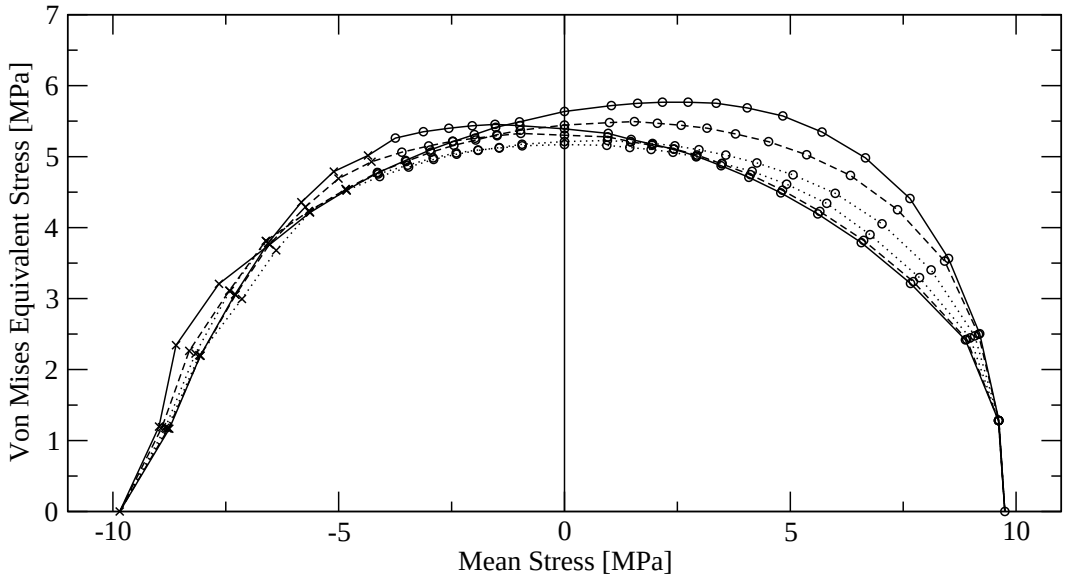

Figure 7.13: Yield surface projected to the von Mises equivalent stress versus mean stress plane; Kelvin foam; $\rho^*/\rho_s = 0.05$.

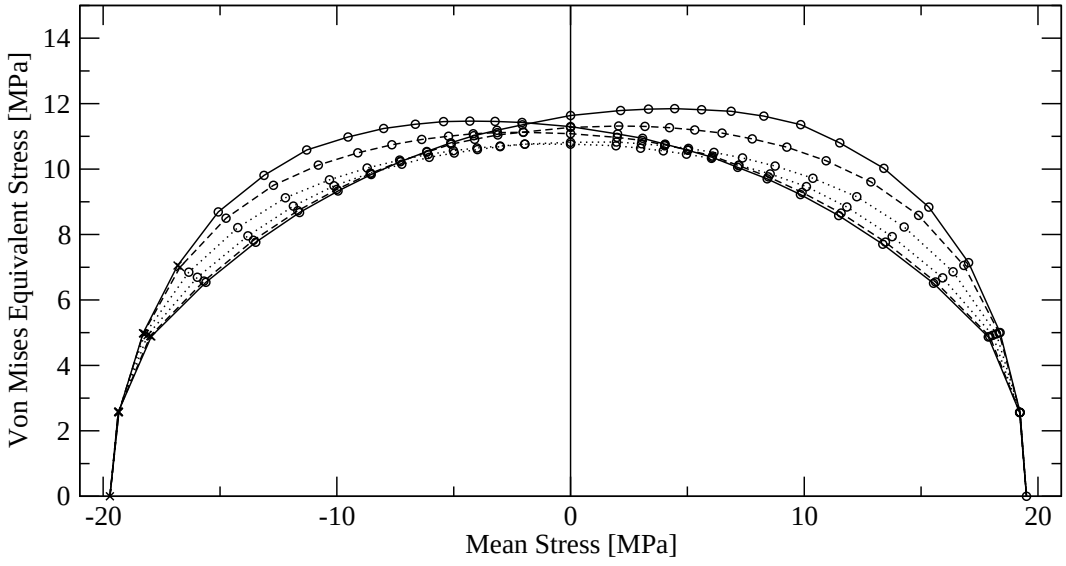

Figure 7.14: Yield surface projected to the von Mises equivalent stress versus mean stress plane; Kelvin foam; $\rho^*/\rho_s = 0.1$.

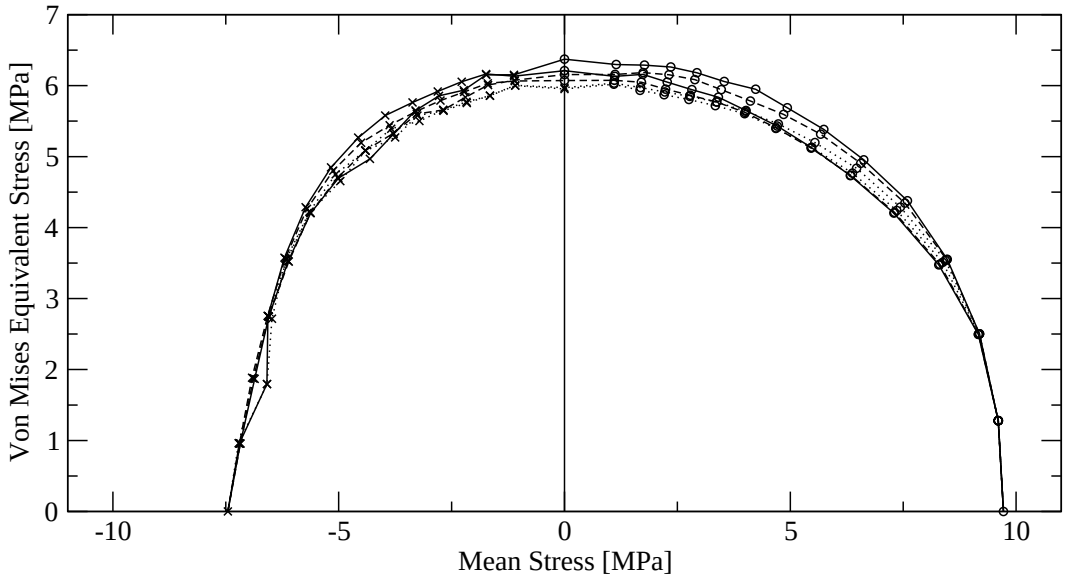

Figure 7.15: Yield surface projected to the von Mises equivalent stress versus mean stress plane; Weaire-Phelan foam; $\rho^*/\rho_s = 0.05$.

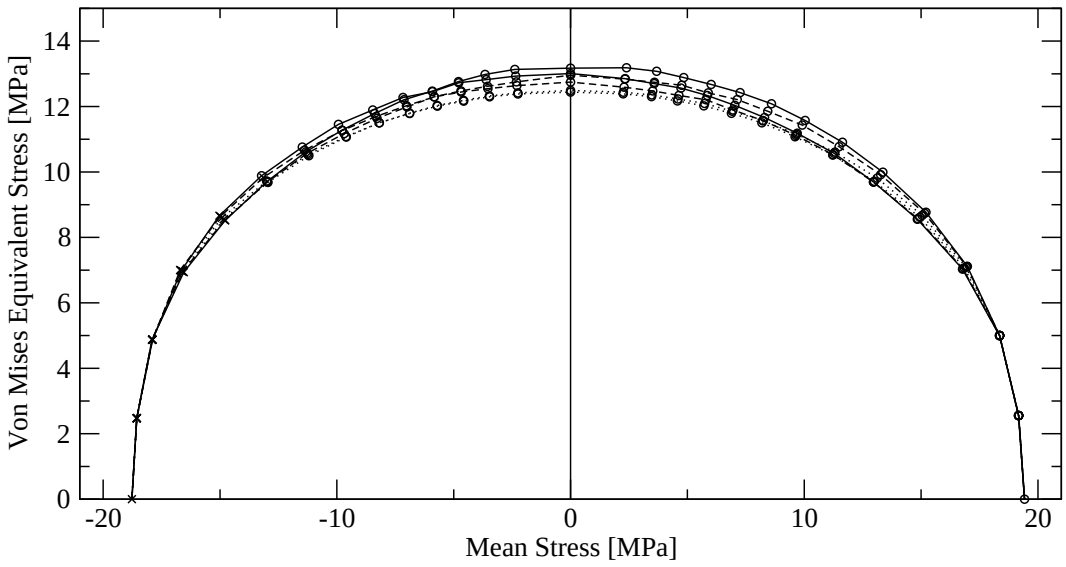

Figure 7.16: Yield surface projected to the von Mises equivalent stress versus mean stress plane; Weaire-Phelan foam; $\rho^*/\rho_s = 0.1$.

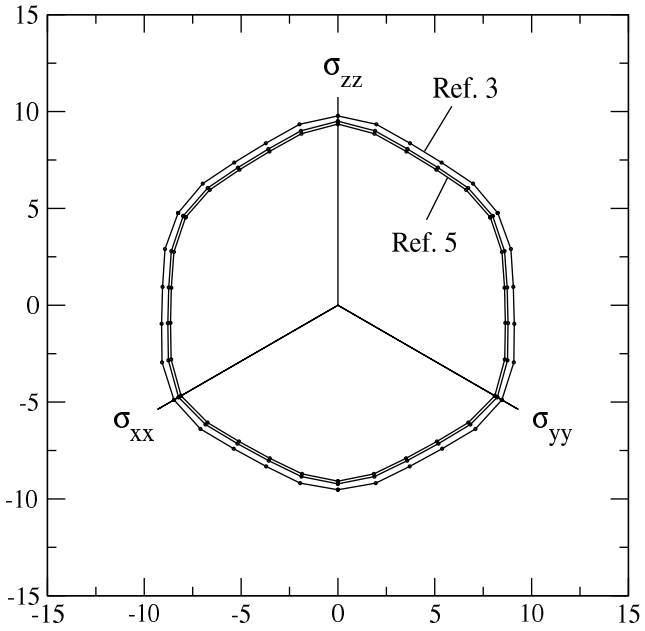

Figure 7.17: Convergence of the yield surface for mesh refinement 3, 4 and 5; Kelvin foam; $\rho^*/\rho_s = 0.1$; (Cross-section at the plane of zero mean stress).

7.3.3 Convergence for Different Mesh Refinements

The yield surfaces obtained by the non-linear method described above should not strongly depend on mesh refinement. (See explanations in Section 7.2). To verify this we performed the non-linear calculations for refinement 3, 4 and 5 of the Kelvin foam (see Figures 5.6 and 5.7 on pages 53 and 54). The results are shown in Figures 7.17 and 7.18 and show good convergence.

7.3.4 Comparison Kelvin - Weaire-Phelan

Figure 7.19 shows a comparison of the cross-sections of the yield surfaces of the Kelvin and Weaire-Phelan foams with both having a relative density of either 0.05 or 0.1. Moreover, the yield surfaces of the two foams can be compared using Figures 7.13 to 7.16.

Values for the critical von Mises stress are generally higher for the Weaire-Phelan foam. Moreover, the individual "meridians" in Figures 7.13 to 7.16 are less scattered for the Weaire-Phelan foam. Surprisingly, the critical mean stress in the case of hydrostatic tension is almost exactly the same for both foams.

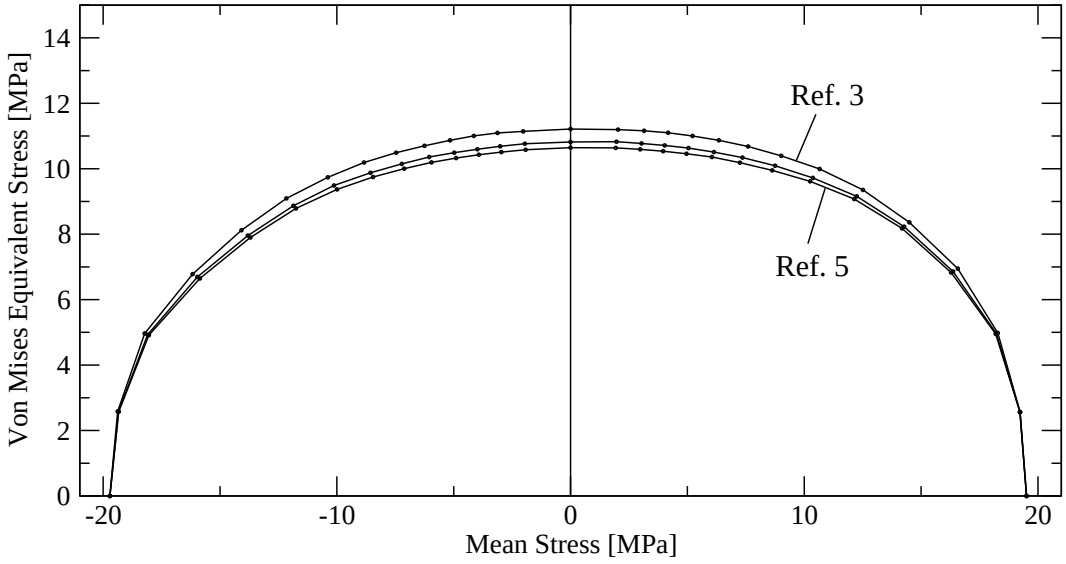

Figure 7.18: Convergence of the yield surface for mesh refinement 3, 4 and 5; Kelvin foam; $\rho^*/\rho_s = 0.1$; For clarity only one meridian per mesh refinement is shown.

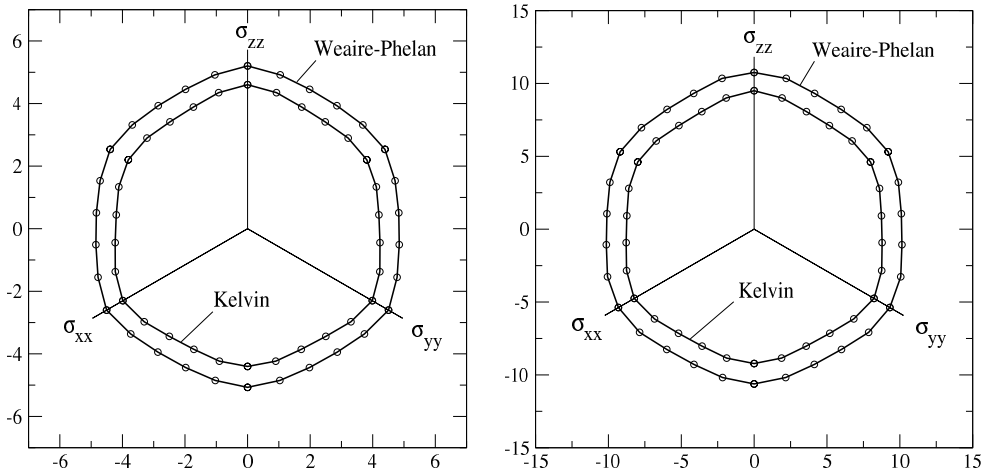

(a) $\rho^*/\rho_s = 0.05$ (b) $\rho^*/\rho_s = 0.1$

Figure 7.19: Cross-sections of the yield surfaces of the Kelvin and Weaire-Phelan foams for two different relative densities at the plane of zero mean stress.

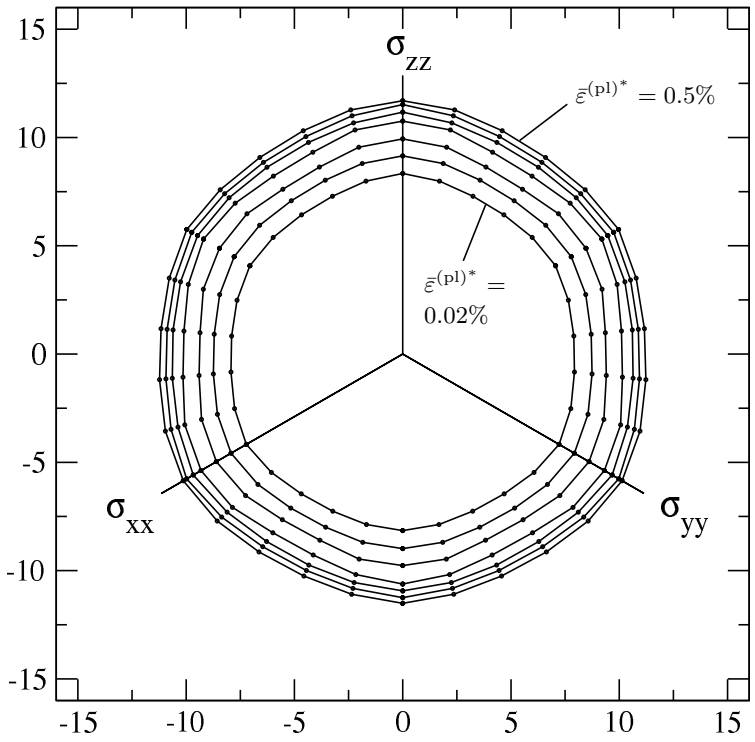

Figure 7.20: Cross-section of the yield surfaces obtained for different values of the critical equivalent plastic strain at the plane of zero mean stress; Weaire-Phelan foam; $\rho^*/\rho_s = 0.1$.

7.3.5 Influence of Chosen Critical Equivalent Plastic Strain

Looking at Figure 7.5 on page 91 we notice that the critical radius in stress space depends on the choice of the critical equivalent plastic strain. All figures above show results for $\bar{\varepsilon}^{(\mathrm{pl})^*} = 0.2\%$. In Figures 7.20 and 7.21 results for the critical equivalent plastic strain ranging from 0.02% to 0.5% are shown.

Obviously, the yield surface becomes smaller and smaller for decreasing values of the critical equivalent plastic strain. For $\bar{\varepsilon}^{(\mathrm{pl})^*} = 0.0\%$ the critical radius in stress space would be found where the first integration point fulfills the von Mises yield criterion. So the results would be the same as with the method described in Section 7.2. In Figure 7.5 (page 91) the first non-zero value of the equivalent plastic strain is found for the radius in stress space $\lambda \approx 8\,\mathrm{MPa}$. This is less then half of the value found for $\bar{\varepsilon}^{(\mathrm{pl})^*} = 0.2\%$!

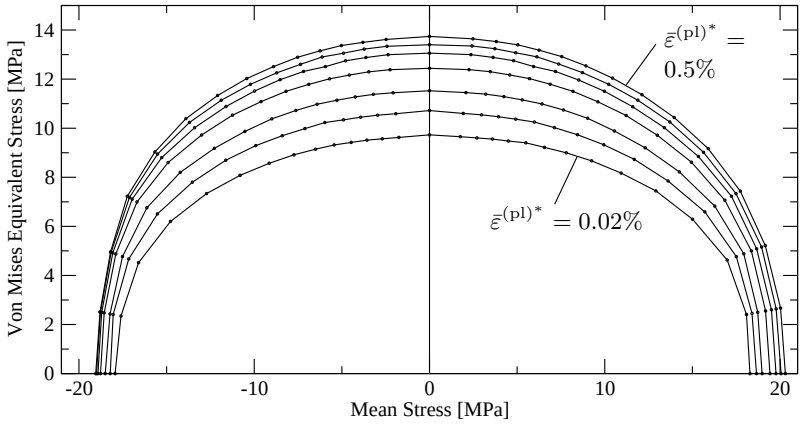

Figure 7.21: Projection of the yield surfaces obtained for different values of the critical equivalent plastic strain to the von Mises equivalent stress versus mean stress plane; Weaire-Phelan foam; $\rho^*/\rho_\mathrm{s} = 0.1$.

7.3.6 Using Plastic Dissipation for Evaluating Macroscopic Yield Surfaces

We have used a given value of the equivalent plastic strain (Equation (7.16)) for defining the onset of macroscopic yielding. As an alternative a critical value of the *plastic dissipation* could be used. This is quite straightforward because ABAQUS outputs the plastic dissipation by default. However, the choice of a realistic value for the critical plastic dissipation is not so apparent.

We simply took the value of the plastic dissipation the different foam structures had in the case of uniaxial tension at a plastic strain of $\varepsilon^{(\mathrm{pl})} = 0.2\%$ as this critical value.

The resulting yield surfaces differ surprisingly little from the results obtained using the equivalent plastic strain. Looking at the cross-section at the plane of zero mean stress the differences are hardly noticeable.

Figures 7.22 and 7.23 show a comparison in the von Mises equivalent stress versus mean stress plane. For clarity only one meridian is shown in each case. The maximum and minimum values of the mean stress are slightly lower using the plastic dissipation yield criterion.

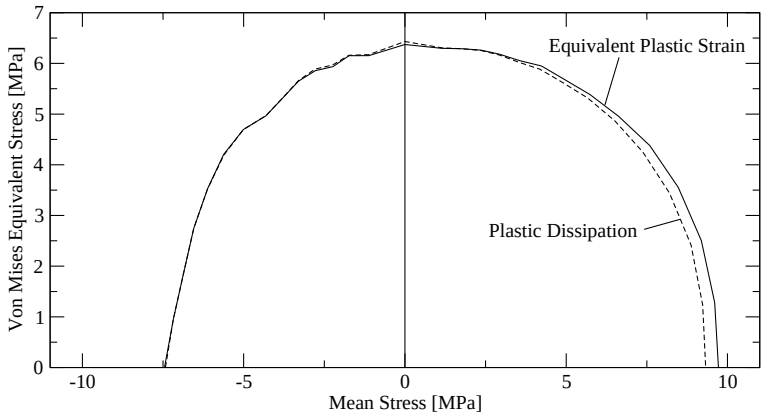

Figure 7.22: Comparison of the yield surfaces found using equivalent plastic strain and plastic dissipation energy; Weaire-Phelan foam; $\rho^*/\rho_s = 0.05$; For clarity only one meridian is shown in each case.

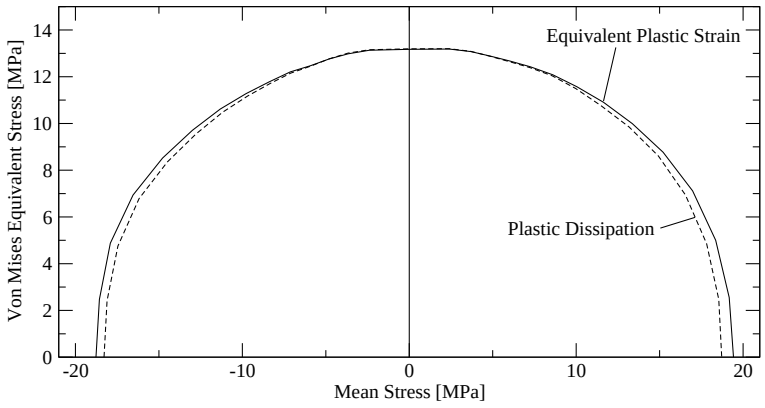

Figure 7.23: Comparison of the yield surfaces found using equivalent plastic strain and plastic dissipation energy; Weaire-Phelan foam; $\rho^*/\rho_s = 0.1$; For clarity only one meridian is shown in each case.

8 Conclusions and Outlook

We have discussed the physical laws, which govern liquid foam structures, and we used the program Surface Evolver for predicting two ideal, dry foam structures that obey these laws: the Kelvin and the Weaire-Phelan foam. Both structures were shown to have curved as well as flat faces. The occurrence of the flat faces is a direct result of the symmetries of these structures.

Even though the curvature of the curved faces is barely noticeable it was shown to influence the linear elastic behavior of both structures for relative densities below about 4%. It can hence be expected that the behavior of real metal foams is also strongly affected by the curvature of the faces.

Though the geometries of the Kelvin and Weaire-Phelan foams are obviously very different, the predicted Young's moduli and shear moduli differ only little from each other. Concerning orientation dependence of Young's modulus the Weaire-Phelan foam turned out to be virtually isotropic for relative densities above 4%. For the Kelvin foam on the other hand, the biggest value for Young's modulus differs from the smallest value by more than 14% for relative densities above 4%. For extremely low relative densities both foams behave quite anisotropically.

The prediction of the initial yield surface using linear Finite Element analysis turned out to be inapplicable. Using non-linear Finite Element analysis and an elasto-plastic bulk material law, yield surfaces for both foam structures could be predicted. However, these yield surfaces contain a region where elastic or elasto-plastic buckling of the flat faces occurs. To investigate the post-buckling behavior with ABAQUS imperfections would have to be included. However, these imperfections would be unphysical, as they would contradict the law of Laplace.

To solve the problem described above Surface Evolver could be used to predict a *random foam*. Such a random foam could be attained by using a Voronoi tessellation with randomly distributed sites, by using randomly distributed cell volumes or a combination of both strategies. All faces in such a foam would be surfaces of constant mean curvature and non-flat. So buckling would probably not occur in such a stochastic foam.

The linear elastic behavior of the two foam structures has been investigated for relative densities up to 25%. This was done because it required no additional effort. Of course using a structure corresponding to the dry foam limit for relative densities as high as 25% makes only limited sense from the physical point of view. In Section 4.3 we used Surface Evolver to predict a wet Weaire-Phelan foam structure. We believe that this is a very promising model for foams with a relative density higher than a few percent and, thus, a candidate model for future study.

Bibliography

The entries are arranged alphabetically by the author's last name.

Abaqus (2003). *ABAQUS Theory Manual*. Pawtucket: ABAQUS, Inc.

Ashby, M. F., Evans, A., Fleck, N. A., Gibson, L. J., Hutchinson, J. W., & Wadley, H. N. (2000). *Metal Foams - A Design Guide*. Butterworth-Heinemann.

Bathe, K.-J. (2002). *Finite-Elemente-Methoden* (Second ed.). Berlin: Springer.

Brakke, K. A. (1992). The Surface Evolver. *Experimental Mathematics*, *1*(2), 141–165.

Brakke, K. A. & Sullivan, J. M. (1997). Using symmetry features of the Surface Evolver to study foams. In *Visualization and Mathematics: Experiments, Simulations and Environments* (pp. 95–117). New York: Springer.

Daxner, T. (2003). *Multi-Scale Modelling and Simulation of Metallic Foams*. Fortschritt-Berichte VDI, Reihe 18. Düsseldorf: VDI Verlag.

Gibson, L. J. & Ashby, M. F. (1997). *Cellular Solids: Structure and Properties* (Second ed.). Cambridge University Press.

Grenestedt, J. L. (1998). Influence of wavy imperfections in cell walls on elastic stiffness of cellular solids. *Journal of the Mechanics and Physics of Solids*, *46*(1), 29–50.

Grenestedt, J. L. (1999). Effective elastic behavior of some models for perfect cellular solids. *International Journal of Solids and Structures*, *36*(10), 1471–1501.

Grenestedt, J. L. & Bassinet, F. (2000). Influence of cell wall thickness variations on elastic stiffness of closed-cell cellular solids. *International Journal of Mechanical Sciences*, *42*, 1327–1338.

Grenestedt, J. L. & Tanaka, K. (1999). Influence of cell shape variations on elastic stiffness of closed cell cellular solids. *Scripta Materialia*, *40*(1), 71–77.

Hales, T. C. (2001). The honeycomb conjecture. *Discrete and Computational Geometry*, *25*(1), 1–22.

Hosford, W. F. (1993). *The Mechanics of Crystals and Textured Polycrystals*. Oxford University Press.

Lord Kelvin (1887). On the division of space with minimum partitional area. *Phil. Mag.*, *24*(151), 503–514.

Kraynik, A. M., Reinelt, D. A., & van Swol, F. (2003). Structure of random monodisperse foam. *Physical Review E*, *67*(3), 31403–1–11.

Kusner, R. & Sullivan, J. M. (1996). Comparing the Weaire-Phelan equal-volume foam to Kelvin's foam. In D. Weaire (Ed.), *The Kelvin Problem* (pp. 71–80). KTK Scientific Publishers.

Matzke, E. B. (1946). The three-dimensional shape of bubbles in foam. *American Journal of Botany*, *33*(1), 58–80.

Nye, J. F. (1985). *Physical Properties of Crystals*. Oxford University Press.

Phelan, R., Weaire, D., & Brakke, K. A. (1995). Computation of equilibrium foam structures using the Surface Evolver. *Experimental Mathematics*, *4*(3), 181–192.

Plateau, J. (1873). *Statique Expérimentale et Théorique des Liquides soumis aux Seules Forces Moléculaires*. Paris: Gauthier-Villars.

Rammerstorfer, F. G. (2002). Skriptum zur FEUANIM-Vorlesung. Vienna University of Technology.

Rammerstorfer, F. G. & Böhm, H. J. (2004). Composites Engineering. Lecture Notes, Vienna University of Technology.

Roberts, A. P. & Garboczi, E. J. (2001). Elastic moduli of model random threedimensional closed-cell cellular solids. *Acta Materialia*, *49*(2), 189–197.

Smit, R. J. M., Brekelmans, W. A. M., & Meijer, H. E. H. (1998). Prediction of the mechanical behavior of nonlinear heterogeneous systems by multi-level finite element modeling. *Computer Methods in Applied Mechanics and Engineering*, *155*(1-2), 181–192.

Sullivan, J. M. (1999). The geometry of bubbles and foams. In J. F. Sadoc & N. Rivier (Eds.), *Foams and Emulsions*, volume 354 of *NATO ASI Series. Series E, Applied Sciences* (pp. 379–402). Kluwer Academic Publishers.

Weaire, D. (Ed.). (1996). *The Kelvin Problem: Foam Structures of Minimal Surface Area*. KTK Scientific Publishers.

Weaire, D. & Hutzler, S. (1999). *The Physics of Foams*. Oxford University Press.

Weaire, D. & Phelan, R. (1994). A counter-example to Kelvin's conjecture on minimal surfaces. *Philosophical Magazine Letters*, *69*(2), 107–110.